Biosphere Impacts of Ocean Hypoxia in a Warming Climate

Justin Leonard Penn

A dissertation
submitted in partial fulfillment of the
requirements for the degree of

Doctor of Philosophy

University of Washington

2020

Reading Committee:
Curtis Deutsch, Chair
Kyle Armour
Stephen Riser

Program Authorized to Offer Degree:
Oceanography

University of Washington

Abstract

Biosphere Impacts of Ocean Hypoxia in a Warming Climate

Justin Leonard Penn

Chair of the Supervisory Committee:
Professor Curtis Deutsch
Oceanography

Earth's climate and biology mediate the availability of dissolved oxygen (O_2) in seawater, a key environmental constraint on energy acquisition for diverse marine life. Energy available for organismal growth, activity, and maintenance becomes limited when the environmental O_2 supply falls short of the biological demand, a physiological condition termed 'hypoxia', which has far-reaching biogeochemical and ecological consequences beyond fitness detriments to individual species. For instance, in the ocean's small anoxic zones ($O_2 < \sim 5\ \mu M$), O_2 limitation of aerobic microbes selects for slower anaerobic metabolisms that convert nitrate (NO_3^-), a critical macronutrient, to biologically inert N_2 gas, thereby causing widespread nitrogen limitation of phytoplankton. Marine animals are more sensitive to low O_2 conditions than microbes and have no sustainable alternative metabolism to aerobic energy production. Even modest O_2 depletion can thus lead to their habitat restriction, both in the long-term by stable aerobic barriers, and dynamically from climate forcing. On geologic timescales, periods of extreme ocean warming and O_2 loss have been tied to episodes of global mass extinction. Currently, anthropogenic climate warming risks O_2 depletion of the modern ocean, threatening both global marine productivity and biodiversity. In this thesis, I aim to use mathematical models of physiology, ecology, biogeochemistry, and climate to explore the effects of hypoxia on marine ecosystems. In Chapters 2 and 3, I develop and analyze a microbial ecosystem model of the ocean's low O_2 zones, fit to geochemical data, to study how competitive dynamics between aerobic and anaerobic microbes regulate global nutrient loss. I find that species competition along minute O_2 gradients at the edges of anoxic zones modulates the long-term rate of ocean N removal, its sensitivity to climate forcing, and causes basin-wide fluctuations in N loss over time even in a stable environment. In Chapters 4 and 5, I focus on marine animal extinction risks from O_2 loss driven by warming by combining Earth System Model simulations of past and future climate change events with a model of species' ecophysiologial limits, calibrated by published laboratory measurements. Focusing on the Permian/Triassic marine mass extinction (~252 million years ago), in Chapter 4, I find that the predicted intensity and biogeographic signature of extinctions arising from ocean warming and O_2 loss explain reconstructions of this event from the marine fossil record. This work thus establishes a mechanistic link between global warming, hypoxia and extinction, with dire implications for future climate change. In Chapter 5, I project animal extinction risks from anthropogenic climate warming and O_2 loss under divergent future greenhouse gas emissions scenarios. If future emissions continue to accelerate, by the end of the century, extinctions driven by temperature-dependent hypoxia will surpass those from current anthropogenic threats, eventually risking a mass extinction comparable to the "Big Five" biotic crises in Earth's past. "Flattening the curve" of global greenhouse gas emissions would curtail these extinction risks, protecting the diversity of animal life in the oceans.

Table of Contents

Page

ACKNOWLEDGEMENTS

The work done for this dissertation would not have been possible if not for the community of people I've been lucky enough to share time with over the past 7 years. Firstly, I want to thank my advisor and dear friend Curtis Deutsch, whose thoughtfulness, patience, creativity, wisdom, and sense of humor have provided me with the richest graduate experience I could have hoped for. From my earliest days as an undergrad in office hours to our latest work on the Permian and beyond, Curtis always supported my explorations, while providing me with the right amount of guidance to see my ideas through to fruition. I look forward to our continued collaboration for years to come. This dissertation is also indebted to the rest of the Deutsch-Hughes family – Amy, Silas and Zia, who have over time become my own little home base in Seattle.

Truly this thesis would not have been possible without the computational assistance of the technical guru Hartmut Frenzel. I will dearly miss Oktoberfest, homemade Linzer torte, and chatting it up everyday about 'nada' in our offices in the Ocean Science Building. Próst my friend! I also am very grateful for the time I got to spend with my compadre, and fellow 'Sagan-head', Thomas Weber, who taught me many facets of ocean biogeochemical modeling, not to mention how to drive stick shift. How I miss our freewheeling brainstorms in those early days! Tom's research and three-dimensional biogeochemical modeling code laid the groundwork for much of my Chapters 2 and 3. I am also grateful to Cecilia Bitz for teaching me the fundamentals of climate modeling and for technical assistance with the Earth System Model simulations in Chapter 4.

I am thankful for having had excellent coauthors during my time in graduate school. A major thank you to Bonnie Chang for her work on the NH_4^+ measurements in Chapters 2 and 3, and to Jonathan Payne and Erik Sperling for their work on the fossil record analysis in Chapter 4.

The work done for Chapter 5 would not have been possible without the support of a graduate student fellowship from the Program on Climate Change at the University of Washington.

My time at the University of Washington wouldn't be so near to my heart if not for the amazing group of graduate students that keeps our community bustling even in the rainiest of winter months. I would certainly be remiss if not to call out two of my closest, and now lifelong, friends – Jake Steinberg and Angie Boysen. Jake and I were truly like brothers separated by the East and West coasts and with personalities that respectively encapsulated their distinct vibes, but which have slowly converged over time. From discussing the mysteries of Universe to the greatest 'TV show about nothing' and everything in between, our search for a good Seattle bagel will continue to the end of time, I'm sure. You'd be hard to find a kinder and more intelligent human than Angie. Angie taught me many things about the outdoors and how to live a full life balancing both work and fun. If given the opportunity to explore outer space, I'd want Angie to pilot the spaceship. There are too many stories to recount, too many adventures we've three had together. It already makes me sad to think of the band breaking up, but it will be all the more tasty when the reunion tour hits… I'd also like to give a special shout out graduate students Elizabeth Brasseale, Ethan Campbell, Megan Duffy, Erik Frederikson, Katherine Heal, Shirley Leung, Ashley Maloney, Brett Morris, Sara Ragen, Hally Stone, Earl Wilson, and certainly more.

This work also benefitted from the guidance, expertise, and scientific input of my advisory committee, Kyle Armour, Anitra Ingalls, and Steve Riser. A special thanks to Kyle for his encouragement and engaging discussions on climate and science in general, and his thoughtful input on Chapter 5, over drinks at the College Inn Pub and elsewhere.

I am indebted to the advice and thoughtfulness of my fellow Deutsch lab group members past and present who helped guide me along the way. Thank you to Keisuke Inomura for always making me laugh and teaching me about the inner workings of microbes. I will always fondly remember chatting about oxygen dynamics and grad student life with Andrew Margolskee, being bunkmates on the R/V Sikuliaq with Jacob Cram, adventures in species modeling and in Massachusetts with Evan Howard, snowboarding with Sarah Myhre, and mushroom hunting with Allison Smith. The Universe would not be as kind without all of you in it.

I am also grateful for my friend Clara Fuchsman whose intricate knowledge about the microbial N-cycle helped solidify my own understanding and whose kind encouragement always pushed me forward. During graduate school, I was lucky enough to embark upon a research cruise to the eastern tropical Pacific on the R/V Sikuliaq where I learned some of the basics of oceanographic data collection. Thank you to Gabrielle Rocap and Rick Keil for this opportunity and for mentoring me along the way. I also would love to give a special thanks to Al Devol, a legend of all things oceanographic; I will never skip the chance to soak up Al's knowledge on the cycling of the seventh element.

I'd additionally like to acknowledge Daniele Bianchi, for spirited discussions on low O_2 environments and the N-cycle, but most importantly, for mentoring me in the ways of the mushroom hunt. I will never forget the delicious spoils of our endless search: expansive bounties of Chanterelles, Boletes, Morels, and Lobsters cooked to Italian culinary perfection. May these fungi forever grow in the magical forests of the Pacific Northwest…

To my family – my grandparents Samuel and Gertrude Goetz, who opened the world to me through scholarly pursuits: I have been innumerably shaped by our travels retracing their paths through war-torn Europe. To my grandma Dorothy, my parents Steve and Genie, my sister Alexa, uncle Joe, my cousin Nathaniel, aunt Andrea, uncle Rick, and Dylan: You have all blessed me with a rich life full of love, kindness, and opportunity. Thank you to my parents in particular who have been fully supportive of me following my own weird dreams. I could not have been born to more loving parents. A special thanks to my sister Alexa, who keeps me young and from becoming too uptight, dude. To my friends and support net in Los Angeles, a crew to long to list, we've known each other for so long that often it feels like we are extensions of each other. And finally thank you to my biological grandmother, recently discovered through the secrets of DNA, the pre-eminent 'old Hollywood' gangster and burnt out rockstar, Judith Goldfadden.

My work is critically dependent on the support and love of my partner Yesenia Román López, a shining beacon of tropical light in a cloudy grey Seattle sky. I am everyday overjoyed and in disbelief that our souls found each other in this life on Earth across the vast possibilities of space and depths of time. Mi hogar es donde estás tú.

Ultimately, my path towards the scientific pursuit would not have started without the work and inspiration of the late planetary Scientist and great science communicator

Carl Sagan, whose musings on the cosmos inspired my own quest for understanding. He is often quoted saying, “We are like butterflies who flutter for a day and think it is forever.” This quote alone has often motivated me to finish Chapters 4 and 5.

And lest I not forget, this thesis was metabolically powered by the caloric supply of many a banh mi sandwiches assembled by the illustrious staff at the Saigon Deli on Brooklyn Ave. Oh how my mouth still waters at the thought of that crunchy baguette and deliciously seasoned tofu …

DEDICATION

To my ancestors who perished in the Holocaust.

To my grandparents, Drs. Samuel and Gertrude Goetz, who survived with their love for humanity intact, and taught me that the future of the world rests on the pursuit of truth with kindness.

Chapter 1

INTRODUCTION

Earth's climate and biology are closely tied to the availability of oxygen (O_2) in the ocean, a critical environmental constraint on aerobic metabolism, and thus fitness, for diverse marine life, from microbial cells to apex predators. In the surface ocean, O_2 produced by phytoplankton equilibrates with the atmosphere towards a saturation concentration that decreases with water temperature (*1–3*). At depth, temperature-dependent microbial respiration of sinking and dissolved organic matter depletes O_2 below saturated levels. The ultimate extent of this O_2 depletion is set by both the rate of organic matter supply from phytoplankton, and the timescale over which subsurface waters are ventilated by physical transport processes. The direct influence of these climatic and biological factors on the spatial distribution of O_2 can be observed in the general decline of O_2 from the poles to the tropics (*4*), where in the surface, warmer water lowers the gas solubility, and at depth, a weak ventilation of the tropical thermocline below high productivity leads to extensive biological utilization. The fingerprints of climate and biology are also apparent in the near-ubiquitous thermocline minimum in O_2, caused by the confluence of significant respiration and slow ventilation rates at those mid-water depths compared to shallower and deeper waters.

Climate warming is expected to exacerbate background O_2 depletion by further decreasing gas solubility, and increasing stratification, diminishing the physical supply of O_2 to marine life below the surface (*3*). Indeed, anthropogenic emissions of greenhouse gases have already caused detectable ocean warming and O_2 loss since the end of the pre-industrial era (ca. 1850 CE) (*5–8*), with trends projected to accelerate under continued rising emissions (*9–11*). If the environmental O_2 supply falls short of the organismal O_2 demand, this limits aerobic energy production, a condition termed 'hypoxia', which has widespread biogeochemical and ecological consequences beyond direct physiological impacts on individual organisms. The aim of this thesis is to develop and analyze mechanistic models of species physiology, ecology, biogeochemistry, and climate, calibrated by and validated against empirical data, to explore the impacts of hypoxia on the ocean's biogeochemical cycles and ecosystems.

For marine microbes, whose metabolic reactions drive the ocean's biogeochemical cycles, the physiological and geochemical impacts of hypoxia are most pronounced when O_2 is fully exhausted (*12–15*). Under these globally rare anoxic conditions ($O_2 < \sim 5$ μM; *16*), slow growing anaerobic species become competitive for key food substrates with aerobes (*17–19*). When anaerobes are dominant, they convert bioavailable forms of the critical macronutrient nitrogen (N) to biologically inert N_2 gas (*20*). Anaerobic N loss thereby depletes the global ocean's N inventory, and acts to limit phytoplankton growth across wide swaths of the low-latitude surface ocean (*21*, *22*). However, in global biogeochemical models of the ocean's O_2 and N cycles, the role of food web dynamics between competing aerobic and anaerobic microbial groups has remained largely unexplored.

In the first part of this dissertation, I developed and analyzed a three-dimensional microbial ecosystem model of the ocean's largest anoxic zone, and fit the model to geochemical field data, to test the role of O_2-dependent microbial community structure and competition in the long-term state (Chapter 2) and dynamics (Chapter 3) of marine N loss. I found that the coexistence of aerobic and anaerobic species at the edges of the anoxic zones slows the rate of global N removal, even while expanding anoxic zone size, and also increases the sensitivity of N removal to external forcing (Chapter 2). At the same time, the resulting microbial ecosystem interactions drive unforced, yet sustained fluctuations in the rates of N removal that persist at basin-scales (Chapter 3), consistent with evidence from nutrient measurements. Although these results are based on regional simulations of the eastern tropical North Pacific anoxic zone, I hypothesize these findings to be applicable to other anoxic environments, including in the permanent anoxic zones of the South Pacific and Arabian sea (*16*), in anoxic microenvironments, such as inside ocean eddys (*23*) and sinking organic particles (*24*), and even in seafloor sediment (*25*). This work also demonstrates the importance of, and lays the framework for, explicitly simulating subsurface microbial ecosystems in global biogeochemical models.

In contrast to extremely well-adapted marine microbes, the impacts of hypoxia on higher trophic levels begin at more modest, and geographically pervasive, O_2 depletions

(*26*). For diverse animal species, their critical oxygen thresholds (P_{crit}) – the ambient O_2 pressure at which the environmental supply equals the metabolic demand – span the full range of the ocean's aerobic conditions (*27–30*). Moreover, marine animals become increasingly sensitive to hypoxia as ambient temperature rises, owing to the fundamental temperature-dependence of metabolism (*27*, *28*, *31*). This temperature dependence acts as a double whammy on species' sensitivity to climate change; warming acts to reduce the environmental O_2 supply, while also increasing the biological demand. Indeed, warming on its own can induce hypoxia even without reductions in ambient O_2, if the metabolic demand is forced above the ambient O_2 supply.

The fitness detriments to marine animals from both long-term and transient hypoxia are increasingly being documented in the literature. For diverse marine species, long-term habitat range limits have been shown to coincide with O_2 levels matching the metabolic demand required for growth, reproduction and ecological activity, implying that hypoxia acts as a barrier to species range expansion (*27*, *28*). Under dynamically varying hydrographic conditions, local die-offs of benthic communities have coincided with the rapid development of intense low O_2 (*32*, *33*), while multi-decadal climate-forced fluctuations in thermocline O_2 are reflected in, and likely drivers of, shifts in fish species abundance (*34–37*). On geologic timescales, the fossil record is rich with examples of global anoxic events co-occurring with massive biodiversity declines (*38*). Perhaps the most well-established and dramatic example is the end-Permian mass extinction (c.a. 252 Ma), the largest in Earth history, during which over two-thirds of genera disappeared (*39*). Geochemical data indicates that global warming and O_2 loss were concurrent with the extinction, driven ultimately by volcanic greenhouse gas emissions (*40–45*). However, whether these environmental changes were the proximate cause of the extinction has not been established.

In chapter 4, I use the end-Permian marine mass extinction as a case study to test whether global warming and attendant O_2 loss could indeed have led to extinctions of diverse marine species, consistent with the fossil record. I simulated the global environmental changes of the Permian/Triassic climate transition using a fully coupled Earth System Model simulation, forced by rising greenhouse gas levels and guided by and validated against geochemical reconstructions of environmental conditions. To model changes in aerobic habitat leading to extinction, I utilized and expanded upon an ecophysiological model that accounts for diverse species' thermal and hypoxia limits, and is constrained by published laboratory measurements. I found that the combined physiological stresses of ocean warming and O_2 loss would have driven extinctions with a global magnitude and biogeographic pattern that can explain observations of these metrics from the marine fossil record. This work thus presents strong evidence for a direct link between climate warming, hypoxia, and extinction during the most extreme loss of biodiversity in Earth history. It also opens the door to understanding the role of climate change in other key events in the history of life, including during other extinction episodes and potentially during periods of biodiversity explosion.

The connection between global warming, ocean O_2 loss and mass extinction demonstrated in chapter 4 has important implications for future extinction risks arising from climate-forced O_2 depletion that is already occurring due to anthropogenic greenhouse gas emissions. In chapter 5, I turn my gaze to evaluating these extinction risks by pairing species ecophysiological limits with an ensemble of Earth System Model simulations that project future climate states under a range of greenhouse gas trajectories. I compare the magnitude of future extinction risks from warming to those caused by other anthropogenic factors, and also to other extinction events in Earth's past. I find that under a 'high emissions scenario', by the end of the century, accelerating extinction risks are expected to surpass all other anthropogenic threats in severity, eventually rivaling the intensity of past global extinction events. However, if dramatic action can be rapidly taken to "flatten the curve" of greenhouse gas emissions, extinctions would be reduced by over 70%. These results outline the range of future possibilities for life in the oceans, and in doing so demonstrate the direct connection between the collective behavior of humans and the habitability of the ocean. To quote the late Carl Sagan (*46*), "If we do not speak for Earth, who will?"

Chapter 2

Microbial functional diversity alters the structure and sensitivity of oxygen deficient zones

2.1 Abstract[1]

Oxygen deficient zones (ODZs) below the ocean surface regulate marine productivity by removing bioavailable nitrogen (N). A complex microbial community mediates N loss, but the interplay of its diverse metabolisms is poorly understood. We present an ecosystem model of the North Pacific ODZ that reproduces observed chemical distributions, yet predicts different ODZ structure, rates, and climatic sensitivity compared to traditional geochemical models. An emergent lower O_2 limit for nitrification lies below the upper O_2 threshold for denitrification, creating a zone of microbial coexistence that causes a larger ODZ, but slower total rates of N loss. The O_2-dependent competition for the intermediate nitrite produces gradients in its oxidation versus reduction, anammox versus heterotrophic denitrification, and the net ecological stoichiometry of N loss. The latter effect implies that an externally driven ODZ expansion should favor communities that more efficiently remove N, increasing the sensitivity of the N cycle to climate change.

---

[1] An edited version of this chapter was published as Penn J. L., Weber T., and Deutsch C., (2016), Microbial functional diversity alters the structure and sensitivity of oxygen deficient zones, *Geophysical Research Letters*, 43, 9773–9780, doi:10.1002/2016GL070438.

2.2 Introduction

The flux of organic matter sinking from the surface ocean can exceed the oxidative capacity of available dissolved O_2 in deeper water. Under the resulting O_2 deficient conditions, the most energetically favorable oxidant is nitrate (NO_3^-), an essential macronutrient for phytoplankton (*47*). The influence of N removal from the oxygen deficient zones (ODZs) is spread well beyond their small volumes (0.1% of the ocean) to encompass most of the low-latitude surface ocean, where biological productivity is N limited. Geochemical models of the N cycle, which convert NO_3^- directly to N_2 gas with a constant stoichiometry (*48*), predict that the rate of total N loss is controlled by the extent of the ODZs and the amount of organic matter they receive (*36*, *37*, *49*, *50*).

The loss of N results from a diverse microbial community exchanging multiple N-bearing substrates through interdependent metabolic pathways (*17*). The first step of heterotrophic denitrification yields NH_4^+ from organic matter and NO_2^- from the initial reduction of NO_3^-. These products can fuel autotrophic bacteria, including anaerobic ammonia oxidizers (anammox bacteria) (*51*) and two groups of aerobic nitrifiers (NH_4^+ and NO_2^- oxidizers). Anammox bacteria combine the metabolites to form N_2, while the nitrifiers reoxidize them to NO_3^-, diverting NO_2^- from further reduction by heterotrophs (*52*). Competition for the scarce intermediates can therefore either enhance or short-circuit the N loss process. The rates of these three metabolic pathways in the major ODZs are highly variable and unpredictable, and their relative importance to long-term N cycling remains controversial (*53–58*).

2.3 Methods

To investigate the effect of diverse metabolisms on the large-scale rates and stoichiometry of N loss we developed a microbial ecosystem model that simulates the biogeochemical cycles of N and O_2 (Figure 2.5A). Organic matter is formed by phytoplankton in the surface ocean and is remineralized by four microbial populations. Heterotrophic bacteria are facultative denitrifiers, switching from oxic respiration to a multistep denitrification (reduction of NO_3^- to NO_2^-, then to N_2) when O_2 falls below a critical threshold (O_2^{crit}) (*18*, *59*, *60*)]. The NH_4^+ released from organic N is used by three autotrophic species: anammox bacteria with a slow and O_2-inhibited growth rate (*61–64*) and aerobic NH_4^+ oxidizing archaea and NO_2^- oxidizing bacteria with nanomolar O_2 sensitivities (*62*, *65*, *66*).

Autotrophs assimilate NH_4^+ for cellular structure, while heterotrophs utilize dissolved organic nitrogen (DON), which is released by phytoplankton, sinking particles, and all populations upon mortality. Microbial parameters including growth and mortality rates, nutrient kinetics, and O_2 sensitivities were taken from appropriate laboratory measurements where available (Table 2.1).

Microbial biomass and chemical tracers were simulated in an ocean model covering the world's largest ODZ, in the eastern tropical North Pacific (ETNP) (*16*). We used an ocean general circulation model that is optimized to fit tracer observations (temperature, salinity, 14C, and CFCs), with a horizontal resolution of 2° latitude and longitude and 24 vertical levels (*67*, *68*). Tracer transport was computed using an annual-mean flow field within the ETNP domain, which extends from the equator to 35°N, the coast to 180°W, and the surface ocean to 2000m depth. Observed annual mean concentrations of O_2 and NO_3^- from the 2009 World Ocean Atlas (*69*) were transported into the domain at its open boundaries. This ensures that the fidelity of solutions reflects model skill for ODZ processes alone and prevents remote and unrelated errors from propagating into the region of interest.

To determine the sensitivity of model predictions to uncertainty in microbial traits, we conducted model simulations across a wide swath of parameter space. Microbial growth and mortality rates and nutrient half-saturations were varied by an order of magnitude, and the O_2 tolerances of heterotrophs and anammox bacteria were shifted from 1 to 10 and 15 μM, respectively (*13*, *18*, *59*, *60*, *62*, *64*, *70*). Each of the 89 resulting model solutions was vetted using field data from the ETNP, including climatological distributions of NO_3^- and O_2 and profile compilations of NH_4^+, NO_2^-, and excess N_2 gas (Figure 2.1). Parameter combinations that could not reproduce all tracer distributions simultaneously were not used for further analysis (Figure 2.6 and Table 2.1). A representative parameter set was chosen as our standard model case and integrated for 250 years to achieve a long-term steady state. A more detailed description of the methodology can be found in Section 2.7 Supplemental Methods.

2.4 Results

The model accurately reproduces observed patterns in metabolic rates and the distributions of chemical tracers (Figure 2.1). The predicted microbial community structure and associated metabolic rates vary between different habitats of the ODZ that are defined by distinct O_2 thresholds (Figures 2.1A and 2.1B). Heterotrophic respiration occurs aerobically in oxic water ($O_2 > O_2^{crit}$) (*13*, *59*). In these regions, aerobic-nitrifying populations are the dominant sink for NH_4^+ and NO_2^-. These obligate aerobes account for ~17% of O_2 consumption in oxic waters, but are the major consumers of O_2 in the ODZ. Indeed, they determine the lowest O_2 concentration attainable, which occurs when aerobic growth falls below mortality, halting the further consumption of O_2. This break-even O_2 concentration (O_2^*)(*71*). depends on the nitrifier's half-saturation constants, growth, and mortality rates and defines the core anoxic zone. For the ecosystem model parameters used here, O_2^* ranges from 0.14 to 1.5 nM, consistent with the lowest observed O_2 concentration in the ocean (*66*, *72*, *73*). In waters with $O_2 = O_2^*$, heterotrophs denitrify NO_3^- to N_2, and anammox bacteria act as the dominant sink for NH_4^+, declining into oxic water because of O_2 inhibition.

Between the two O_2 thresholds, O_2^{crit} and O_2^*, nitrifying and denitrifying populations coexist in a shell of suboxic water that surrounds the anoxic core of the ODZ. The simulated coexistence of these groups is consistent with simultaneous rate measurements (*58*, *65*, *70*, *74*, *75*), paired rate-gene data (*55*), and N isotopes (*76*, *77*). To achieve such coexistence in a steady state requires the O_2 threshold for denitrification (O_2^{crit}) to be above the minimum value required by nitrification (O_2^*). Because the value of O_2^* is constrained by observations to be in the nanomolar range, the overlap between aerobic and anaerobic habitat depends primarily on O_2^{crit}. The model's sensitivity to this uncertain threshold is examined below.

The microbial metabolic rates are also recorded in the observed distributions of key metabolites, providing strong constraints on time-mean community structure. Within the anoxic zone, the net reduction of NO_3^- to NO_2^- forestalls the downward increase in NO_3^-, shunting it into a subsurface maximum in NO_2^- (Figure 2.1C) (*54*, *60*, *73*). The further reduction of NO_2^- to N_2 by both heterotrophic and anammox bacteria yields an accumulation of excess N_2 (*78*) with no detectable NH_4^+ in anoxic water (*66*, *70*). In the oxic ocean, aerobic nitrification maintains both NH_4^+ and NO_2^- at low levels without production of N_2. Across a range of parameter sets (n= 43; see Table 2.1), the model simultaneously reproduces these chemical patterns, implying realistic balances among biological nutrient exchanges and physical fluxes. We use this group of model solutions to quantify the effect of both individual physiological traits and the entire microbial ecosystem on the large-scale cycling of O_2 and N.

Of all the microbial traits, the O_2 threshold of denitrification (O_2^{crit}) exerts the strongest influence on the size of the ODZ and its mean volumetric rate of N loss (Section 2.7 Supplemental Methods), two key features of ODZ biogeochemistry. As O_2^{crit} is increased from 1 to 10 μM, the volume of the ODZ defined by that threshold grows by nearly threefold (Figure 2.2A), in simulations as in climatological observations (*36*). In contrast, the mean rate of N loss declines by a fraction similar to the increase in ODZ size (Figure 2.2B). The net effect of this trade-off between volume and volumetric rate is that the ecosystem model maintains a constant total rate of N_2 production (Figure 2.2C) as well as of regional O_2 consumption (not shown), irrespective of the O_2 concentration at which denitrification begins. Although increases in O_2^{crit} reduce aerobic heterotrophic respiration, that change is compensated for by increases in O_2 consumption via NO_2^- oxidation coupled to heterotrophic NO_3^- reduction in the suboxic zone. These pathways have the same O_2 demand and net NO_3^- yield per unit DON remineralization (*17*). The O_2 threshold for denitrification therefore cannot be reliably inferred from distributions of O_2, NO_3^-, or N_2.

The insensitivity of integrated N loss to O_2^{crit} in the ecosystem model differs markedly from the predictions of traditional geochemical models, which do not explicitly represent microbial populations. Geochemical models assume no resource competition between nitrifying and denitrifying microbes and can be mimicked in the ecosystem model by excluding nitrifying populations from the ODZ (Figure 2.5B). Across the simulated range in O_2^{crit}, the ecosystem model produces an ODZ that is 25% to 100% larger than the geochemical approximation (Figure 2.2A) but with rates of N loss that are 14% to 66% slower on average (Figure 2.2B). These differences are independent of microbial growth and mortality rates and nutrient half-saturations (Figure 2.7). In contrast to the ecosystem model, regional N loss from the geochemical model increases with O_2^{crit}

because it causes the ODZ volume to rise without a concomitant reduction in volumetric N loss. As O_2^{crit} decreases, so does the overlap of aerobic and anaerobic habitat, causing the ecosystem and geochemical models to converge.

The ecosystem's dilution of N loss across a more expansive ODZ results from interactions between nitrifying and denitrifying bacteria. Nitrifiers are assumed to have a lower half-saturation constant for NO_2^- than the heterotrophic populations (Table 2.1), giving them a competitive advantage when O_2 is available. Indeed, this higher NO_2^- affinity is required in the model to reproduce the observed lack of NO_2^- in oxic water and its accumulation in anoxic waters (Figure 1). As a result of this advantage, nitrifying bacteria that thrive in the suboxic shell surrounding the core anoxic zone limit complete heterotrophic denitrification to N_2 by reoxidizing NO_2^- produced by the first step of denitrification (Figure 2.3A). The additional consumption of O_2 by nitrifiers leads to the simulated growth of the ODZ relative to the geochemical model, in which NO_2^- reoxidation is precluded. While concentrated at the boundaries of the anoxic zone, where O_2 falls below the detection limit of traditional methods, NO_2^- oxidation continues into the core (*58*), maintaining O_2 at levels below the detection limit of the most sensitive sensors (*56*, *66*). In the anoxic core, O_2 limitation of NO_2^- oxidation allows NO_2^- to accumulate, favoring complete heterotrophic denitrification to N_2.

The competitive advantage of NO_2^- oxidizers in the suboxic shell reduces the mean volumetric rate of N_2 production via its effect on the average stoichiometry of N loss (Figure 2.3B). By diverting NO_2^- from further reduction, nitrifying bacteria substantially lower the total amount of N_2 produced per mole of DON remineralized by heterotrophic denitrifiers (herein the N_2:DON ratio; mol N-N_2/mol N-DON), below the 7.5 assumed in traditional geochemical models (Figure 2.8). Depending on the value of O_2^{crit}, the mean N_2:DON ratio in the suboxic shell lies between 3.9 and 1.4. As O_2^{crit} is increased, this decreases the ODZ's average stoichiometry of N loss by expanding the niche of NO_2^- oxidizers. The O_2^{crit} threshold defines the volume of the suboxic shell, where NO_2^- oxidizers are dominant, but not the anoxic core, where NO_2^- uptake is controlled by denitrification. Increases in O_2^{crit} thus raise the ratio of suboxic to anoxic water, which shifts the stoichiometry of N loss toward the low values found in the suboxic shell, causing the slower mean volumetric rate of N loss (Figure 2.2B). In the geochemical model, volumetric N loss is maintained even as O_2^{crit} is increased, because it lacks a suboxic zone in which NO_2^- oxidation outcompetes heterotrophic denitrification.

Associated with these stoichiometric gradients are large variations in the fraction of N loss contributed by autotrophic anammox bacteria versus the heterotrophs, denoted $f$amx (Figure 2.3C). The attribution of N_2 production to these different populations from direct rate measurements in the field has proven controversial due to substantial variability with unknown cause (*53*, *54*, *56*, *57*, *65*). The microbial ecosystem produces spatial variations in $f$amx as a natural consequence of resource competition in the suboxic zone. In contrast to heterotrophs, the uptake of NO_2^- by nitrifiers has little effect on anammox bacteria because they are NH_4^+ limited (*17*, *51*). The fractional contribution of anammox to N_2 production is therefore greatest in the suboxic shell, and declines into the anoxic core of the ODZ, where reoxidation is slowed by scarce O_2. Integrated across the ODZ, anammox contributes to between 31% and 49% of N loss (i.e., $f$amx = 0.31–0.49; see section 2.7 supplemental methods and Figure 2.9).

The stoichiometry of steady state anaerobic reactions is thought to imply a mean $f$amx of 0.28 (*79*), but cannot explain the large observed deviations from this value. Previous studies assume that all NO_2^- produced by denitrification is reduced to N_2 (*70*). When accounting for the fraction of NO_2^- that is oxidized or accumulates in the water column, simulated spatial variabilities of both $f$amx and N_2:DON can be predicted exactly (Figure 2.3D). The niche partitioning of aerobic and anaerobic metabolisms along gradients in O_2 can thus reconcile variations in $f$amx and simple mass balance predictions, without the need for non-Redfieldian organic matter cycling (*70*) or supplementary sources of NH_4^+ (*80*, *81*).

2.5 Implications for Climate Warming

The gradient of N loss stoichiometry associated with the mean microbial habitat pattern implies a greater sensitivity of the N cycle to climate than previously recognized (Figure 2.4). The volume of low O_2 water undergoing N loss is itself quite sensitive to climate-driven changes in tropical O_2 (*36*), but changes in N loss also depend on the ratio of total N_2 production per unit of organic N remineralization via denitrification, which have not been previously considered. Because N_2:DON ratios increase systematically from the suboxic shell to the anoxic core (Figure 2.3B), any increase in the ratio of anoxic to suboxic water volume should also accelerate N loss and shift the balance of metabolisms in favor of heterotrophic denitrification over anammox.

To demonstrate this stoichiometric effect, we simulated the influence of a large-scale O_2 depletion on the contemporary volumes of anoxic and suboxic waters in the Pacific Ocean, by applying a uniform anomaly to the current climatological O_2 distribution. These idealized O_2 depletion experiments approximate the response of the ODZ's volume to historical climate variations in more realistic models (*36*). As O_2 is depleted on the regional scale, the volume of anoxic and suboxic waters both rise, as expected (Figure 2.4). However, the anoxic water expands proportionally faster, increasing the ratio of the anoxic core volume relative to that of the suboxic shell. Although observational uncertainties in current climatological volumes are considerable, an increase in the core to shell volume ratio is robust to these uncertainties (Figure 2.10) because it arises from simple geometry; a bounded volume grows proportionally faster than its surrounding surface.

To estimate the consequence of these volume changes for total N loss rates, we applied the model-predicted gradients in ecosystem stoichiometry throughout the Pacific ODZ. By altering mean N loss stoichiometry, shifts in the relative volumes of these distinct microbial habitat zones further increase N loss by an amount comparable to the ODZ volume expansion itself (Figure 2.4), thus doubling the impact of O_2 depletion in the metabolically diverse ocean compared to one with fixed N-cycle stoichiometry. A full accounting of the long-term effect of ocean deoxygenation and climate warming on N loss must take into account interactions between ocean circulation, N loss, and biological export, which our calculations have held constant. However, these idealized calculations illustrate a novel and important role for changing ecological stoichiometry due to shifts in the microbial community across the ODZ as the ocean loses O_2. Accurately predicting the response of N loss to climate change will therefore require ocean models to account for feedback between these microbial ecosystem dynamics and the biogeochemical cycles.

2.6 Acknowledgments

We thank Bonnie Chang for the NH_4^+ data, Tim DeVries for the ocean circulation model, Clara Fuchsman for the NO_2^- oxidation and STOX O_2 data, and Alyson Santoro for valuable feedback. This work was supported by a grant from the Gordon and Betty Moore Foundation (GBMF #3775).

2.7 Supplemental Methods

This section describes the model's construction, mass-balance calculations, and ocean data constraints. Text sections 2.7.1 and 2.7.2 explain the two major model components: the microbial ecosystem and the mass balance of the chemical cycles of N and O_2. In text section 2.7.3, we develop an ecosystem model that approximates traditional geochemical models. In text section 2.7.4, we diagnose the pathways of N loss and its stoichiometry from the ecosystem model simulations. Lastly, in text sections 2.7.5 and 2.7.6 we describe the model sensitivity tests, and the cost function and ocean data used to construct the ensemble of realistic model solutions.

2.7.1 Microbial Ecosystem Model

The biogeochemical cycles of N and O_2 are driven by biological rates derived from a microbial ecosystem model with four bacterial populations (B_X, in units of μM N; X abbreviates the population name) (Figure 2.5A). In each model grid box, the biomass of bacteria is governed by a set of ordinary differential equations in which time-rates of change are equal to the difference between growth, mortality, and ocean transport. The physiological traits governing growth and mortality are represented through a set of population-specific kinetic parameters, including the mortality rate (ϕ) and the maximum intrinsic growth rate (μ_{xy}, where Y is an index of growth substrate, if there is more than one), which can be reduced by resource limitation factors (γ^C_B) and a set of functions (*f*) that represent additional environmental influences. The resulting set of equations is:

$$\frac{dB_H}{dt} = \mathbf{A_I} B_H + f_H^{O2} \mu_{H1} \min(\gamma_H^{O2}, \gamma_H^{DON}) B_H + (1 - f_H^{O2})(\mu_{H2} \min(\gamma_H^{NO3}, \gamma_H^{DON}) + \mu_{H3} \min(\gamma_H^{NO2}, \gamma_H^{DON})) B_H - \phi_H B_H$$

Equation 2.1

$$\frac{dB_{AX}}{dt} = \mathbf{A_I}B_{AX} + f^{O2}_{AX}\mu_{AX}\min(\gamma^{NH4}_{AX},\gamma^{NO2}_{AX})B_{AX} - \phi_{AX}B_{AX}$$ Equation 2.2

$$\frac{dB_{AO}}{dt} = \mathbf{A_I}B_{AO} + \mu_{AO}\min(\gamma^{NH4}_{AO},\gamma^{O2}_{AO})B_{AO} - \phi_{AO}B_{AO}$$ Equation 2.3

$$\frac{dB_{NOB}}{dt} = \mathbf{A_I}B_{NOB} + \mu_{NOB}\min(\gamma^{NO2}_{NOB},\gamma^{O2}_{NOB})B_{NOB} - \phi_{NOB}B_{NOB}$$ Equation 2.4

Here, B_H is heterotrophic bacteria, B_{AX} is anammox bacteria, B_{AO} is ammonia oxidizing archaea, and B_{NOB} is nitrite oxidizing bacteria. $\mathbf{A_I}$ is a matrix that represents water transport between grid cells internal to the model domain. The parameters of the ecosystem model are discussed below and their numeric values are provided in Table 2.1.

The model's formulations of microbial physiology are similar to those used in wastewater treatment studies (*82*). The positive terms on the right-hand side of equations 2.1-2.4 represent bacterial growth, as a function of ambient chemical concentrations (C_X, in μM; X is the type of chemical). Resource constraints reduce the growth rate below its maximum value by a Michaelis-Menten limitation factor ($\gamma^C{}_B$):

$$\gamma^C_B = \frac{C_X}{C_X + K^C_B}$$ Equation 2.5

where $K_B{}^C$ is the half-saturation parameter of bacteria B_X on chemical C_X. Growth is limited only by the substrate with the lowest limitation factor (Liebig's Law of the Minimum).

In equation 2.1, the first three terms represent the growth of facultatively denitrifying heterotrophic bacteria on dissolved organic N (DON) through three oxidative pathways: O_2, NO_3^-, and NO_2^- reduction. Heterotrophic growth rates are proportional to the energetic yield of the operative metabolic pathway. The fraction of heterotrophic growth that respires O_2 versus NO_3^- or NO_2^- ($f_{O2}{}^H$) is influenced by the availability of O_2 in the environment (*18*, *59*, *60*). We model this using a rapid transition function:

$$f_H^{O2} = .5(1 - \tanh(O_2^{crit} - C_{O2})) \qquad \text{Equation 2.6}$$

where the parameter O_2^{crit} is the concentration of O_2 (C_{O2}) at which 50% of heterotrophic growth is partitioned to anaerobic metabolism.

In equation 2.2, the growth of anammox bacteria is through the anaerobic oxidation of NH_4^+ with NO_2^-, and is slowed by the presence of O_2 in the seawater (*61*, *62*, *64*), modeled according to the inhibition function:

$$f_{AX}^{O2} = \frac{K_{AX}^{inh}}{K_{AX}^{inh} + C_{O2}} \qquad \text{Equation 2.7}$$

where the parameter K_{AX}^{inh} determines the O_2 concentration (C_{O2}) at which anammox growth is 50% of its maximum, independent of substrate limitation. Growth through aerobic ammonia and nitrite oxidation are represented by the growth terms of equations 2.3 and 2.4, respectively. The subtractive terms of equations 2.1-2.4 represent bacterial mortality, which scales linearly with biomass, at a rate ϕ_B.

2.7.2 Chemical Cycles

The model's biogeochemical cycles of N and O_2 consist of the physical transport for each chemical tracer as well as biological sources and sinks, which are derived from the growth and mortality of the bacterial populations. The conservation equations that govern the pools of chemical tracers are:

$$\frac{dC_{NH4}}{dt} = \mathbf{A_I} C_{NH4} + \mathbf{A_E} C_{NH4}^E + J_{NH4}^{\Sigma H} - J_{NH4}^{AO} - J_{NH4}^{AX} - J_{NH4}^{NOB} - k^{phy} C_{NH4} \qquad \text{Equation 2.8}$$

$$\frac{dC_{NO2}}{dt} = \mathbf{A_I} C_{NO2} + \mathbf{A_E} C_{NO2}^E + J_{NO2}^{AO} + J_{NO2}^{H2} - J_{NO2}^{H3} - J_{NO2}^{AX} - J_{NO2}^{NOB} - k^{phy} C_{NO2} \qquad \text{Equation 2.9}$$

$$\frac{dC_{NO3}}{dt} = \mathbf{A_I} C_{NO3} + \mathbf{A_E} C_{NO3}^E + J_{NO3}^{NOB} + J_{NO3}^{AX} - J_{NO3}^{H2} - \mu^{phy} \gamma_{phy}^{NO3} \qquad \text{Equation 2.10}$$

$$\frac{dC_{DON}}{dt} = \mathbf{A_I}C_{DON} + \mathbf{A_E}C_{DON}^{E} + \sigma J^{phy} + J^{rem} + J_{DON}^{mort} - J_{DON}^{\Sigma H} \qquad \text{Equation 2.11}$$

$$\frac{dC_{N2xs}}{dt} = \mathbf{A_I}C_{N2xs} + J_{N2xs}^{H3} + J_{N2xs}^{AX} - \frac{K_W}{\Delta z_0}C_{N2xs} \qquad \text{Equation 2.12}$$

$$\frac{dC_{O2}}{dt} = \mathbf{A_I}C_{O2} + \mathbf{A_E}C_{O2}^{E} + r_{O2}J^{phy} - J_{O2}^{H1} - J_{O2}^{AO} - J_{O2}^{NOB} - K_{O2}(C_{O2} - O_2^{obs}) \qquad \text{Equation 2.13}$$

where C_{NH4} is ammonium (NH_4^+), C_{NO2} is nitrite (NO_2^-), C_{NO3} is nitrate (NO_3^-), C_{DON} is dissolved organic N (DON), C_{N2xs} is excess nitrogen gas (N_{2xs}) that is produced biologically within the ocean, and C_{O2} is dissolved oxygen gas (O_2). Units of N-bearing compounds are μM N. O_2 is in μM O_2. $\mathbf{A_E}$ is a matrix that represents transport into the model domain from exterior grid cells. The supercript E above tracer concentrations denotes the tracer boundary condition. See below for the definitions of parameters and biological sources and sinks (J). The numerical values of parameters are given in Table 2.1.

2.7.3 Primary Production.

Nutrients (NH_4^+, NO_2^-, and NO_3^-) are assimilated into organic matter by photosynthesis within the upper 75 m. Phytoplankton populations are not explicitly represented, but instead their uptake of surface nutrients is parameterized by:

$$J^{phy} = k^{phy}C_{NH4} + k^{phy}C_{NO2} + \mu^{phy}\gamma_{phy}^{NO3} \qquad \text{Equation 2.14}$$

where k^{phy} is the uptake rate of NH_4^+ and NO_2^- by phytoplankton (y^{-1}), μ^{phy} is the uptake rate of NO_3^- by phytoplankton (N y^{-1}), and γ^{NO3}_{phy} describes its limitation factor (equation 2.5). A fraction (σ) of assimilated N is converted directly to DON and transported by ocean circulation. The remainder is exported to depth in particles that are hydrolyzed to DON according to an empirical power law between the particle flux and depth (J^{rem}) with exponent b (*83*).

2.7.4 Remineralization.

The remineralization or respiration rate (in µM y^{-1}) of a chemical tracer is linked to the bacterial growth terms through the stoichiometry of their metabolic reactions. The term $J_{NH4}^{\Sigma H}$ (equation 2.8) is the sum of heterotrophic remineralization processes (H growth reactions 1-3) that produce NH_4^+ from DON ($J_{DON}^{\Sigma H}$; eq. 2.11). NH_4^+ can either be oxidized anaerobically to N_{2xs} through the anammox reaction (J_{NH4}^{AX}) or aerobically (J_{NH4}^{AO}) to NO_2^- (J_{NO2}^{AO}; in equation 2.9) during the first step of nitrification. NO_2^- is also produced by the first step of heterotrophic denitrification (J_{NO2}^{H}), termed dissimilatory NO_3^- reduction (J_{NO3}^{H2}; in equation 2.10). The consumption of NO_2^- occurs through three processes: oxidation during the second step of nitrification (J_{NO2}^{NOB}), reduction during the second step of heterotrophic denitrification (J_{NO2}^{H3}), and during the anammox reaction (J_{NO2}^{AX}). NO_2^- oxidation yields the major nutrient NO_3^- (J_{NO3}^{NOB}; equation 2.10), and completes the remineralization process, while heterotrophic denitrification reduces NO_2^- to the biologically unavailable form, N_{2xs} (J_{N2xs}^{H3}; in equation 2.12). N_{2xs} produced by the anammox reaction (J_{N2xs}^{AX}) derives from both NO_2^- and NH_4^+, while a small fraction of the NO_2^- consumed by anammox is oxidized to NO_3^- (J_{NO3}^{AX}) (*63*). N_{2xs} is subject to loss from gas exchange, with a surface flux equal to the excess N_2 times a piston velocity K_W. The rate of concentration change is the surface flux divided by the depth of the model's surface layer (Δz_o).

2.7.5 Stoichiometry.

The metabolic reaction stoichiometries are derived using the redox half-reaction method, which tracks the amounts of substrate used, metabolic products formed, and biomass synthesized during bacterial growth, ensuring a strict conservation of mass (*84*). The growth reaction of anammox is unique in that these bacteria are thought to use distinct e^- donors for carbon fixation and energy production, and because NO_2^- is used both as an oxidant and reductant (*63*). The stoichiometry of the cell synthesis reaction is fixed among the bacteria, and assumes constant elemental ratios in organic matter (*85*). Heterotrophic DON breakdown occurs through the reverse of cell synthesis.

2.7.6 Bacterial N Assimilation.

NH_4^+ requires the least amount of energy for use as a nutrient in biomass synthesis, making it preferred for bacterial growth (*84*). Autotrophs assimilate NH_4^+ directly from seawater. Heterotrophs can acquire N either through from NH_4^+ available in the environment, or their own breakdown of DON. In a balanced growth situation, the C:N ratio of the bacterial biomass relative to their organic matter substrate determines whether excess NH_4^+ is required from seawater to achieve mass balance (*86*). Since the C:N ratio of organic matter within the ETNP (6.8) (*70*) is statistically indistinguishable from that found in marine bacteria (6.8±1.2) (*87*), this implies that the N quota for heterotrophs can be satisfied by the uptake of DON alone. We therefore assume that heterotrophs acquire N for biomass from DON, without uptake of NH_4^+. The terms for DON and NH_4^+ uptake ($J_{DON}^{\Sigma H}$, J_{NH4}^{AO}, J_{NH4}^{AX}, J_{NH4}^{NOB}) also account for N assimilation into biomass. Bacterial mortality directs N from biomass to DON (J_{DON}^{mort}; equation 2.11).

2.7.7 O_2 cycle.

O_2 is produced in photic zone in the molar ratio r_{O2} during the assimilation of total N by photosynthesis (J^{phy}; eq. 2.13), and is consumed throughout the water-column by both aerobic organic matter remineralization (J_{O2}^{H1}) and the two stages of nitrification (J_{O2}^{AO} and J_{O2}^{NOB}). To ensure a realistic O_2 supply to the subsurface ODZ, the air-sea gas exchange of O_2 is modeled by restoring predicted values to observed concentrations (O_2^{obs}) in the top model layer at the rate K_{O2}.

2.7.8. Geochemical Model

We modified the ecosystem model to mimic traditional geochemical models of the N and O_2 cycles (Figure 2.5B) (*48*) and enable a direct comparison of their time-mean characteristics. Three assumptions distinguish the geochemical model: 1) the intermediates NH_4^+ and NO_2^- are implicitly treated, 2) autotrophic reactions are instantaneous, and 3) aerobic and anaerobic processes occur in isolation.

The model contains only a single heterotrophic bacteria population (B_H; in μM N). The same parametrizations of growth and decay from the ecosystem model apply to this heterotrophic population, whose time-rate of change is described by the following equation:

$$\frac{dB_H}{dt} = \mathbf{A_I} B_H + f_H^{O2} \mu_{H1} \min(\gamma_H^{O2}, \gamma_H^{DON}) B_H + (1 - f_H^{O2}) \mu_{H2} \min(\gamma_H^{NO3}, \gamma_H^{DON}) B_H - \phi_H B_H \qquad \text{Eq. 2.15}$$

where the parameters governing growth and mortality have the same meaning and values as those in equation 2.1 of the ecosystem model (see Table 2.1). The one key difference is that now there are only two, as opposed to three, heterotrophic growth terms (growth on O_2 and NO_3^-). Anaerobic growth is assumed to occur through the complete heterotrophic denitrification reaction, which converts NO_3^- to N_{2xs} directly, as opposed to first releasing NO_2^- into seawater before its subsequent reduction to N_2, as in the ecosystem model.

The biogeochemical cycles of N and O_2 are governed by tracer transport of the chemical tracers and their biological sources and sinks, which are derived from the growth and mortality rates of the heterotrophic population (in equation 2.15). The four chemical tracers (C_X, in μM; X is the tracer) simulated in the geochemical model are NO_3^-, DON, N_{2xs} and O_2. The conservation equations controlling their time-rates of change are:

$$\frac{dC_{NO3}}{dt} = \mathbf{A_I} C_{NO3} + \mathbf{A_E} C_{NO3}^E + J_{NO3}^{H1} - J_{NO3}^{H2} - \mu^{phy} \gamma_{phy}^{NO3} \qquad \text{Equation 2.16}$$

$$\frac{dC_{DON}}{dt} = \mathbf{A_I} C_{DON} + \mathbf{A_E} C_{DON}^E + \sigma J^{phy} + J^{rem} + J_{DON}^{mort} - J_{DON}^{\Sigma H} \qquad \text{Equation 2.17}$$

$$\frac{dC_{N2xs}}{dt} = \mathbf{A_I} C_{N2xs} + J_{N2xs}^{H2} - \frac{K_W}{\Delta z_0} C_{N2xs} \qquad \text{Equation 2.18}$$

$$\frac{dC_{O2}}{dt} = \mathbf{A_I} C_{O2} + \mathbf{A_E} C_{O2}^E + r_{O2} J^{phy} - J_{O2}^{H1} - K_{O2}(C_{O2} - O_2^{obs}) \qquad \text{Equation 2.19}$$

where the terms take on the same meaning and numerical values as in equations 2.8 – 2.13 and Table 2.1, except where noted below.

Since NH_4^+ and NO_2^- are not explicitly simulated, primary production is solely the result of NO_3^- assimilation, per the last term of equation 2.5. Because the autotrophic populations are also not simulated as prognostic variables, their effects on the chemical tracers are instead coupled to the growth reactions of the heterotroph through their metabolic process stoichiometries (*48*). All of the NH_4^+ released by aerobic heterotrophy (growth reaction 1; equation 2.15) is instantly converted to NO_3^- (J_{NO3}^{H1}; equation 2.16) and consumes O_2 (J_{O2}^{H1}; equation 2.19) according to the stoichiometry of the coupled heterotrophic respiration-nitrification process. NH_4^+ released by anaerobic heterotrophy (growth reaction 2; equation 2.15) is converted to N_{2xs} by the anammox reaction, and consumes a stoichiometric amount of the NO_2^- produced by NO_3^- reduction. Any NO_2^- remaining from NO_3^- reduction is instantly converted to N_{2xs}, such that the total rate of N_{2xs} production (J_{N2}^{H2}; equation 2.18) accounts for N loss from both the anammox reaction and heterotrophic denitrification, in the ratio of ~ 28:72 (*70*).

2.7.9 Diagnosing N-loss Pathways

We compared the partitioning of N loss between anammox and heterotrophic denitrification pathways in the ecosystem model to simple mass balance predictions based on the stoichiometries of those reactions. Following the method of (*79*), we track the fate of NO_2^- after the reduction of one mole of NO_3^- by heterotrophic bacteria. A fraction (x) of this NO_2^- is further reduced to N_2 by heterotrophs, a second fraction is metabolized by anammox bacteria, and the remaining fraction (α) accumulates in the water-column. Here, we modify the method slightly to incorporate into α the NO_2^- that is re-oxidized by aerobes, and the portion converted to NO_3^- during anammox. This fraction therefore represents all NO_2^- that escapes N-loss pathways by any means. Previous derivations have assumed that all $(1+3x/2)/R_N$ moles of NH_4 liberated from DON during NO_3^- and NO_2^- reduction are combined with NO_2^- by anammox (note R_N is the molar ratio of NO_3^- reduced to DON respired). Here, we also account for a fraction (β) of NH_4^- that accumulates in the water-column or is metabolized by ammonium oxidizers. The NO_2^- balance of these chemical reactions can then be solved for x, provided α and β are known:

$$x(\alpha,\beta) = \frac{1-(1-\beta)/R_N - \alpha}{1+(3/2)(1-\beta)/R_N}$$ Equation 2.20

The number of moles of N_2 gas produced by heterotropic denitrification is then given by:

$$N_2^H = x/2$$ Equation 2.21

and N_2 production by anammox is:

$$N_2^{AX} = 1.02(1-\beta)(1+3x/2)/R_N$$ Equation 2.22

where 1.02 is the empirical molar ratio of N_2 produced to NH_4^+ consumed by anammox (*88*). These equations can then be combined to predict, from α and β alone, the contribution of anammox to overall N-loss:

$$f_{amx} = \frac{N_2^{AX}}{N_2^{AX} + N_2^H}$$ Equation 2.23

and the overall stoichiometry of anaerobic respiration (moles N-N_2 produced / moles DON respired):

$$R_{N-loss} = 2\frac{N_2^{AX} + N_2^H}{(1+3x/2)/R_N}$$ Equation 2.24

We diagnosed the α and β terms from our ecosystem-ocean simulations: α is computed as the difference between the rates of NO_3^- and NO_2^- reduction, normalized to the rate of NO_3 reduction, and β is the difference between anaerobic NH_4^+ production and anammox, normalized to the anaerobic NH_4^+ production rate:

$$\alpha_{GCM} = \frac{J_{NO3}^{H2} - J_{NO2}^{H3} - J_{NO2}^{AX}\rho_{NO2}^{AX}}{J_{NO3}^{H2}} \quad \text{Equation 2.25}$$

$$\beta_{GCM} = \frac{J_{NH4}^{H2} + J_{NH4}^{H3} - J_{NH4}^{AX}\rho_{NH4}^{AX}}{J_{NH4}^{H2} + J_{NH4}^{H3}} \quad \text{Equation 2.26}$$

where the J terms are defined above in the description of the chemical cycles, and $\rho_{\mathrm{NO2}}{}^{\mathrm{AX}}$ and $\rho_{\mathrm{NH4}}{}^{\mathrm{AX}}$ are the fractions of NO_2^- and NH_4^+ uptake by anammox that goes to N_2, as opposed to NO_3^- and biomass, respectively.

Ecosystem model simulations conform exactly to the predictions of Eqs. 2.23 and 2.24 when accounting for variability in both the mass balances of NH_4^+ and NO_2^- (β and α terms, respectively) (Figure 2.11). However, since NO_2^- is the main factor driving the higher f_{amx} values, the lower rates of N-loss, and the larger ODZ in the ecosystem model, we focus on the effect of variations in its balance (α) in Figure 2.3. This is done by normalizing the diagnosed model values to the case in which no NH_4^+ escapes anammox (i.e. β = 0).

2.7.10 Sensitivity Tests

We performed a suite of ecosystem model simulations to estimate uncertainty in poorly known model parameters and test the robustness of our central result, the dilution of N loss across a larger ODZ, against their uncertainty. Model parameters were inferred by integrating an additional 89 simulations in the GCM (Table 2.1). We used observations of the chemical tracers to define a cost function that selects for realistic model solutions and generates an ensemble that is used for uncertainty statistics and model error bars provided in the main text. Simulations were initialized using the decadal-mean output from the end of the 250 year standard run spin-up, allowing for 25-year integrations to steady-state. Simulations varying the exponent of the particle flux (b) were spun-up as for the standard model. The results of these experiments are discussed below.

The values of microbial kinetic parameters, including growth and mortality rates, O_2 tolerances, and nutrient half-saturations, were taken from laboratory experiments, wastewater treatment studies and in situ measurements where available (Table 2.1). To account for uncertainty in growth and mortality rates, and half-saturation constants, we varied their values by at least a factor of two and an order of magnitude above and below their standard model values (14 parameters, 83 simulations). We also varied the O_2 sensitivity of anammox from 1-15 μM for anammox and the critical threshold for heterotrophic denitrification (O_2^{crit}) from 1-10 μM, yielding an additional 4 simulations. Finally, we inferred the depth attenuation coefficient of the particle flux (b) by varying its value across the range observed for oxic and anoxic water (0.4-0.858). 43 of the 89 simulations can reproduce all tracer distributions simultaneously (Figure 2.1).

The O_2 threshold for denitrification exerts the largest effect of all parameters on the volume of the ODZ and its rates of N loss, but never reverses the trend between the ecosystem and geochemical models, as discussed in the main text (Figure 2.2). Across the simulated range in O_2^{crit} (1-10 μM), the volume of the ODZ ($O_2 < O_2^{crit}$) varies from .75-2.2 x 10^{15} m^3, and the rate of N loss from 2.6-0.9 μM N y^{-1}. In contrast, for the scenario in which O_2^{crit} = 5 μM, the predicted range in the volume of the ODZ and rates of N loss from all model other simulations is only 1-1.4 x 10^{15} m^3 and 2.2-1.3 μM N y^{-1}, respectively (Figure 2.7). For the above mentioned reasons and because the value of O_2^{crit} cannot be inferred directly from the chemical tracers, we provide the range of model predictions for different values of O_2^{crit} in the main text, and use the simulations that vary other ecosystem parameters to estimate uncertainty at a given O_2^{crit}.

Regardless of microbial physiological parameter values, the ecosystem model also predicts a higher contribution of anammox to total N loss (Σf_{amx}) than the 0.28 assumed in geochemical models, as a result of NO_2^- reoxidation in the suboxic zone (Figure 2.9). In contrast to ODZ volume and N loss, Σf_{amx} is not most sensitive to the O_2 threshold for denitrification. Across the range in O_2^{crit}, Σf_{amx} varies from 0.36 to 0.4, whereas across all other experiments Σf_{amx} varies from 0.31 to 0.49. Anammox bacteria's mortality and nutrient half-saturations exert the strongest influence, with low mortality rates allowing for the maximum Σf_{amx}, and a high NO_2^- half-saturation (K_{NO2} = 3 μM) leading to the minimum Σf_{amx}. As K_{NO2} increases, anammox bacteria have a higher propensity for NO_2^- limitation, which increases the likelihood of being outcompeted by NO_2^- oxidation in the suboxic shell, where Σf_{amx} reaches its spatial maximum (Figure 2.3). We chose K_{NO2} = .1

μM as our standard model case, yielding $\Sigma f_{amx} \sim 0.4$, both because this K_{NO2} value best reproduces observed uptake kinetics (*89*), and because it ensures NH_4^+ limitation of anammox (mean ODZ NO_2^- = .45 μM), which is implied by all available evidence (*17*), including water-column NH_4^+ addition experiments from within the simulated region (*51*).

2.7.11 Ocean Data

We use observed distributions of the chemical tracers (Figure 2.6) to define a cost function that sorts model solutions based on whether they reproduce key features of the ODZ. For a simulation to be used in uncertainty calculations, Root Mean Square Errors (RMSE) between model and data profiles must be less than a predefined threshold for all chemical tracers in which observations are available (Table 2.2). RMSE thresholds are determined by requiring the simulated ODZ to have no detectable NH_4^+ (*70*), contain realistic subsurface accumulations of NO_2^- (*60*) and N_{2xs} gas (*78*), and a mean profile of NO_3^- that displays little gradient with depth in the upper thermocline (~ 200 – 400 m) (*69*) (Figure 2.6). Chemical tracers are averaged around the data-locations shown in Figure 2.6B. Uncertainty in the observed regional profile of NO_2^- precludes selecting against models with zero subsurface accumulation. To rule out these unrealistic scenarios with our cost function we instead compute the RMSE and mean NO_2^- profiles (Figure 2.1, 2.6) by only considering those that contain a well-defined secondary NO_2^- maximum, here defined as NO_2^- concentrations exceeding 1 μM below 100 m. For O_2, the cost function selects for ODZs that become functionally anoxic for upwards of 100 meters in the vertical, which is a conservative requirement given the observed distribution of anoxia within the ETNP (*66*). NH_4^+ levels below 15 nM are set to the observational detection limit (NH_4^+ ~ 10 nM; Bonnie Chang, personal communication) in both the observations and model output.

Observed annual mean concentrations of O_2 and NO_3^- from the 2009 World Ocean Atlas (*69*) were used as initial conditions and transported into the domain at its open boundaries. For chemical tracers whose large-scale distributions are not available from observations (e.g. NH_4^+), ecosystem model equilibria were used to generate initial and boundary conditions

In Figure 2.4, volumes of low O_2 water were computed from the monthly climatology of (*69*) by summing over grid cells containing O_2 levels less than a predefined threshold for each month and then averaging over 12 months. For model-data comparisons, the annual mean O_2 climatology is binned to the model grid. The correction of (*50*) is applied to all WOA09 O_2 data used in the study to more accurately represent the true volume of the ODZs.

2.8 Figures

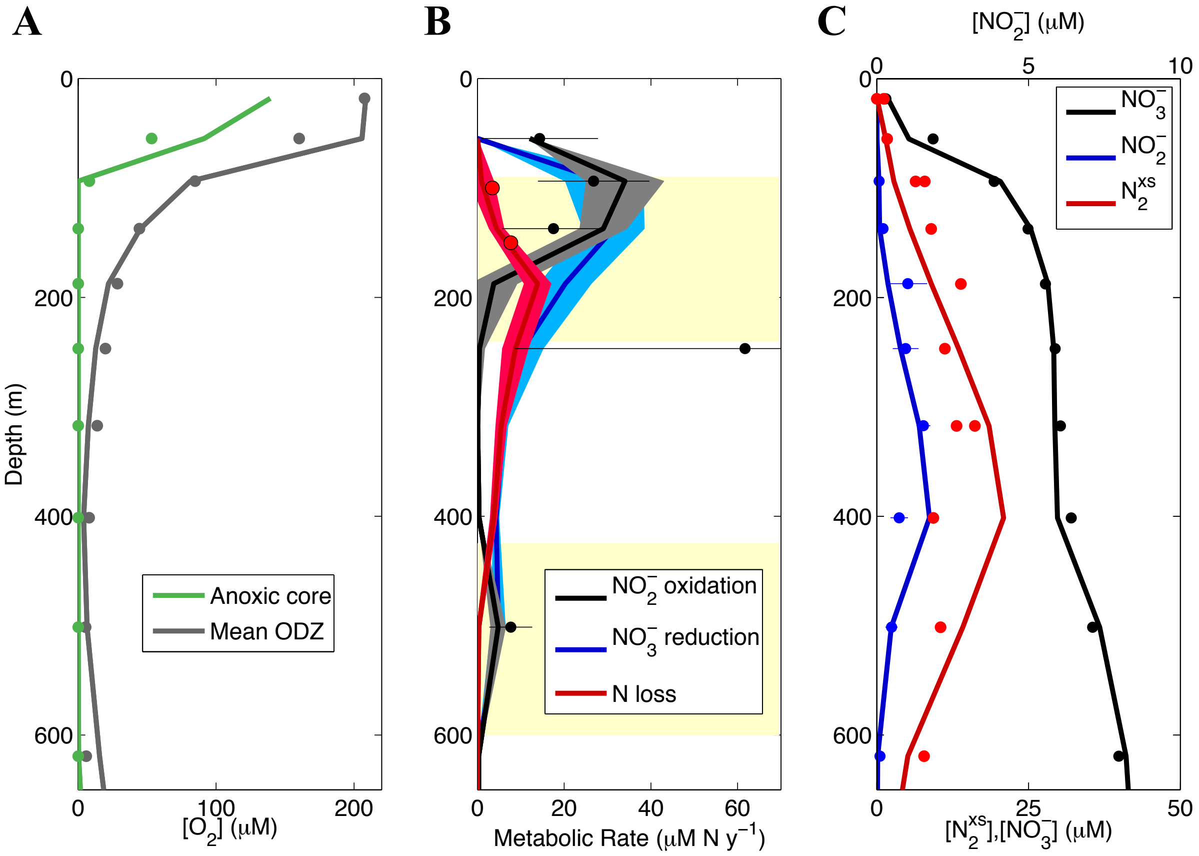

Figure 2.1 Chemical distributions and metabolic rates from the eastern tropical North Pacific ODZ. Observations (points) are shown with the mean model simulated value (lines) and the standard deviation (shading) among 43 model simulations with different microbial parameters that reproduce all chemical data (Section 2.7 Supplemental Methods). (A) Depth profiles of O_2 concentrations taken through the core of the ODZ and averaged over its horizontal extent (Figure 2.6). The ODZ core profile is computed as the minimum O_2 concentration on a given depth surface. Uncertainty in modeled chemical tracer distributions is smaller than the line thickness. Green points are measurements from the anoxic core made using a high precision STOX sensor at station BB2 (*66*). Grey points are from the World Ocean Atlas (WOA) annual climatology (*69*). (B) Depth profiles of metabolic rates from the core of the ODZ. The coexistence of aerobic and anaerobic processes is marked by off-white bands. NO_2^- oxidation measurements from station 3 of (*55*) and the offshore stations of (*58*) are averaged onto the model grid, and their standard error is displayed as horizontal black lines. A single rate outlier lies outside the range displayed (~124 μM N y^{-1} at 190 m). Observed N loss rates are from offshore in situ particle incubation experiments (*70*). Metabolic rates were not used for model vetting, and thus provide an independent check on the ecosystem model parameters. (C) Depth profiles of nitrogen compounds (μM N) averaged over the regions shown in Figure 2.6. Uncertainty in modeled chemical tracer distributions is smaller than the line thickness. The standard error of NO_2^- observations is shown as horizontal blue lines. Simulated NH_4^+ concentrations (not shown) are at or near the observable detection limit (~ 10 nM), in agreement with the measurements presented in Figure 2.6. The NO_2^- data are from (*60*), NO_3^- data are from the WOA annual climatology (*69*), and excess N_2 gas measurements are from (*78*).

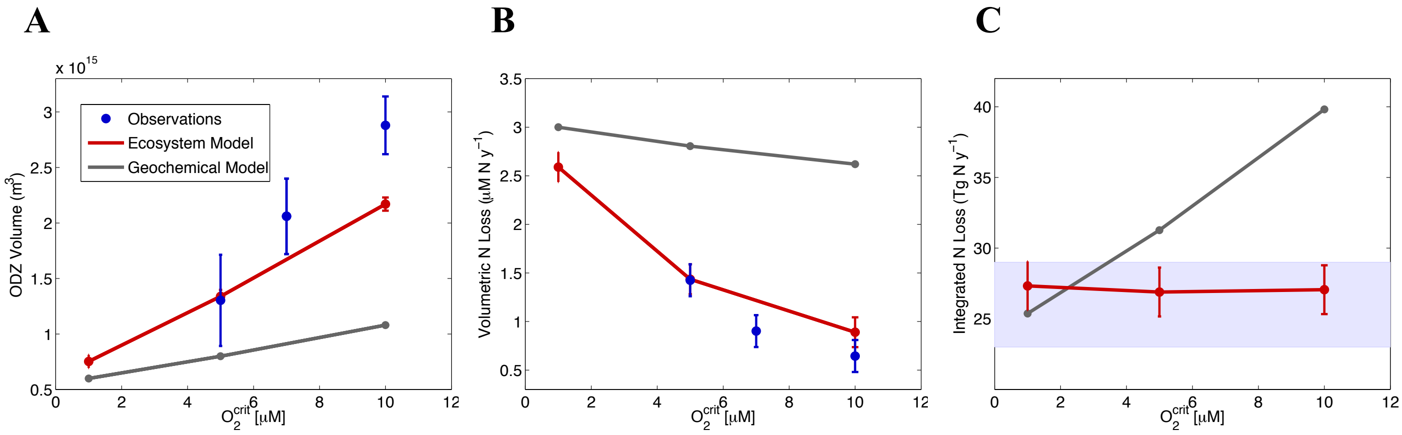

Figure 2.2. (A) Annual mean ODZ volume, and (B) the volumetric and (C) integrated rates of N loss from observations and predicted by the microbial ecosystem and geochemical models, as a function of the critical O_2 threshold for denitrification (O_2^{crit}). ODZ volume is computed as the volume of water with $O_2 < O_2^{crit}$ in the upper 700 m, where the rate of N loss is large. Error bars on observed volumes represent their monthly standard deviations. Observed volumetric rates are computed by dividing the total rate of N loss (*20*) by the observed annual ODZ volumes in (A). Error in the observed volumetric rates represents the 1-σ uncertainty in the total rate of N loss, which is shown as greyish blue shading in (C). Ecosystem model error bars are computed as the standard deviation among data-fitting simulations for the scenario in which $O_2^{crit} = 5$ μM (Figure 2.7).

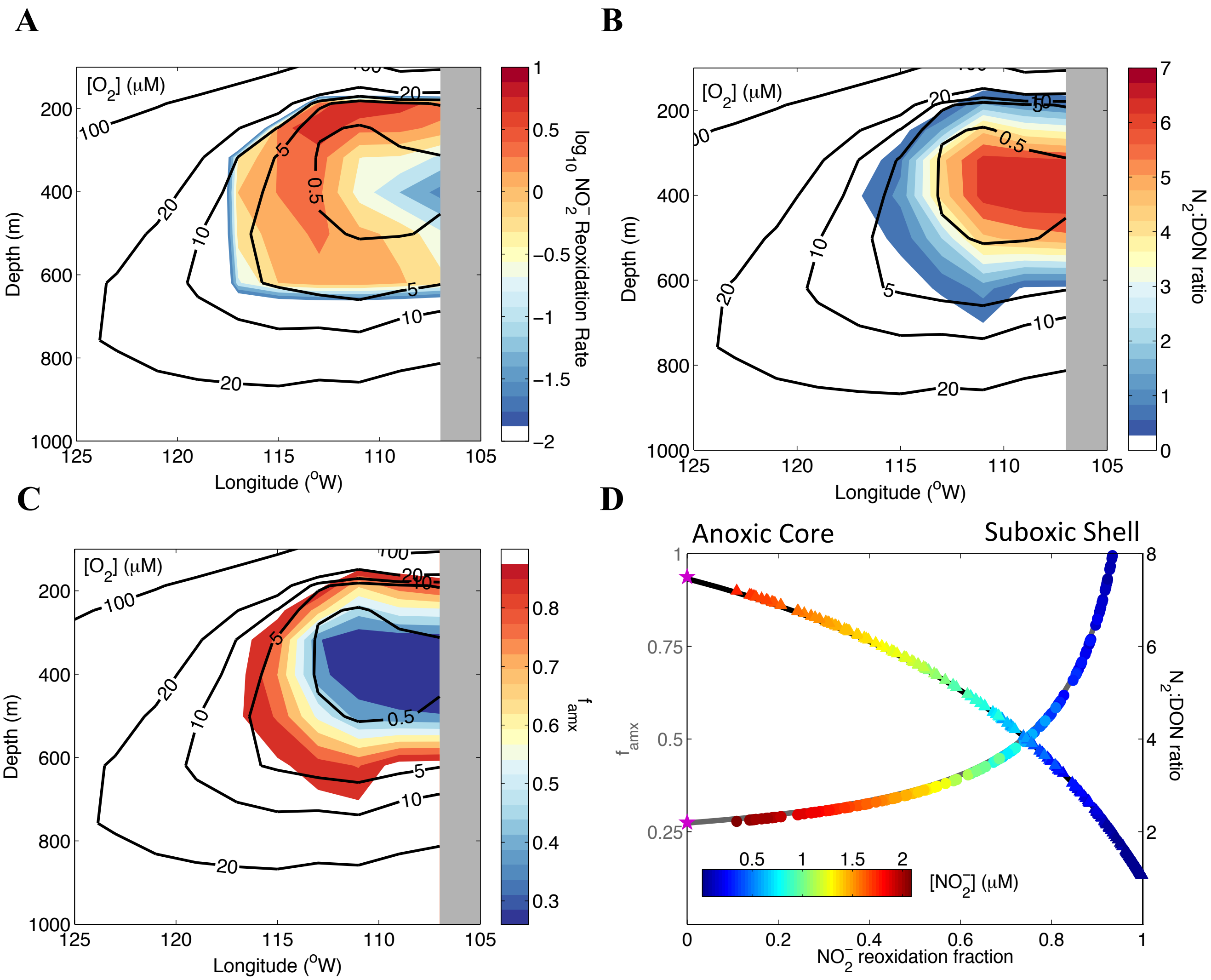

Figure 2.3. Zonal mean ODZ cross-sections of the NO_2^- reoxidation rate (μM N y^{-1}) (A), the ratio of total N_2 produced per mole of DON remineralized via denitrification (N_2:DON ratio; units of mol N-N_2/mol N-DON) (B), and the contribution of anammox to total N loss (*f*amx) (C) from the standard ecosystem model scenario. NO_2^- reoxidation is defined as NO_2^- that is produced from NO_3^- during the first step of heterotrophic denitrification, but is oxidized back to NO_3^- during nitrification. Note the $\log_{10}$ scaling of NO_2^- reoxidation rates in (A). Rates and ratios are overlain by time-mean O_2 concentrations (contours). Grey shading denotes the eastern boundary of the Pacific Ocean. N_2:DON ratios (triangles) and f_{amx} (circles) versus the NO_2^- reoxidation fraction from the standard ecosystem model scenario (D). The NO_2^- reoxidation fraction includes the accumulation of NO_2^- (colors) in the anoxic core, which is eventually reoxidized to NO_3^- in the suboxic shell. Model values conform to steady-state predictions (lines; grey for *f*amx and black for N_2:DON) based on the known reaction stoichiometries (*79*) (Section 2.7 Supplemental Methods). Values predicted by geochemical models are shown as purple stars.

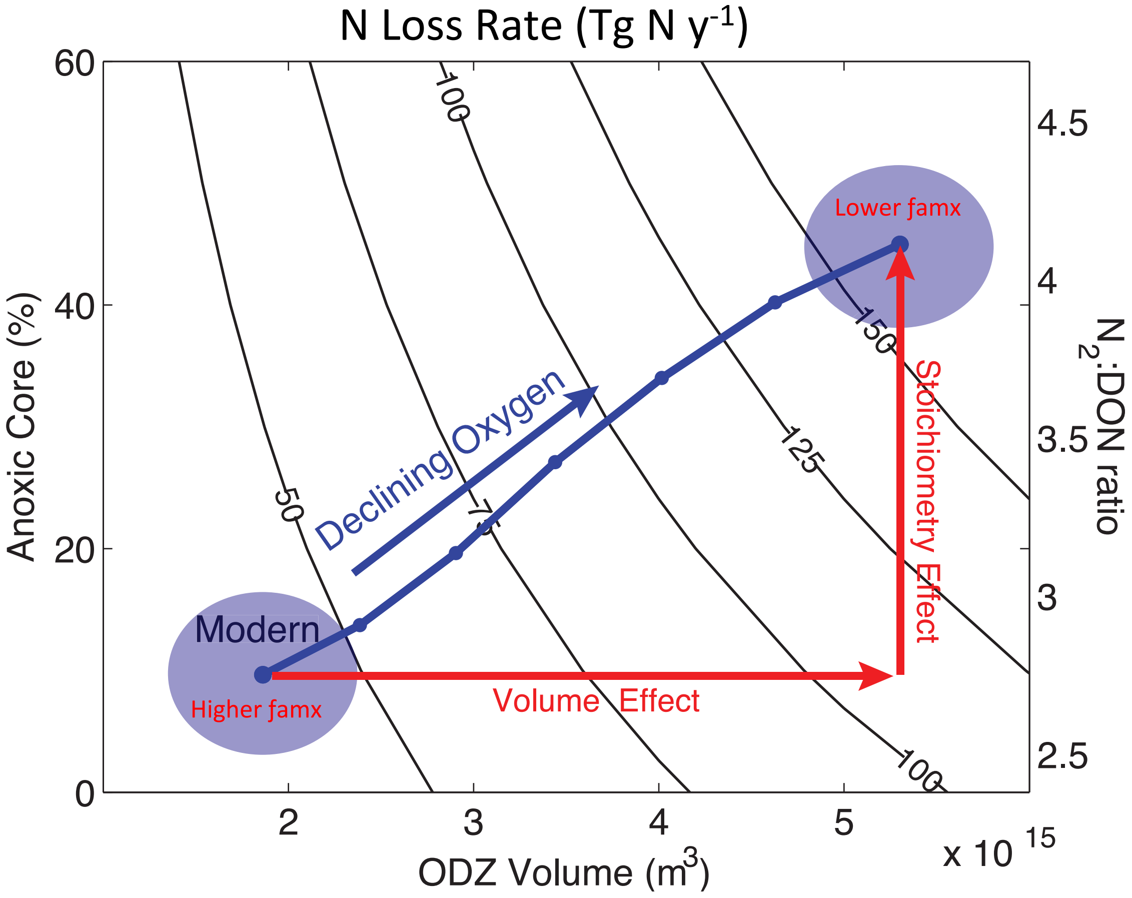

Figure 2.4. Predicted rates of N loss in the Pacific Ocean (contours; Tg N y^{-1}) for a given ODZ volume, anoxic percentage, and ratio of total N_2 produced per mole of DON remineralized via denitrification (N_2:DON ratio; units of mol N-N_2/mol N-DON). N loss rates are computed as: $J^{N2} = J^{DON}(r^{anx}V^{anx}+r^{sub}V^{sub})$, where r^{anx} is the N_2:DON ratio in the anoxic core (6.2), r^{sub} is the N_2:DON ratio in the suboxic shell (2.4), J^{DON} is the mean anaerobic remineralization rate (7.6 x 10^{-15} Tg N m^{-3} y^{-1}), and V^{anx} and V^{sub} are potential volumes (m^3) of anoxic and suboxic waters, respectively. N_2:DON ratios and rates of anaerobic DON remineralization are diagnosed from the standard ecosystem model scenario. The solid blue line is the relationship between annual mean ODZ volume and its anoxic percentage in the Pacific Ocean, as derived from the World Ocean Atlas climatology (*69*), assuming the ODZ starts at O_2 < 5 µM. Uncertainty in modern ocean values (blue shading around the leftmost point) is calculated as the standard deviation across monthly observations, and is propagated to the deoxygenated ODZ. Potential volumes and anoxic percentages (points to the right of modern) are calculated from observations by subtracting O_2 in increasing 1µM increments in a spatially uniform pattern. The component of N loss change that results from a change in mean N loss stoichiometry is indicated by the vertical red vector, while the component that results from a total volume change is indicated by the horizontal vector.

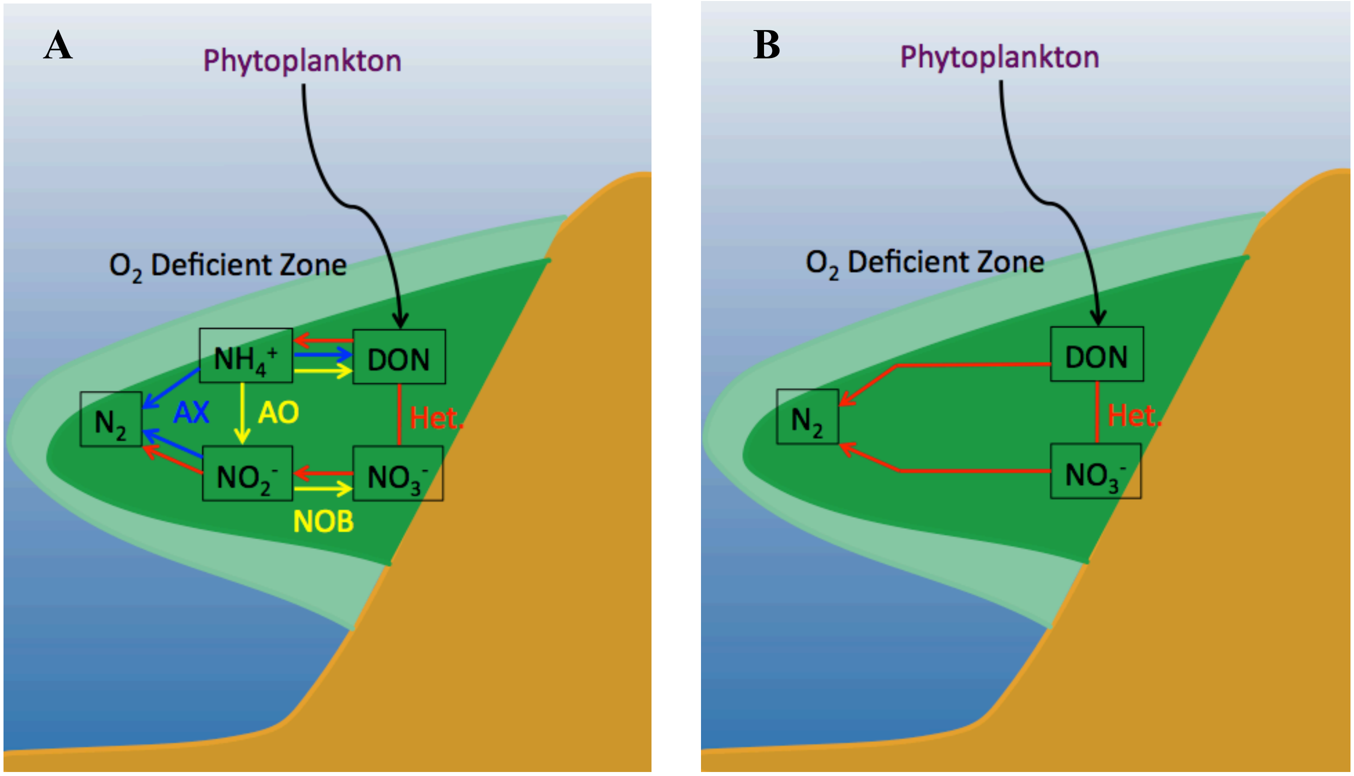

Figure 2.5. Schematic diagrams of the microbial ecosystem (A) and geochemical (B) models. Chemical tracers are represented by black boxes, and their ecosystem fluxes by colored arrows. Het. is heterotrophic bacteria, AO is ammonia oxidizers, NOB is nitrite oxidizing bacteria, AX is anammox bacteria.

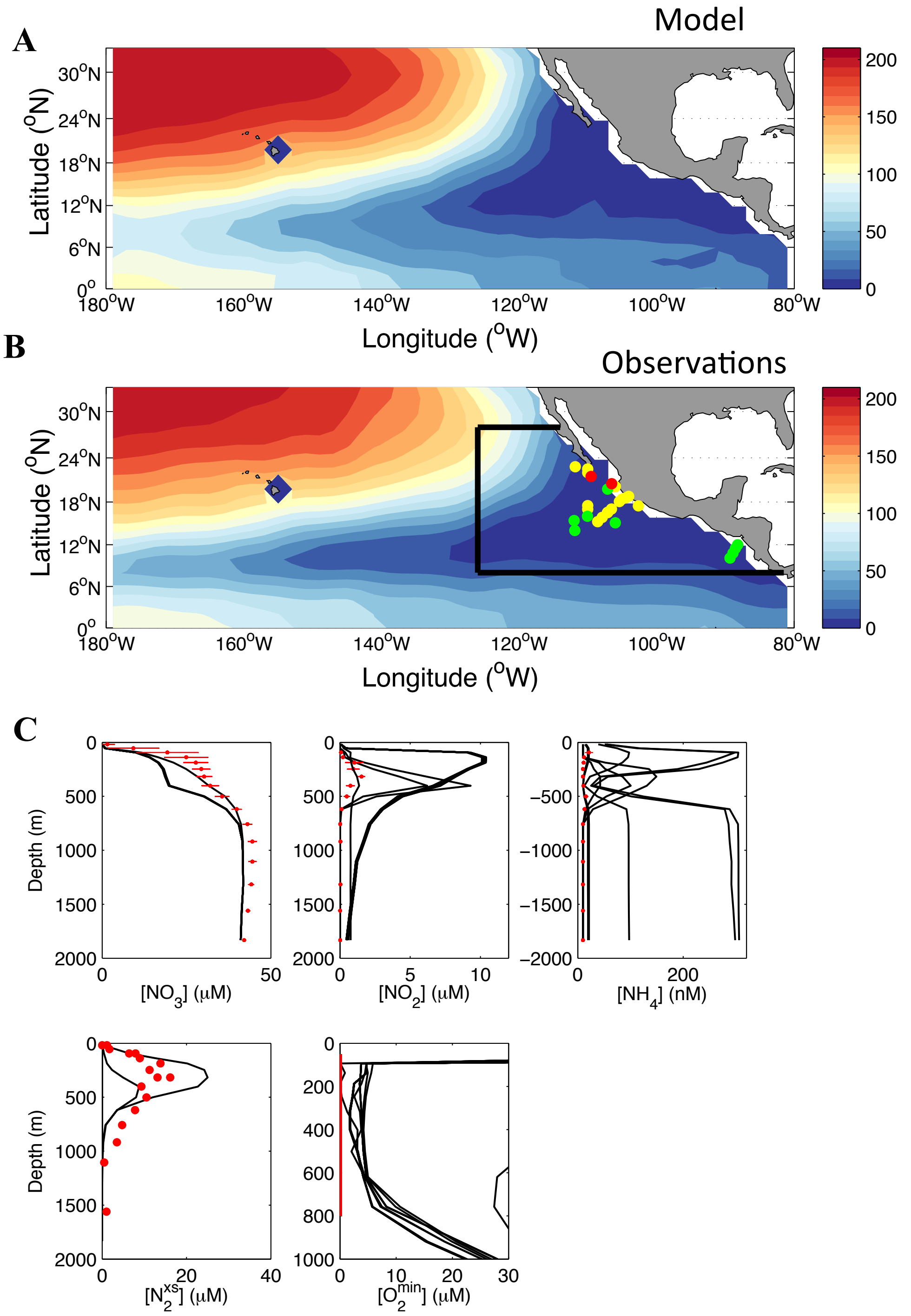

Figure 2.6. (A) Modeled and (B) observed O_2 distributions averaged from 115 to 700 m. Locations of N_2^{xs} gas (red), NH_4^+ (yellow), and NO_2^- (green) data used in this study to constrain ecosystem simulations are overlain as points in (B). Model profiles of N_2^{xs}, NH_4^+, and NO_2^- are averaged around these locations. Observed and modeled NO_3^- and O_2 profiles are averaged within the region outlined by the black box, which contains the maximum horizontal extent of the ODZ and has complete data coverage for these tracers. (C) Depth profiles of model tracers (black lines) from simulations that do not reproduce observations (red). NO_3^- error bars are spatial standard deviations. NO_2^- and NH_4^+ error bars are spatial standard errors. Modeled O_2^{min} is computed as the horizontal minimum O_2 concentration at each depth.

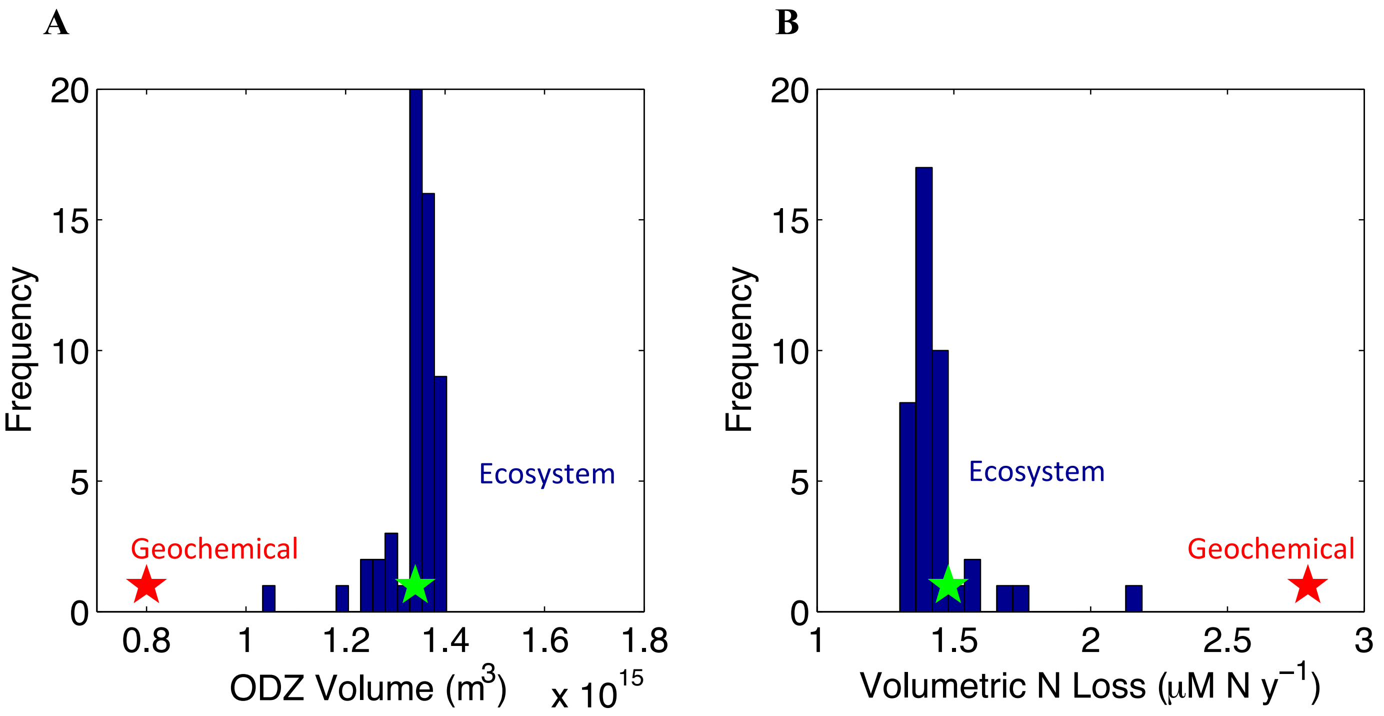

Figure 2.7. Time-mean ODZ properties. Histograms of (A) total ODZ volume and (B) the volumetric rate of N loss from data-reproducing ecosystem models for the scenario in which O_2^{crit} = 5 μM. Red stars indicate values predicted by the geochemical model. Green stars mark the values from the standard model whose spatial patterns are analyzed in the main text.

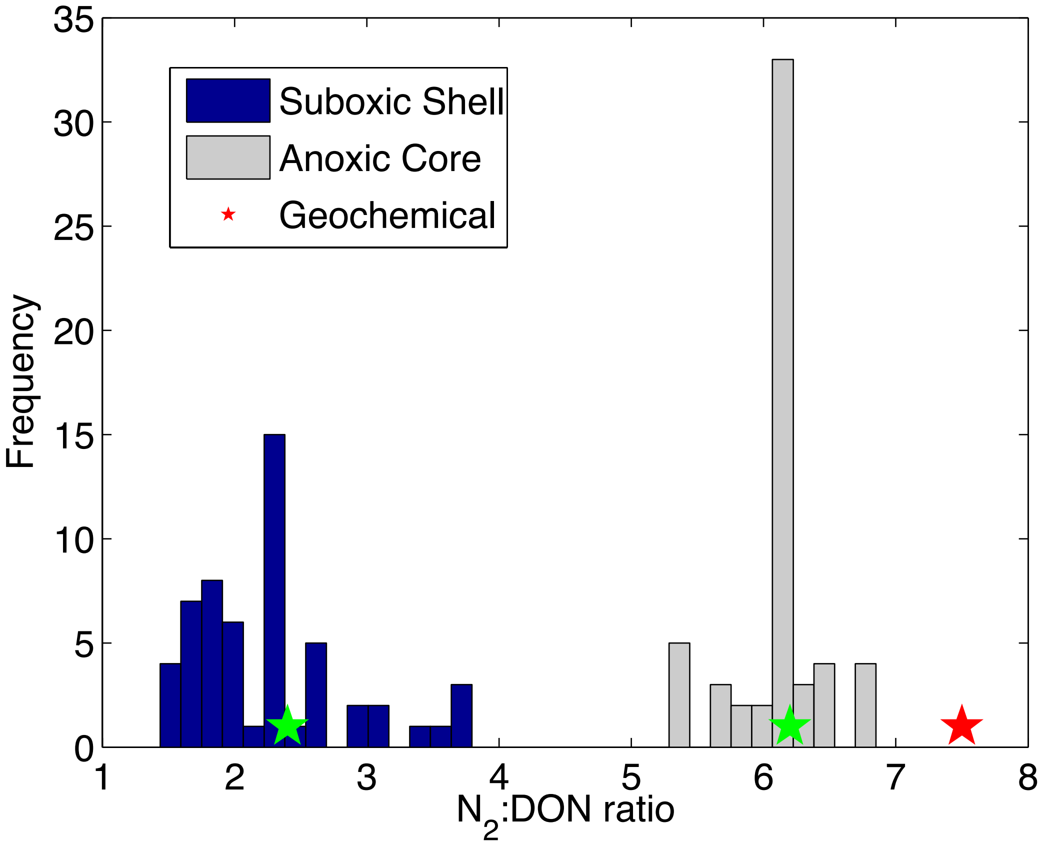

Figure 2.8. Histograms of the ratio of total N_2 produced per mole of DON remineralized via denitrification (N_2:DON ratio; units of mol N-N_2/mol N-DON) in the suboxic shell (blue) and anoxic core (grey) from data reproducing ecosystem models for the scenario in which O_2^{crit} = 5 μM. The red star indicates the value predicted by the geochemical model. Green stars mark the values from the standard model that is analyzed in the main text.

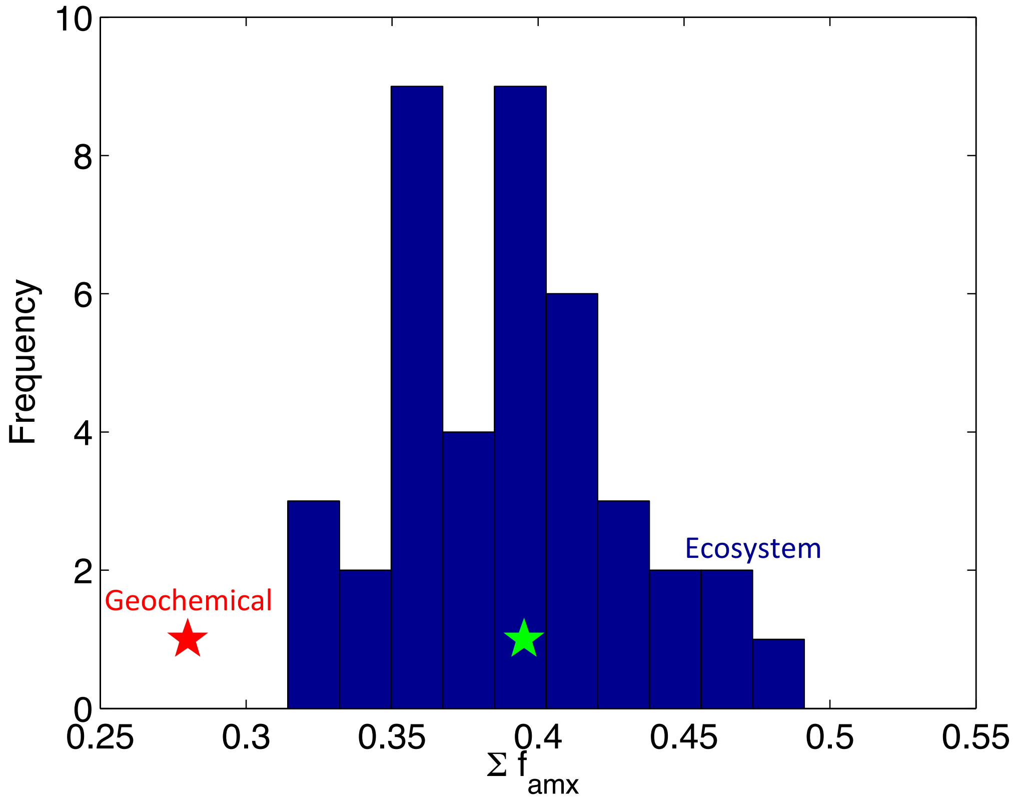

Figure 2.9. The total contribution of anammox to N loss (f_{amx}) across data reproducing scenarios for the case in which O_2^{crit} = 5 μM. The geochemical model is marked as the red star. The green star marks the value of the standard model whose spatial patterns are analyzed in the main text. In all scenarios famx is greater than the 0.28 predicted by the geochemical model.

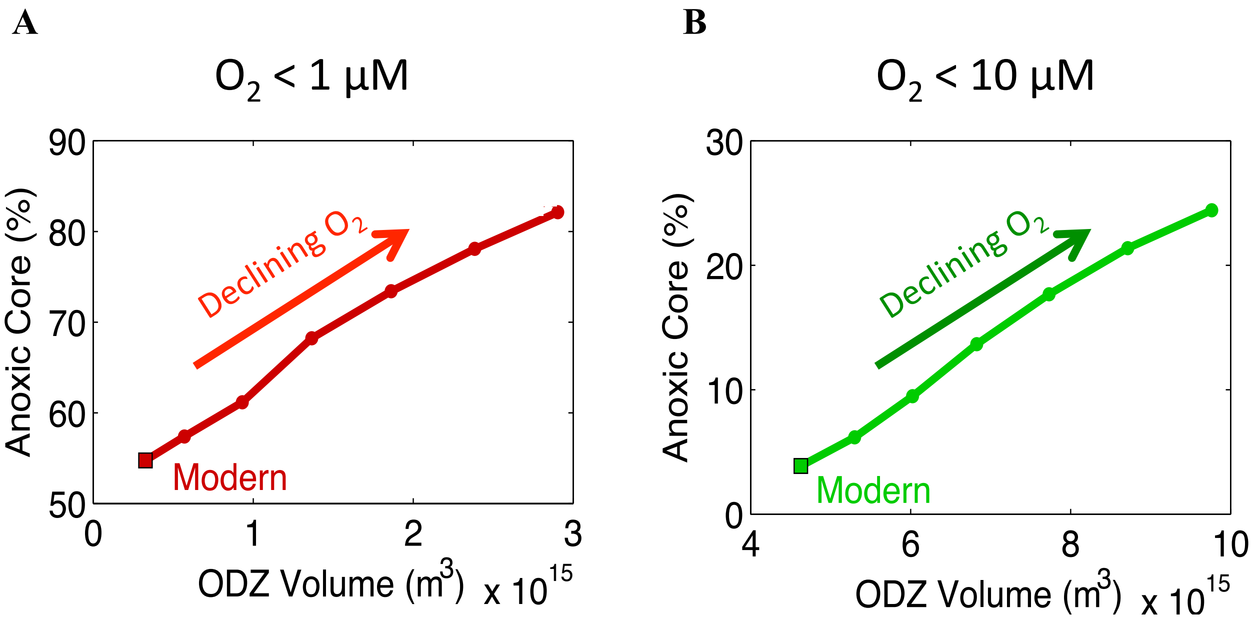

Figure 2.10. The relationship between annual mean ODZ volume and anoxic percentage in the Pacific Ocean, as derived from the World Ocean Atlas climatology (*69*), assuming the ODZ starts at $O_2 < 1$ µM (A) and $O_2 <$ 10 µM (B). Modern ocean values are marked by squares. Potential volumes and anoxic percentages (circles) are calculated from observations by subtracting O_2 in increasing 1 µM increments in a spatially uniform pattern. Note the different axes scales. The anoxic fraction of the ODZ increases as its total volume grows regardless of the exact O_2 threshold that defines the ODZ.

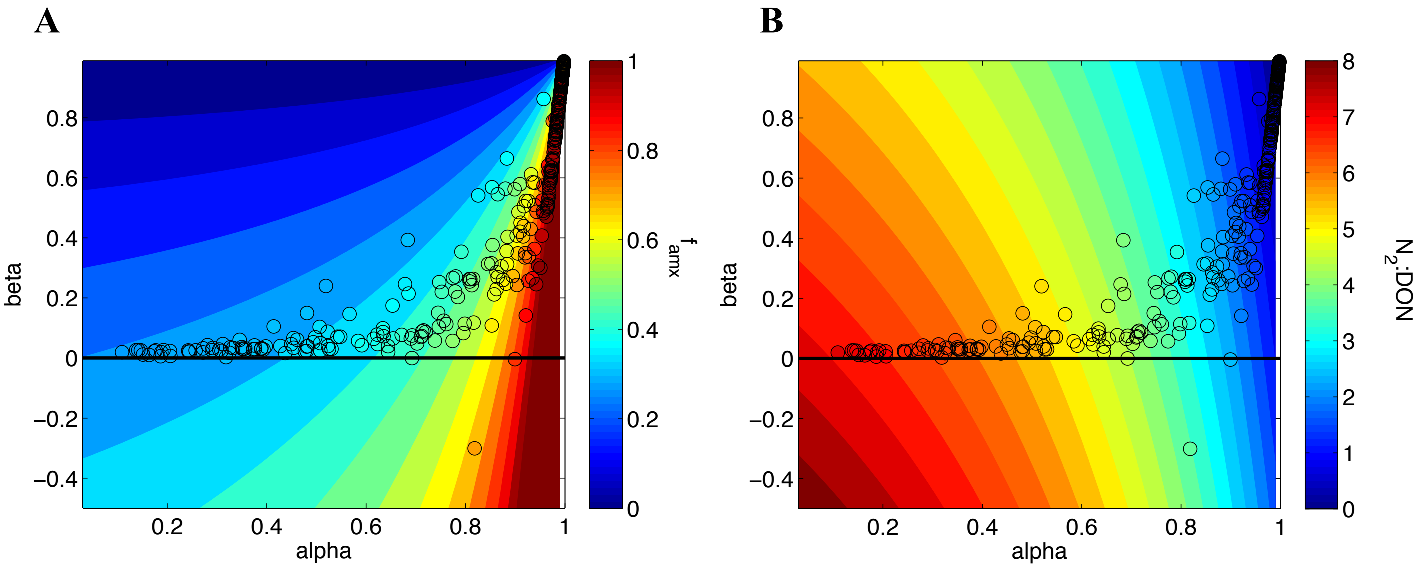

Figure 2.11. Diagnosed ecosystem stoichiometry. Variations in (A) f_{amx} and (B) the molar ratio of total N_2 produced to DON remineralized via denitrification (N_2:DON; units of mol N-N_2/mol N-DON). Colored circles are values diagnosed from grid cells of the standard model simulation analyzed in the main text. Colored contours are predicted from metabolic reaction stoichiometries (Section 2.7 Supplemental Methods). α and β are the respective fractions of NO_2^- and NH_4^+ that escape conversion to N_2^{xs}. In Figure 2.3D, diagnosed model values have been normalized to conform to $\beta = 0$ (black line) by subtracting out the difference between predicted values at diagnosed β and at $\beta = 0$.

2.9 Tables

Table 2.1. Ecosystem model parameters.

Parameter	Symbol	Units	Standard Value[a]	Posterior Range[b]	References
e^- fraction to cell synthesis	θ_s	Dimensionless	0.67 H 0.19 AX 0.15 AO 0.04 NOB		H, AO, NOB: (*82*) AX: (*88*)
Maximum growth rate	μ_{xy}	d^{-1}	2.0 H1 1.27 H2 1.85[c] H3 0.08[c] AX 0.65[c] AO 0.65[c] NOB	0.93 - 1.85 (H3) 0.04 - 0.08 (AX) 0.65 – 6.5 (NOB)	H: (*82*, *86*) AX: (*63*) AO: (*90*) NOB: (*91*)
Mortality rate	ϕ	d^{-1}	0.62[d] H 0.005[c] AX 0.045[c] AO 0.045[c] NOB	0.31 - 0.93 (H) 0.0025 - 0.01 (AX) 0.0045 - 0.045 (NOB)	H: (*82*, *92*) AX: (*93*) AO, NOB: (*82*, *91*)
O_2 half-saturation	K^{O2}	nM	20.0		(*62*, *65*, *66*)
Critical O_2 threshold for heterotrophic denitrification	O_2^{crit}	μM	5.0[e]	1 - 10	(*13*, *18*, *59*, *60*)
50 % O_2 inhibition of anammox	K_{O2}^{inh}	μM	8.1[e]	1 - 15	(*62*, *64*)
DON half-saturation	K_{DON}^{H}	μM	0.5		(*86*)
NH_4^+ half-saturation	K_{NH4}	nM	92[c] AX 133.0[c] AO 80.0[c] NOB	46-184 (AX) 8-80 (NOB)	AO: (*90*) AX: (*63*)
NO_2^- half-saturation	K_{NO2}	μM	10[d] H3 0.09[f] AX 0.08[g] NOB	5 - 20 0.009 - 3 0.008 - 0.8	H: (*94*) AX: (*63*, *89*)
NO_3^- half-saturation	K_{NO3}	μM	3.23 H2 1.25 Phy		H: (*95*) Phy: Estimated from surface NO_3^- (*69*)
Depth attenuation coefficient	b	dimensionless	0.6[e]		(*20*, *83*)
Phytoplankton uptake rate of NO_3^-	μ^{phy}	N d^{-1}	0.077		Estimated from surface NO_3^- (*69*)
Phytoplankton uptake rate of NH_4^+ and NO_2^-	k^{phy}	d^{-1}	0.143		
Fraction of production to DON	σ	dimensionless	0.5		
Piston Velocity	K_W	m d^{-1}	3.0		(*20*)
O_2 restoration rate	K_{O2}	d^{-1}	0.143		

[a] Standard value column refers to the parameters of the model analyzed in the main text. [b] The posterior range column provides the range of parameter values that fit the ocean data and are used in uncertainty calculations. Where no range is given, only the standard value reproduces the data. [c] Parameters that are varied by an order of magnitude around their standard values. [d] Same as [c], but parameters are additionally co-varied by 50% of their standard values. [e] Parameters that are varied over the observed range detailed in text

section S5. [f] Same as [c], but additionally run with K_{NO2} = 3 μM. [g] Same as [c], but additionally run with K_{NO2} = 10 μM.

Table 2.2 Cost function root mean square error (rmse) thresholds.

Tracer	**rmse threshold (μM)**	**Data source**
O_2	–––	(*66*)[a]
NH_4^+	.005	Bonnie Chang, unpublished data
NO_2^-	1	(*60*)
NO_3^-	3.2	(*69*)
N_2^{xs}	5	(*78*)

[a] O_2 is required to fall below 0.1 μM for at least 100 meters in the vertical.

Chapter 3

Microbial ecosystem dynamics drive fluctuating nitrogen loss in marine anoxic zones

3.1 Abstract[2]

The dynamics of nitrogen (N) loss in the ocean's oxygen deficient zones (ODZs) are thought to be driven by climate impacts on ocean circulation and biological productivity. Here we analyze a data-constrained model of the microbial ecosystem in an ODZ and find that species interactions drive fluctuations in local and regional scale rates of N loss, even in the absence of climate variability. By consuming O_2 to nanomolar levels, aerobic nitrifying microbes cede their competitive advantage for scarce forms of N to anaerobic denitrifying bacteria. Because anaerobes cannot sustain their own low-O_2 niche, the physical O_2 supply restores competitive advantage to aerobic populations, resetting the cycle. The resulting ecosystem oscillations induce a unique geochemical signature within the ODZ — short-lived spikes of ammonium similar to variability found in measured profiles. The microbial ecosystem dynamics also give rise to variable ratios of anammox to heterotrophic denitrification, providing a mechanism for the unexplained variability of these pathways observed in the ocean.

---

[2] An edited version of this chapter was published as Penn, J.L., Weber T., Chang B.X., and Deutsch C. (2019), Microbial ecosystem dynamics drive fluctuating nitrogen loss in marine anoxic zones, *Proceedings of the National Academy of Sciences*, 116 (15) 7220-7225, https://doi.org/10.1073/pnas.1818014116

3.2 Introduction

Bioavailable nitrogen (N) is a key macronutrient that limits the rates of biological activity. In the ocean, the concentration of nitrate (NO_3^-), the major form of bioavailable N, is reduced by anaerobic reduction to biologically inert N_2 gas within small subsurface O_2-deficient zones (ODZs) (*17*). The volumetric rate of N removal within these zones is limited by the downward flux of organic matter from sinking particles (*70*). In turn, ODZ volumes are strongly dependent on the regional O_2 content of the thermocline in which they reside (*36*). Variations in climate have major impacts on the supply of O_2 and organic matter to the ODZ, driving changes in the magnitude of N removal across a wide spectrum of timescales, from months to millennia (*37*, *54*, *96*).

Microbial community structure also plays a major role in regulating N_2 gas production. Anaerobic processes, such as anammox and heterotrophic denitrification, can tolerate up to micromolar amounts of O_2, allowing them to coexist with aerobic nitrifying microbes, which become limited by O_2 only at nanomolar concentrations (*14*, *18*, *60*, *62*, *64–66*, *70*, *97*). Because both anaerobic and aerobic metabolisms utilize the key N-cycle intermediates ammonium (NH_4^+) and nitrite (NO_2^-) as substrates, their coexistence results in resource competition whose outcome is determined by nanomolar variations in O_2 (Chapter 2). When nitrification is dominant, the reoxidation of partially denitrified NO_2^- to nitrate (NO_3^-) reduces the magnitude of N_2 production and increases O_2 consumption; when aerobic nitrifiers are excluded by O_2 scarcity, NO_3^- is efficiently reduced all of the way to N_2 (Chapter 2 and ref. *77*). Here we demonstrate that resource competition between aerobic nitrifiers, anaerobic denitrifiers, and anammox bacteria can also lead to regional-scale temporal variability in the rates of N and O_2 cycling, even with constant physical fluxes of O_2 and organic matter into the ODZs.

3.3 Methods

To examine the role of microbial interactions in the dynamics of fixed N loss, we analyzed a microbial ecosystem model (Chapter 2) embedded within an ocean general circulation model (*98*). The steady three-dimensional ocean circulation is optimized to fit tracer observations (temperature, salinity, radiocarbon, and CFC- 11), implying realistic ventilation rates and pathways of the ODZs (*68*). We focus on the world's largest ODZ, in the eastern tropical North Pacific (ETNP) (*16*), by restricting the boundaries of the model from the equator to 35° N, the coast to 180° W, and the surface ocean to 2,000 m depth. Observed annual mean concentrations of O_2 and NO_3^- (*69*) are transported into the domain at its open boundaries to ensure their realistic supply to the ODZ region. The circulation does not vary over time, leaving microbial ecosystem dynamics as the sole source of temporal variability.

The microbial ecosystem model simulates the biomass of four microbial functional groups and the biogeochemical cycles of N and O_2 (Chapter 2). In the surface ocean, phytoplankton produce dis- solved organic nitrogen (DON) and sinking organic particles from inorganic N (NH_4^+, NO_2^-, NO_3^-). DON is remineralized by heterotrophic bacteria using O_2, or multistep denitrification (reduction of NO_3^- to NO_2^-, then to N_2) below a critical O_2 threshold (O_2^{crit}). The NH_4^+ and NO_2^-released by heterotrophs is used by autotrophs: slow growing and O_2-inhibited anammox bacteria, or aerobic archaea and bacteria that either perform NH_4^+ or NO_2^-oxidation with nanomolar O_2 sensitivities. Autotrophs assimilate NH_4^+ from seawater for growth. Because the C:N ratio of bacterial biomass (6.8 ± 1.2) (*87*) matches that of organic matter within the ODZ (6.8) (*99*) heterotrophs satisfy their nutrient demand via NH_4^+ remineralized from DON (*86*). DON is released by phytoplankton, sinking particles, and all microbial populations during mortality.

In previous work (Chapter 2), we assessed the model fit to observed long-term mean (climatological) fields of O_2 and NO_3^-, and profile compilations of NH_4^+, NO_2^-, and biologically produced N_2 gas (N_2^{xs}) from within the ETNP. These data reflect the characteristic vertical profiles of key chemical indicators of the metabolic status of the ODZs: subsurface maxima in NO_2^- and N_2^{xs}, reduced accumulations of NO_3^-, and nanomolar levels of NH_4^+ and O_2 (Figure 3.6). To constrain uncertainty in model parameters, we varied microbial growth, mortality, and nutrient affinities over two orders of magnitude, spanning values observed in laboratory cultures and process studies (Table 3.1), and compared the resulting simulated profiles to the observations (Figure 3.6). Of the 90 parameter combinations tested, half reproduce all observed chemical profiles simultaneously, implying a realistic balance of physical and biological fluxes of N and

O_2. This ensemble of model simulations that reproduce the data are used for further analysis and to quantify the sensitivity of our main results.

3.4 Results and Discussion

The simulated rate of regional N loss aligns with geochemical estimates based on measurements of the accumulation of N_2^{xs}, the deficits of NO_3^-, and its isotopes (*68*, *100*), but fluctuates strongly over time (Figure 3.1A) despite the steady rates of ocean circulation. These fluctuations are not caused by changes in the flux of organic matter or the physical supply of O_2 to the ODZ region, which are stable (Figure 3.7). The fluctuations persist across a wide range of physiological and ecological assumptions: regardless of the precise O_2 sensitivities of the microbial populations (yellow, red, and green lines in Figure 3.1A); with and without inclusion of dissimilatory NO_3^- reduction to NH_4^+ (DNRA) (*80*) (blue line in Figure 3.1A); whether heterotrophic denitrification is represented as a facultative or obligate process (*17*, *101*) or if its steps are mediated by a single or multiple populations (*94*) (Figure 3.8). Fluctuations in N loss are found under all ecosystem model parameter combinations that satisfy the available tracer data constraints (Figure 3.9). Their amplitude is large relative to time-mean rates, averaging 43% ± 35% (SD) on regional scales and 233% ± 123% (SD) at the locations where fluctuations occur. While the regionally integrated N-loss rate lacks a characteristic frequency, local rates of N loss can vary through semiregular oscillations (Figure 3.1B). The complex fluctuations in the regional-scale N loss (Figure 3.1A) thus arise from the integration of the many localized oscillators with distinct periods, phasing, and amplitudes.

The oscillations are also evident in aerobic metabolic rates, which together with the changes in N loss, drive large-scale fluctuations in the concentrations of O_2, NH_4^+, and NO_2^-, (Figure 3.2). Fluctuations are strongest at the edge of the ODZ's anoxic core, in a "suboxic" zone, where the full diversity of simulated microbial populations coexist—aerobic NH_4^+ and NO_2^- oxidizers as well as autotrophic anammox bacteria and heterotrophic denitrifiers (Chapter 2). In the anoxic core of the ODZ, where aerobic metabolisms are excluded, the chemical environment, the resident microbial populations, and their metabolic rates are relatively stable over time. The coincidence of variability in zones of long-term nitrifier–denitrifier coexistence implies that the oscillations are driven by interactions between these microbial groups. Indeed, if the nitrifiers are separated from autotrophic anammox and heterotrophic denitrifiers by imposing non-overlapping O_2 thresholds, oscillations do not arise in the model simulations (Figure 3.10).

The mechanism of these oscillations derives from a fundamental ecosystem dynamic: consumption of O_2 by aerobic microbes provides an advantage for anaerobes, but their niche cannot be sustained against the physical O_2 supply without intermittent dominance of the aerobes. In the model ODZ, the consumption of O_2 by NO_2^- oxidation (~41 Tg O_2 y^{-1}) vastly outweighs NH_4^+ oxidation (~4.9 Tg O_2 y^{-1}); NH_4^+ oxidation thus plays little role in the oscillatory dynamic. The complete ecological sequence of the oscillation is illustrated by the phase diagram of NH_4^+ and O_2 at a single point in space (Figure 3.3). When O_2, NH_4^+, and NO_2^- are plentiful, NO_2^- oxidizing bacteria experience net population growth (Figure 3.3A and B, location i). Their metabolic rate exceeds the physical O_2 supply and depletes the available O_2 and NO_2^- (Figure 3.3A and B, ii). The loss of O_2 promotes anaerobic metabolisms, but the loss of NO_2^- also depletes the energy available for heterotrophic growth fueled by denitrification. The NO_2^- oxidizers can short circuit complete heterotrophic denitrification to N_2 because of their higher efficiency of NO_2^- utilization (Chapter 2), which is required by the model to reproduce the observed distribution of NO_2^- within oxic and anoxic waters (Figure 3.11). In contrast, the depletion of NO_2^- has little effect on anammox bacteria because they are generally limited by NH_4^+ in the model, consistent with rate measurements from the ODZs (*17*, *51*). Thus, as NO_2^- is drawn down by oxidation, the decline of heterotrophic denitrification relative to anammox (Figure 3.3C, iii) depletes NH_4^+ to levels that, in − turn, limit the NO_2^- oxidizers, which utilize NH_4^+ for biomass production, slowing their rate of O_2 and NO_2^- utilization (Figure 3.3B, iii). The cessation of O_2 consumption allows its concentration to be gradually replenished by the physical supply, while NO_2^- simultaneously accumulates due to an excess of NO_3^- reduction over NO_2^- oxidation (Figure 3.3A, iv). O_2 accumulation selects against anammox (Figure 3.3C, iv), while NO_2^- accumulation fuels a rapid burst of N loss through heterotrophic denitrification (Figure 3.3D, i). The NH_4^+ liberated from DON during this denitrification pulse restores it to levels that sustain NO_2^- oxidizer growth, a condition that again favors net O_2 consumption, and the oscillation starts anew.

The ecosystem oscillations predicted here arise in a completely steady physical environment, but the supply of organic matter and O_2 to the ODZ exhibit strong temporal variations in the real ocean. We tested the impact of physical variability on the intrinsic ecosystem oscillations by first imposing empirically derived seasonal fluxes of organic particles and then stochastic changes in the rates of ocean circulation (Figure 3.12). Ecosystem-driven variability persists, and is even amplified, in the presence of these external forcings, suggesting the oscillations would act as a strong source of variability in the natural environment.

Top-down ecological controls on microbial populations also have the potential to limit fluctuations caused by resource competition. We represented grazing losses in the model by applying a quadratic mortality term to all microbial populations, assuming predation is unselective (Figure 3.13). We varied the intrinsic grazing rate by an order of magnitude and find that while the variance in regional N loss is unchanged under weak grazing, under strong grazing the variance is decreased by an order of magnitude (Figure 3.13A). However, adding this strong grazing term causes an unrealistic build up of NH_4^+ concentration in the anoxic core of the ODZ (Figure 3.13B). By reducing the biomass of the slow- growing anammox bacteria, grazing lessens the main sink of NH_4^+ in these zones, allowing it to accumulate to persistently high concentrations. The observed distribution of NH_4^+ therefore does not support the grazing rates needed to stabilize the ecosystem oscillations.

The distribution of NH_4^+ within the ODZ provides a unique and detectable geochemical signature of the microbial oscillations (Figure 3.4). Over the course of the oscillation, shifts in the balance of NH_4^+ sources and sinks lead to its temporary accumulation within the ODZ, at levels up to ~10 times the mea- surable detection limit of the most sensitive technique (~10–15 nM)—the orthophthalaldehyde (OPA) method. These NH_4^+ spikes are short lived, however, occurring only ~5% of the time throughout the ODZ ($O_2 < 5$ μM), such that the average model concentration of NH_4^+ remains below detection. We looked for this potential signature of the oscillation by analyzing 18 depth profiles of NH_4^+ from the ETNP measured using the OPA method (section 3.6 supplemental methods). Consistent with the predicted time-mean NH_4^+ concentrations, the average observed concentration of NH_4^+ in waters with $O_2 < 5$ μM falls below detection. However, in ~8% of these measurements, we find NH_4^+ concentrations exceeding this detection limit, consistent with the frequency of occurrence predicted by ecological oscillations. NH_4^+ measurements made with less sensitive conventional techniques suggest spikes are also present in the eastern tropical South Pacific and Arabian Sea ODZs outside the model domain (e.g., refs. *65*, *102*, *103*), but a quantitative analysis of these features will require more high precision data.

A transient accumulation of NH_4^+ within the ODZ might also be expected from excretion at depth by vertically migrating zooplankton and micronekton (*81*, *104*). Measured NH_4^+ spikes occur up to 100–300 m below the mean depth of diel vertical migration recorded for this region (line and shading in Figure 3.4). In contrast, elevated NH_4^+ within the ODZ is found over a similar depth range to where ecological oscillations occur in the model. Temporary spikes of NH_4^+ could also arise from transitory pulses of sinking organic matter that release NH_4^+ into the ODZ faster than it can be consumed. We tested whether changes in the particle flux can produce NH_4^+ spikes, by adding the observed seasonal cycle in net primary production to a model simulation with weak internal oscillations, and thus inherently small pulses of NH_4^+. In this case, even with forced fluctuations in the supply of organic matter into the ODZ, the predicted time-varying concentrations of NH_4^+ barely exceed the detection limit at any depth. The measured spikes in NH_4^+ therefore support strong nonequilibrium ecosystem behavior.

Ecological oscillations within the ODZ have direct consequences for the fraction of total N loss that derives from anammox ($f$amx) as opposed to heterotrophic denitrification (Figure 3.5). The contribution of these metabolic pathways to N loss has been observed to vary across and within the ODZs from direct rate measurements in the field, but the causes of these variations remain hotly debated (*54*, *81*, *99*). During the course of the oscillation, when NO_2^- oxidizing bacteria are ascendant, the NO_2^- that would otherwise be reduced by heterotrophs is reoxidized to NO_3^-. The suppression of heterotrophic denitrification temporarily allows NH_4^+-limited anammox to contribute up to 100% of local N_2 production. However, after NO_2^- accumulates, the rapid bursts of heterotrophic denitrification vastly exceed previous rates of anammox (Figure 3.3 C and D) and thereby dominate total N loss over a complete oscillatory cycle (horizontal lines

Fig. 5). These local variations in the balance of N loss processes can temporarily obscure the time-mean gradients in $f$amx across the ODZ (Chapter 2). Because they occur over an extremely narrow range in the concentrations of O_2, NH_4^+, and NO_2^-, evaluating this ecological contribution to observed variations in $f$amx will require frequent and high-precision measurements of these chemical abundances and associated metabolic rates.

Oscillatory behavior is a common feature of idealized ecosystem models with multiple interacting populations (*105*, *106*), but is rarely shown to persist in realistic representations of the environment such as a three-dimensional ocean circulation. Intrinsic ecosystem oscillations provide a mechanism to generate variations in marine microbial community structure and N and O_2 cycling, which are often ascribed to externally forced changes in physical and chemical conditions. Because these oscillations lack spatial coherence and power at decadal and longer timescales (Figure 3.1A), they are unlikely to explain large-scale decadal variations in N loss (*37*). However, dynamics such as these may be pervasive beyond the ODZs, occurring wherever the physical supply of resources selects for a microbial community that over time undermines its own ecological niche by shifting the chemical environment to temporarily favor the growth of its competitors or degrade the growth of its facilitators.

3.5 Acknowledgements

We thank Tim DeVries for supplying the ocean circulation model, H. Frenzel for technical assistance, and C. Fuchsman and A. Santoro for insightful discussions. This work was made possible by grants from the Gordon and Betty Moore Foundation (GBMF 3775 to C.D.) and the Joint Institute for the Study of the Atmosphere and Ocean under NOAA Cooperative Agreement (NA15OAR4320063, contribution no. 2018-0141, to B.X.C.). This work is NOAA-Pacific Marine Environmental Laboratory contribution no. 4772.

3.6 Supplemental Methods

Samples from the eastern tropical North Pacific (ETNP) were collected by B.X. Chang in April 2012 during a cruise aboard the R/V Thomas G. Thompson between 14 and 23°N and 103 and 112°W using a Seabird 911 CTD (conductivity, temperature, depth) equipped with a Seabird SBE 43 dissolved oxygen sensor, a WETLabs ECO Chlorophyll fluorometer, and a Biospherical/Licor photosynthetically active radiation (PAR)/irradiance sensor attached to a rosette of 24-10L Niskin bottles (*107*). Vertical profiles of ammonium concentrations were measured using the ortho-phthaldialdehyde (OPA) method (*108*) (detection limit, ~10 - 15 nM) at 18 stations. OPA ammonium samples were collected directly from the Niskin bottles into HDPE bottles that were pre-conditioned with the OPA reagent. Samples were stored at 4°C and ammonium concentrations were measured within 24 hours of sample collection.

3.7 Figures

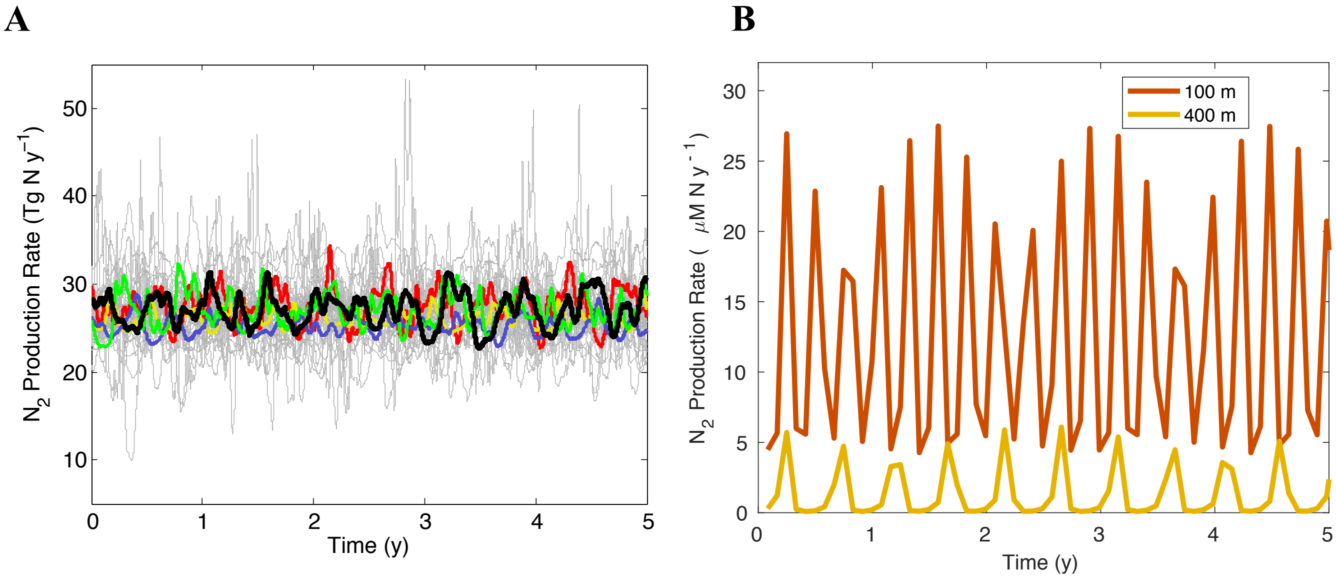

Figure 3.1. Time-series of ecologically-driven variability in the regional and local rates of N loss from the ODZ of the eastern tropical North Pacific. (*A*) Rates are spatially integrated across the ETNP in the standard model simulation (black), and sensitivity cases (grey and colors). Oscillations occur regardless of physiological or ecological uncertainties (Table 3.1): whether O_2 tolerances of anaerobes are 1 μM (yellow) or ≥10 μM (red), if the two steps of nitrification (NH_4^+ and NO_2^- oxidation) have different nanomolar O_2 sensitivities (green), or if an additional metabolism (dissimilatory nitrate reduction to ammonium; DNRA) is incorporated into the model (blue). They also hold across wide ranges in other microbial ecosystem parameters (grey; Table 3.1). (*B*) Time-series of local rates of N loss in locations with representative ecosystem oscillations (12°N, 90°W at 100 m and 25°N, 113°W at 400 m).

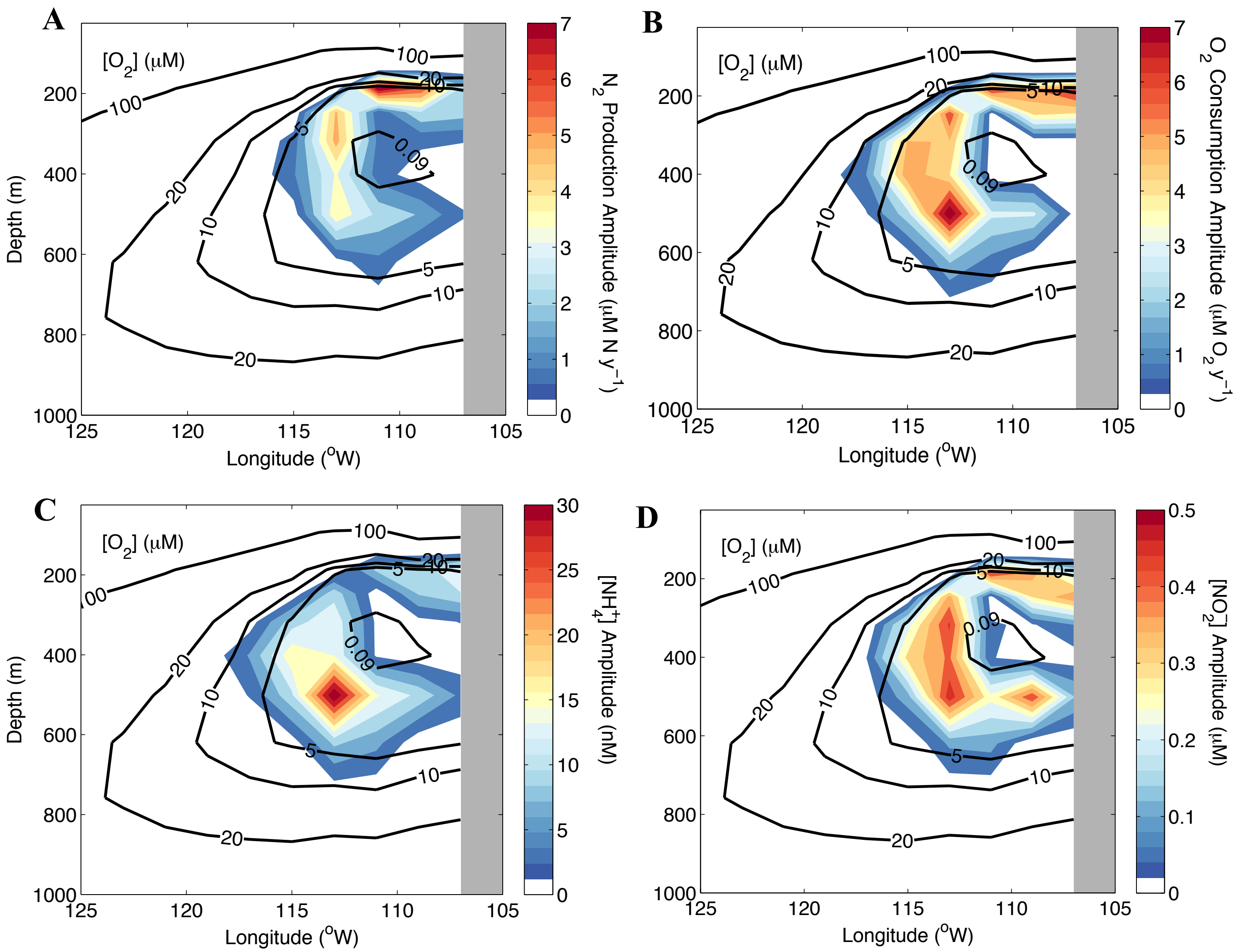

Figure 3.2. Spatial distribution of ecologically-driven oscillations within the O$_2$ deficient zone. The spatial distribution of oscillation amplitudes (colors) is shown along a zonal cross-section through the model ODZ (20 − 28°N). Oscillation amplitudes are computed as the difference between maximum and minimum values over a 10-year simulation for (*A*) the N loss rate, (*B*) the O$_2$ consumption rate, and the concentrations of (*C*) NH$_4^+$, and (*D*) NO$_2^-$. Variability is overlain by time-mean concentrations of O$_2$ (in μM; black contours). Grey shading denotes the western coastline of North America.

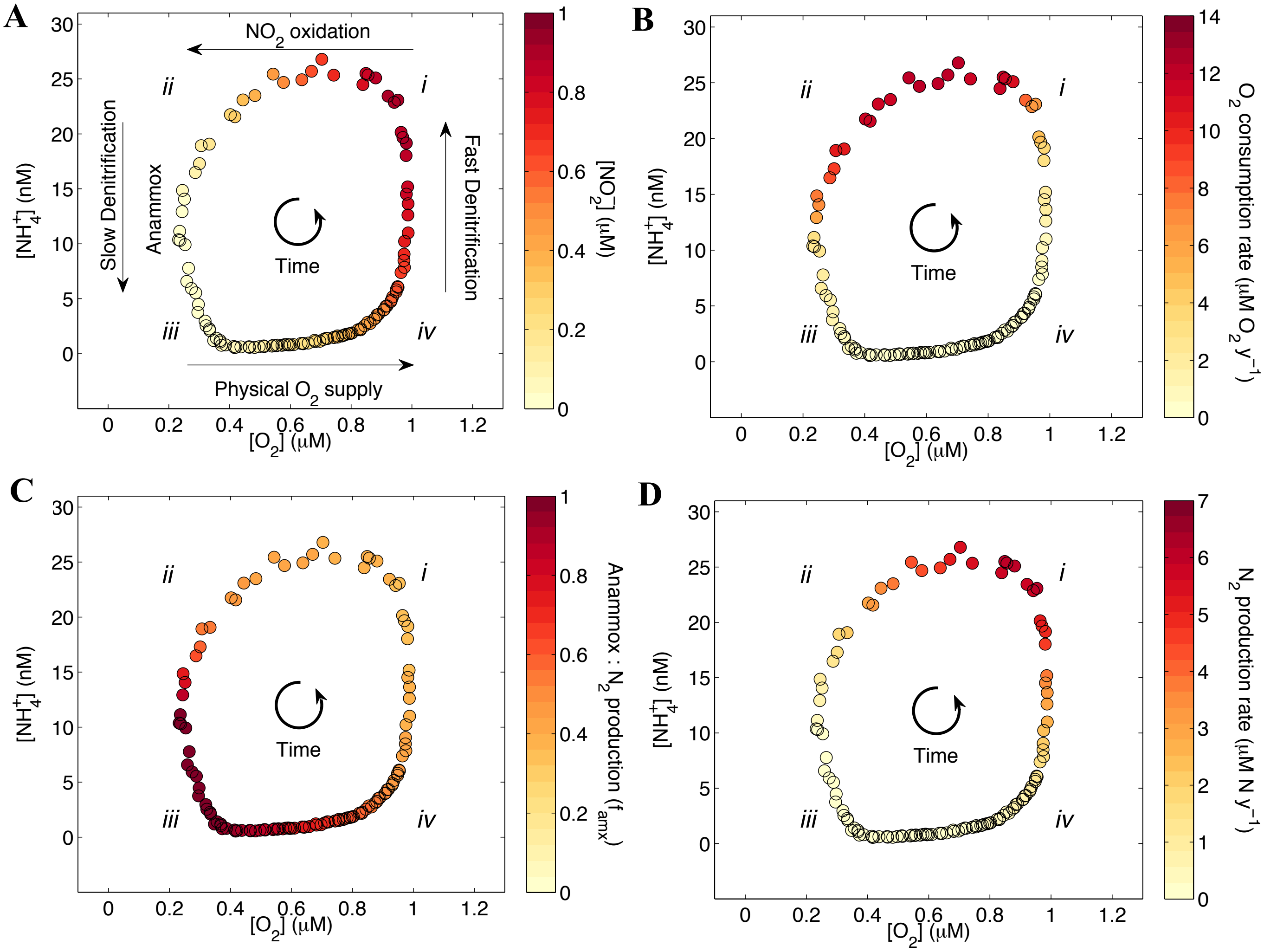

Figure 3.3. Dynamics of the ecosystem oscillation. The oscillation of key ecosystem variables is shown in the phase space of NH_4^+ and O_2, from a representative location at the suboxic boundary between the anoxic zone and the oxic ocean (i.e. same as in Figure 3.1B at 400 m). Time proceeds in the counter-clockwise direction, indicated by spiraling arrows. NH_4^+ and O_2 levels are colored by (*A*) the concentration of NO_2^- (μM), (*B*) the rate of O_2 consumption by NO_2^- oxidation (μM O_2 y^{-1}), (*C*) the contribution of anammox to total N_2 production (*f*amx), and (*D*) the rate of total N_2 production (μM N y^{-1}). Straight arrows in (*A*) identify the dominant process driving changes in NH_4^+ and O_2 during each phase of the cycle. Locations *i*-*iv* marked on the phase diagrams are described in the text.

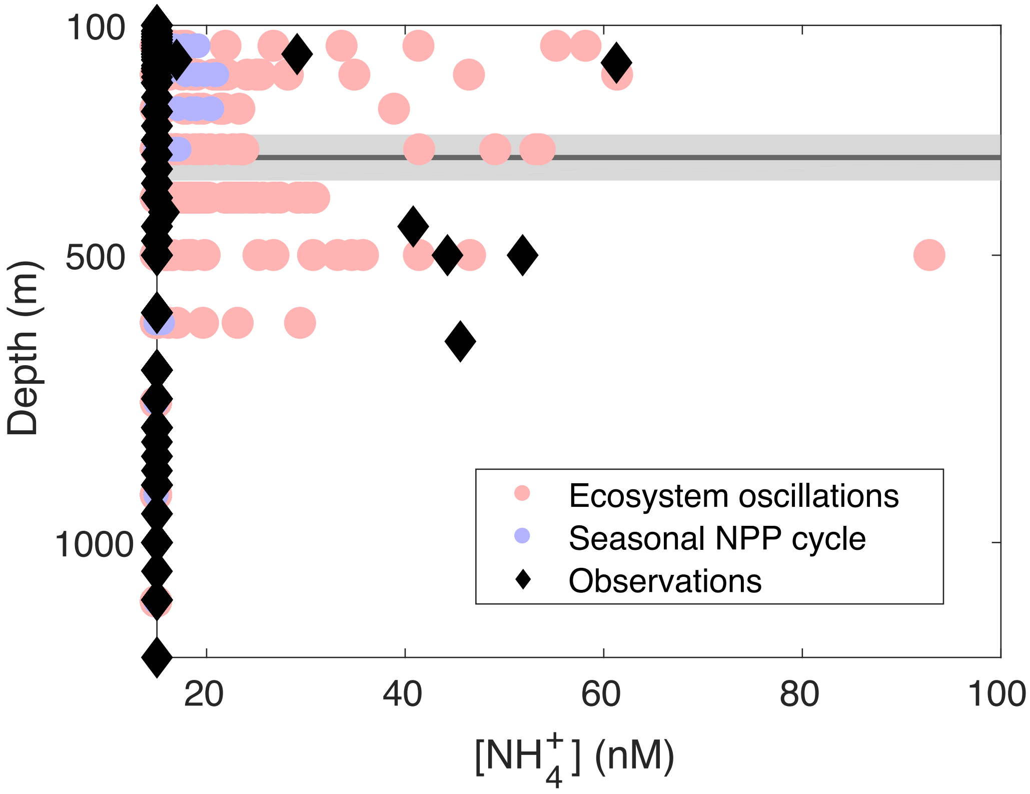

Figure 3.4. NH$_4^+$ depth profiles from the oxygen deficient zone of the eastern tropical North Pacific, in model simulations and observations. Depth profiles were sampled monthly over the course of a year in the standard model simulation (pink circles), and measured on a cruise to the ETNP in 2012 (black diamonds; SOM). NH$_4^+$ exceeds the detection limit (~15 nM) in ~5% of the time in the model simulation and in ~7% of observations at O$_2$ < 5 µM, but on average is below detection in both. Model and observed NH$_4^+$ values below 15 nM are set to this detection limit. The diel vertical migration depth for the ETNP is plotted (mean indicated by line, SD by shading) (81). The time-dependent NH$_4^+$ profiles are also shown from a model simulation with an imposed seasonal cycle of primary production, but weak internal oscillations (violet). Seasonal fluctuations in the supply of organic matter to the ODZ cannot produce the magnitude of NH$_4^+$ spikes implied by the observations.

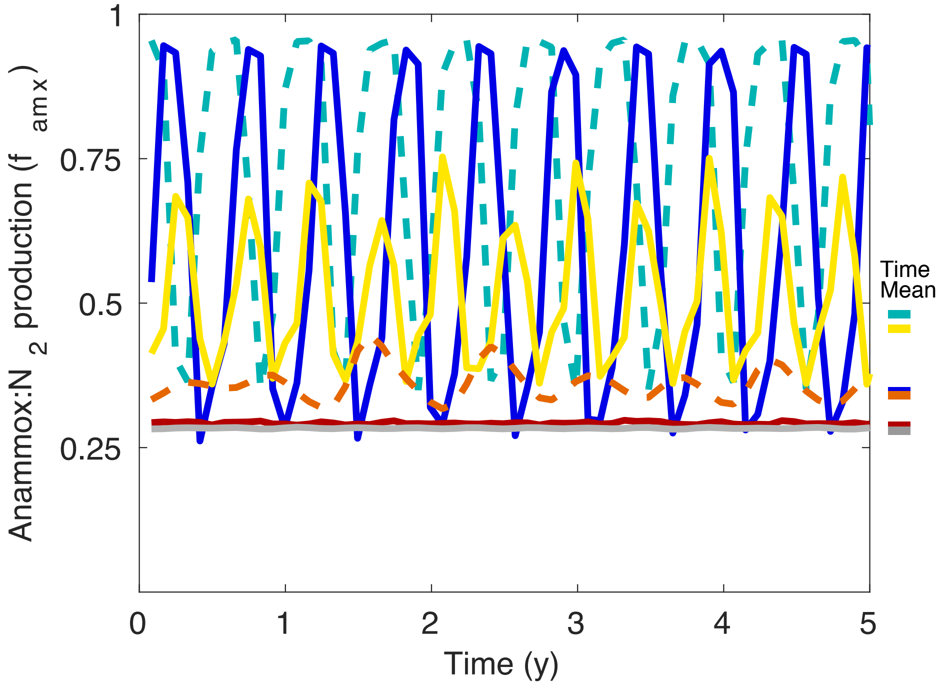

Figure 3.5. The contribution of anammox to total N_2 production (*f*amx) over time. Time-series of f_{amx} in representative locations across the ODZ, from 115 m – 450 m. At the oxic-anoxic interface (oxycline), f_{amx} can vary over wide ranges that temporarily obscure its time-mean gradient (blue, cyan, and yellow lines). Within the secondary NO_2^- maximum, f_{amx} approaches the value of 0.28 and oscillations are weak (orange, red, and grey lines). Solid lines are from the heart of the ODZ, whereas dashed lines are from its margins. Time-mean contributions of anammox to N loss are shown as colored horizontal lines on the right axis.

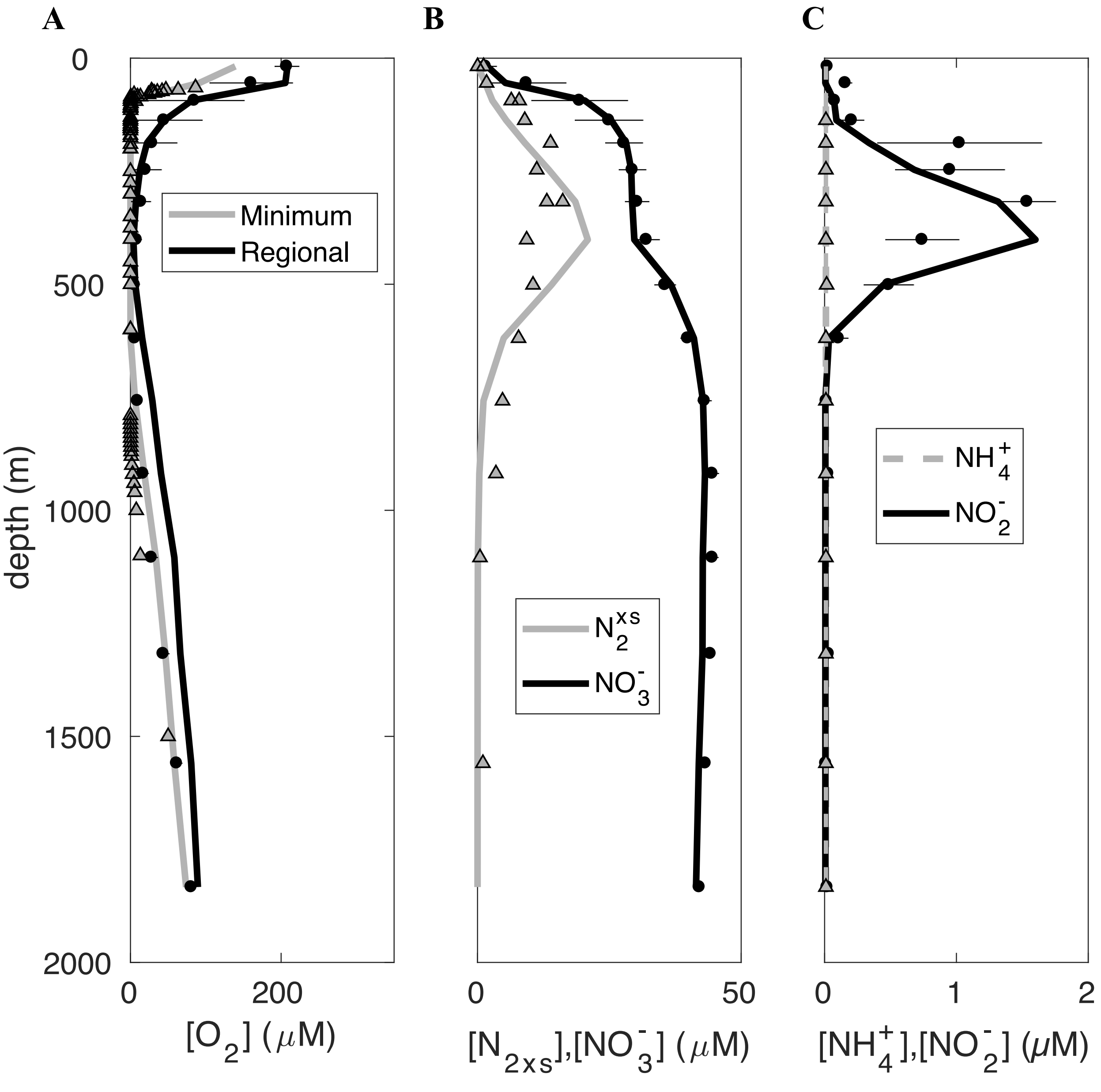

Figure 3.6. Depth profiles of O_2 and N-bearing compounds from the O_2 deficient zone of the eastern tropical North Pacific. Model values (lines) are compared to observations (symbols). An example model parameter set that reproduces the observations is shown (i.e. standard value column in Table 3.1). Model parameters that do not reproduce the observed ODZ profiles are discarded from further analysis as in Chapter 2. O_2 in the core of the model ODZ is taken as the minimum value at each depth level. Observed depth profiles of O_2 from the ODZ core are from published measurements using the high-precision STOX sensor (*66*). Regional O_2, as well as NO_3^-, are averaged across the ODZ both in the model and climatologies (*4, 185*). Model depth profiles of NH_4^+, NO_2^-, N_2^{xs} are averaged around the regions within the ODZ where observations were made (Chapter 2). Error bars are spatial standard deviations for tracers with climatological observations (i.e., O_2 and NO_3^-) and standard errors for profile compilations (i.e., NH_4^+, NO_2^-). Units of N_2xs are μM N-N_{2xs}.

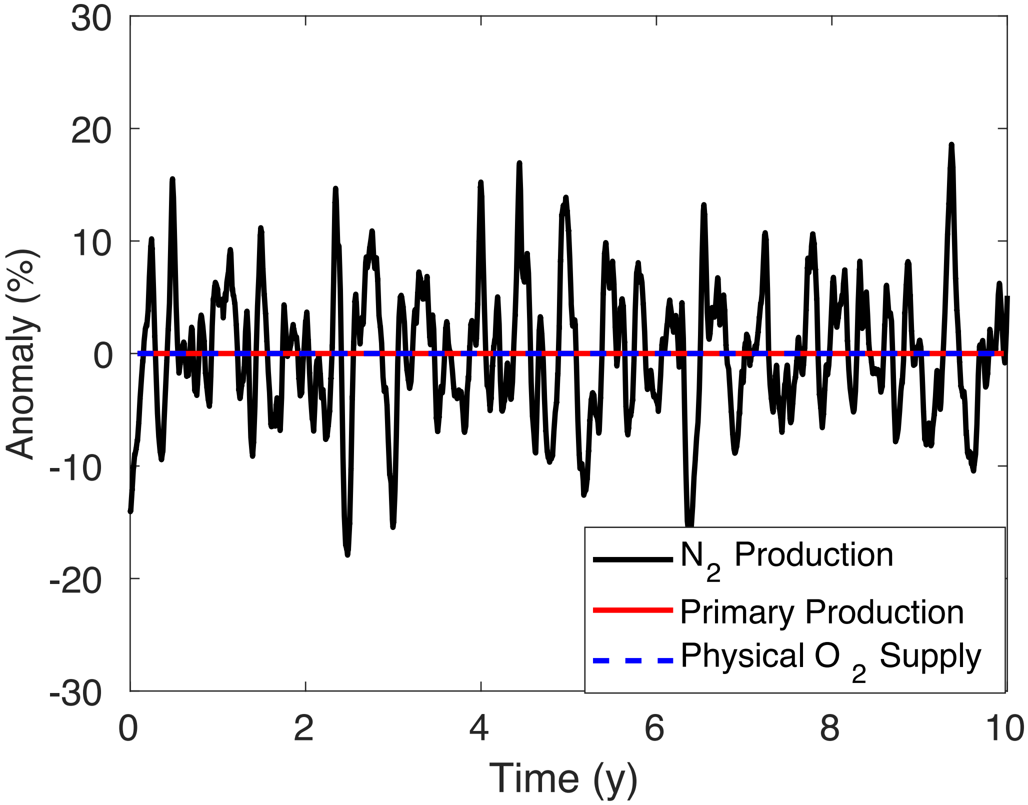

Figure 3.7. Time-series of relative changes in the regional rate of nitrogen loss, primary production, and physical oxygen supply to the O_2 deficient zone of the eastern tropical North Pacific. Anomalies are computed as percent changes relative to the time-mean. The regional rate of nitrogen loss displays strong temporal fluctuations despite the constant rates of physical O_2 and organic matter supply.

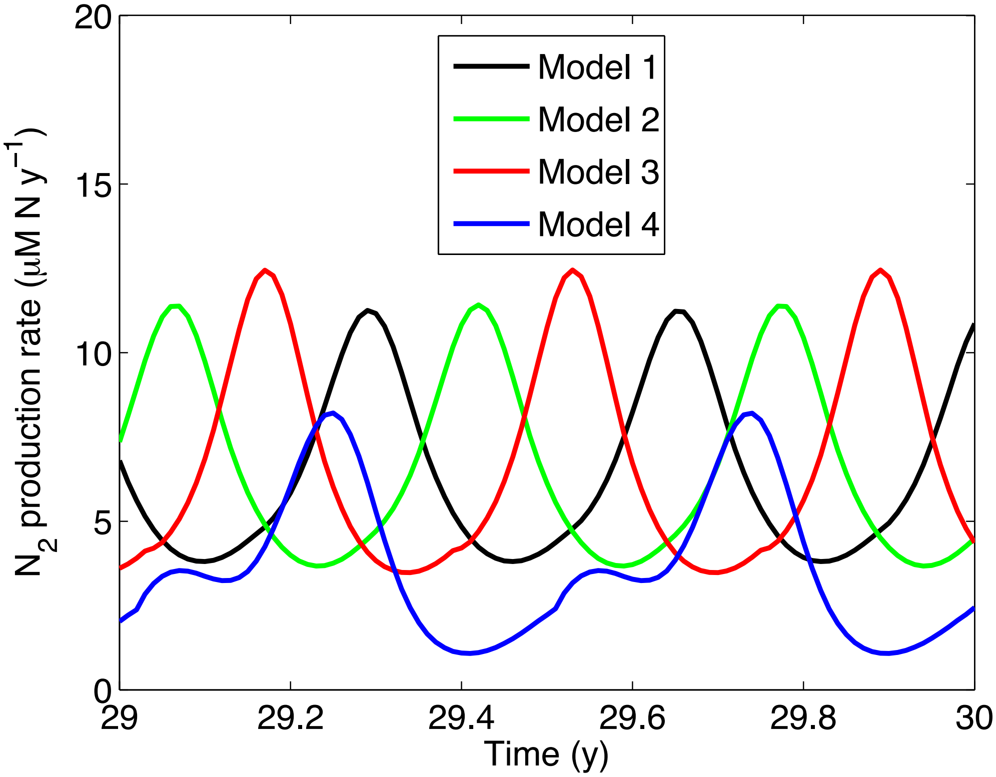

Figure 3.8. Sensitivity of the ecosystem oscillation to different parametrizations of heterotrophic bacteria physiology and ecology. To allow for rapid model solutions, each of these experiments was conducted in a one-box model of the ODZ. Model 1 uses the standard ecosystem model parameter set and parametrizations (Table 3.1; Chapter 2). Model 2 tests the effect of inhibition kinetics as opposed to a critical O_2 switch for heterotrophic denitrification. The measured nM O_2 inhibition parameters from ref. (64) are used for heterotrophic and anammox bacteria (Table 3.1), lowering the minimum values of the anaerobic O_2 sensitivities tested in this work. Model 3 tests the effect of assuming the heterotrophs are comprised of two populations. The first performs aerobic respiration, with a nanomolar half-saturation constant (12) (K_m = 20 nM O_2). The second is an obligate denitrifier. Model 4 tests the effect of splitting the heterotrophic denitrifiers into multiple populations. The first is a facultative aerobe that switches to NO_3^- reducer below a critical O_2 threshold, whereas the second can only conduct NO_2^- reduction to N_2^{xs} below a critical O_2 threshold (94). In all model scenarios, intrinsic fluctuations arise in the simulated rate of N loss despite the steady rates of O_2 and organic matter supply. The box model circulation is a constant, 1-way advective flow that brings in tracers from the boundary and removes them from within the box at a rate of 1 y^{-1}. Boundary conditions are chosen to reflect tracer concentrations found at the boundary of the simulated ODZ within the GCM. Model simulations are integrated for 30 years and display long-term mean tracer concentrations that fall within the range measured for the ETNP. All ecosystem parameters and model structures are the same as in the GCM, except where explicitly noted above.

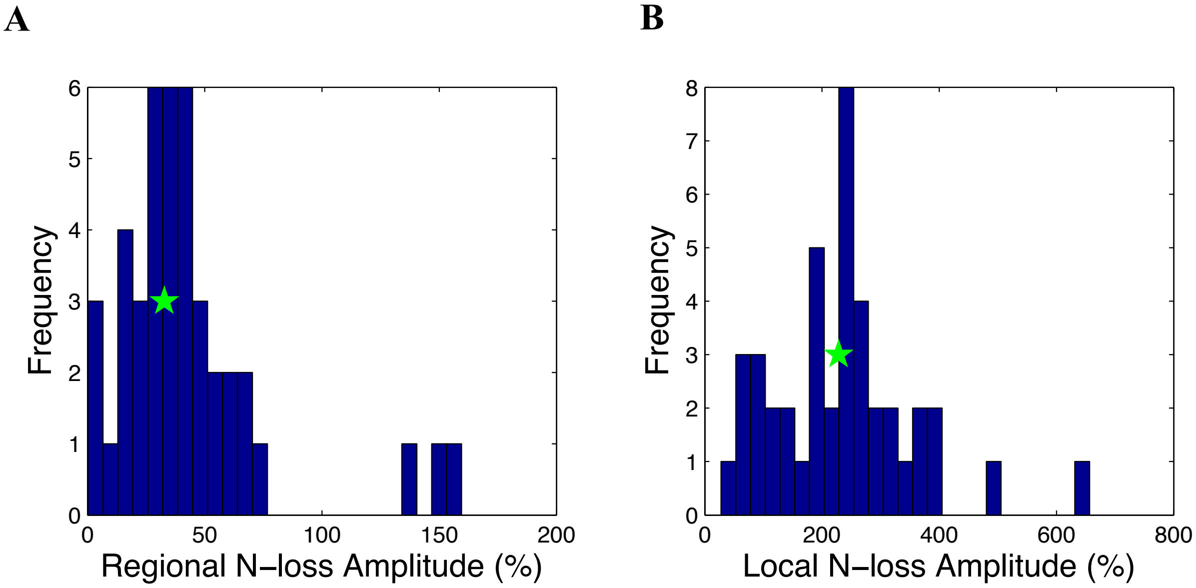

Figure 3.9. Amplitude of (*A*) regional and (*B*) local fluctuations in rates of N loss across data-reproducing sensitivity experiments in the GCM. Amplitudes are computed as the maximum minus minimum rates over the simulation time-course, and are normalized as percentages of the time-mean rate. Local amplitudes are averaged across grid cells with potentially measurable N loss fluctuations and time-mean rates (N loss ≥ 0.1 nM N d^{-1}; *70*). The green star marks the values from the standard model parameter set. We find that ecosystem oscillations emerge in every scenario that reproduces observations, indicating they are a realistic and robust feature of the microbial ecosystem model.

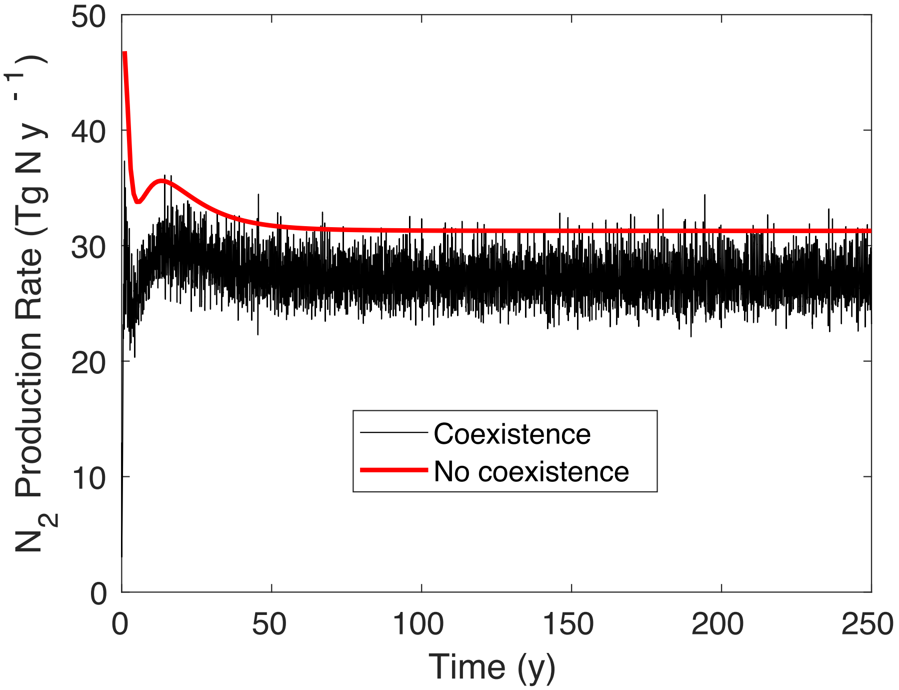

Figure 3.10. The effect of nitrifier-denitrifier niche-separation on the intrinsic ecosystem fluctuations in N loss. Time-series of the regional rate of N loss in the standard microbial ecosystem model simulation (black) and in a geochemical model (red) in which the coexistence of aerobic nitrifying and anaerobic denitrifying populations is precluded via non-overlapping O_2 thresholds (Chapter 2). In the geochemical model, the switch from aerobic to anaerobic processes occurs across a prescribed critical oxygen threshold (O_2^{crit}). Above O_2^{crit}, organic matter remineralization occurs via aerobic heterotrophy and complete nitrification. Below O_2^{crit}, organic matter remineralization occurs through heterotrophic denitrification and anammox in the ratio of ~72:28. In the geochemical model, the predicted rate of N loss is completely stable, confirming the oscillations in the ecosystem model arise from interactions between aerobic and anaerobic populations.

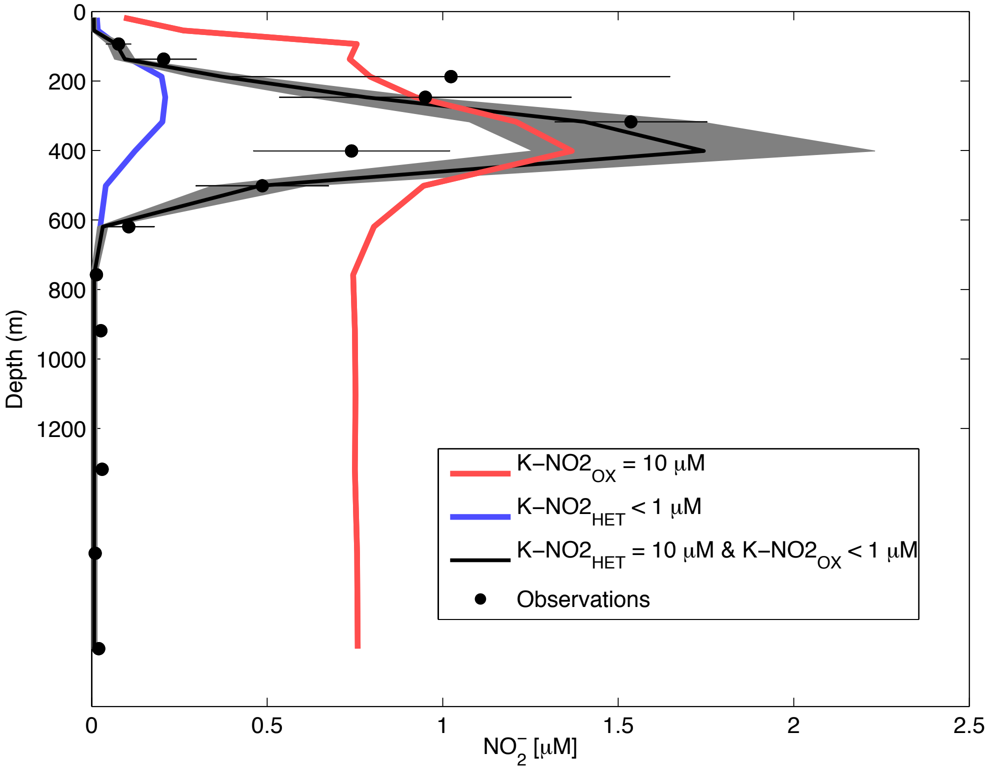

Figure 3.11. The regional mean profile of the secondary NO_2^- maximum in the ETNP (Chapter 2) compared to model simulations with different values of the half-saturation constant for NO_2^- (K_m-NO_2^-) for heterotrophs versus NO_2^- oxidizers. The K_m-NO_2 value of denitrifying heterotrophs has been previously estimated in laboratory uptake experiments (K_m-NO_2 = 8 ± 4.2 μM) (*94*). We find that a similar range of values (K_m-NO_2 = 5 - 20 μM) is able to reproduce the available field measurements of NO_2^- within the anoxic core (black line; 23). If the K_m-NO_2 of heterotrophs is chosen to be too low (≤ 1 μM), heterotrophs deplete NO_2^- below observed values in the anoxic core. In this case, not even maximum model NO_2^- levels (blue line) are large enough to match mean observations (dots). Conversely, if this parameter is too high, NO_2^- accumulates to unrealistically large values. We are unaware of any laboratory study that estimates realistic K_m-NO_2 values for marine NO_2^- oxidizing bacteria. Instead, this parameter value is inferred by comparing model simulations to in situ NO_2^- measurements in the oxic ocean, where NO_2^- oxidation is the dominant sink for NO_2^-. Solutions with sub-micromolar K_m-NO_2 (black line) best reproduce the available measurements. If, like for heterotrophs, the K_m-NO_2 of NO_2^- oxidizers is in the micromolar range, NO_2^- concentrations accumulate to higher values than observed in the oxic ocean (red line). Finally we note that although the K_m-NO_2 of anammox cannot be inferred from the observed NO_2^- distribution (Table 2.1), strong ecosystem oscillations occur across the range of sensitivities implied by kinetics experiments from marine sediments (K_m-NO_2 = 0.1 – 3 μM) (89).

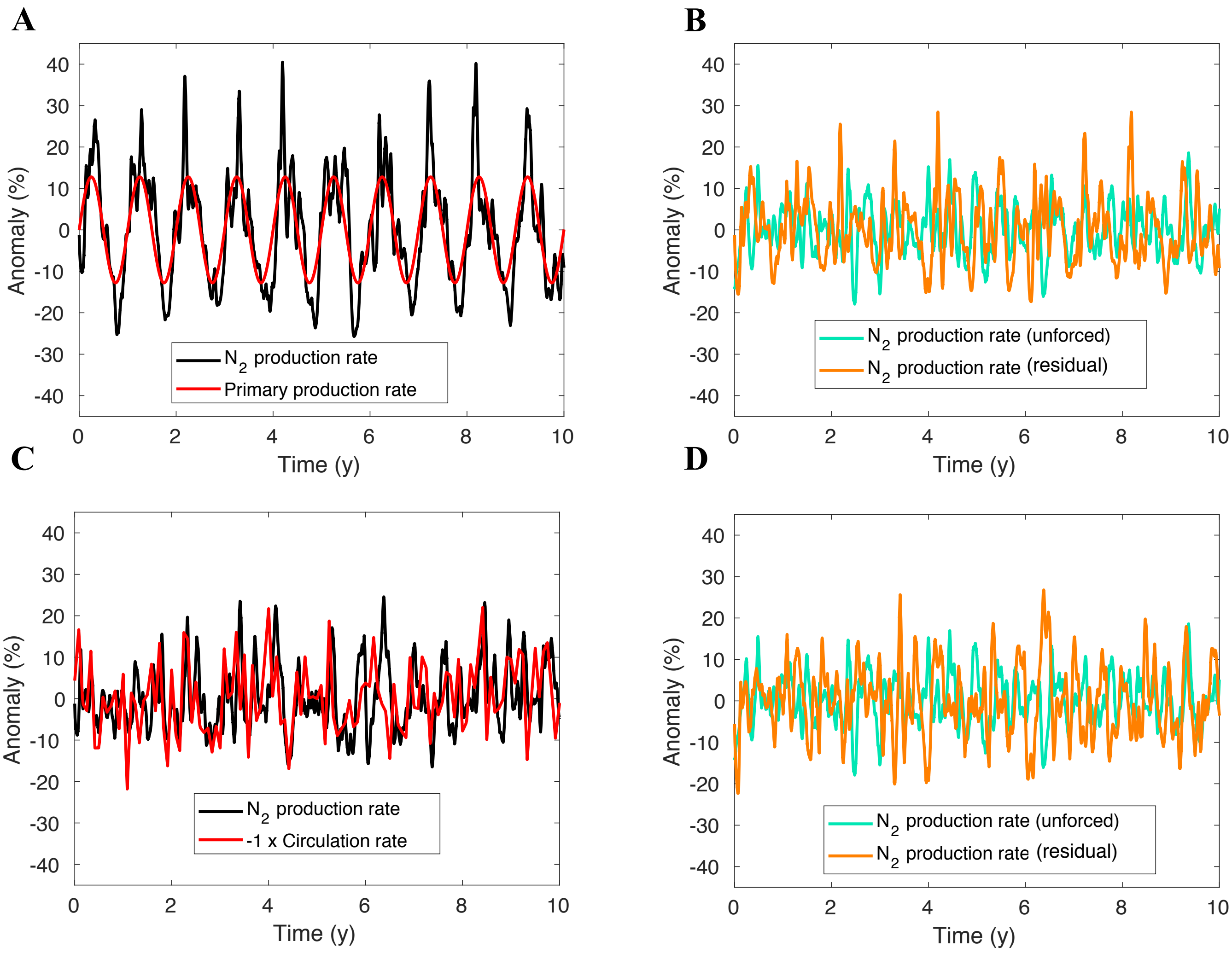

Fig. 3.12. Time-series of variability in the regional rate of N loss in response to external forcing. We conducted two sets of sensitivity experiments to test the impact of external variability on the intrinsic ecosystem oscillations. First, we imposed a seasonal cycle in net primary production (NPP) (*A*, *B*). Second, we added stochastic variations in the rates of ocean circulation (*C*, *D*). (*A*) Percent changes in the regional N loss rate from the ETNP (black) under the case of an imposed seasonal cycle of NPP (red). The amplitude the imposed seasonal cycle (12.8% of the mean) is based on satellite-derived NPP (187) within the model domain, using observations from 2002 to 2010 (http://orca.science.oregonstate.edu/1080.by.2160.monthly.hdf.vgpm.s.chl.a.sst.php). The seasonal cycle explains ~ 59% of the simulated changes in the rate of N loss ($R^2 = 0.59$, $p < 0.01$). At the locations within the ODZ where the strongest ecosystem oscillations occur (amplitude > 5 μM N y^{-1}), the forced seasonal variations in total NPP account for ~33% of the total variance in N removal, implying an even stronger role for the oscillations locally. (*B*) Ecosystem contribution to variability in the regional rate of N_2 production in the unforced simulation (green) and in the case of imposed seasonal changes in NPP (orange). Changes are attributed to the ecosystem dynamics by subtracting out the seasonal component of N_2 production variability, assuming this varies with the same relative amplitude and timing as the forcing itself. Components are shown as percent anomalies relative to the time-mean rate of N_2 production. Variability resulting from the ecosystem dynamics remains undiminished and is even amplified under the seasonally varying particle flux scenario. (*C*) Percent changes in the regional N loss rates from the ETNP (black) under the case of stochastic monthly variations in the regional rates of ocean circulation (red). The time-dependent ocean circulation rate (A) is varied by scaling the annual mean rate (A_0) by a forcing factor (F) according to: $A = A_0 (1+F)$. The forcing factor is interpolated from monthly values that are randomly sampled from a normal distribution with a mean of 0 and standard deviation of 0.1. The time-series of circulation rate changes explain < 20% of the simulated variations in N loss ($R^2 = 0.17$, $p < 0.01$). (*D*) Ecosystem contribution to variability in the regional rate of N_2 production in the unforced simulation (green) and in the case of stochastic changes in ocean circulation (orange). Changes are attributed to the ecosystem dynamics as in (*B*). Because the relationship between the ocean circulation changes and the rate of N_2 production is negative ($r = -0.41$), we multiply the forcing by -1 before removing it from the simulated N_2 production rate. Variability resulting from the ecosystem dynamics remains undiminished under the stochastically varying ocean circulation scenario.

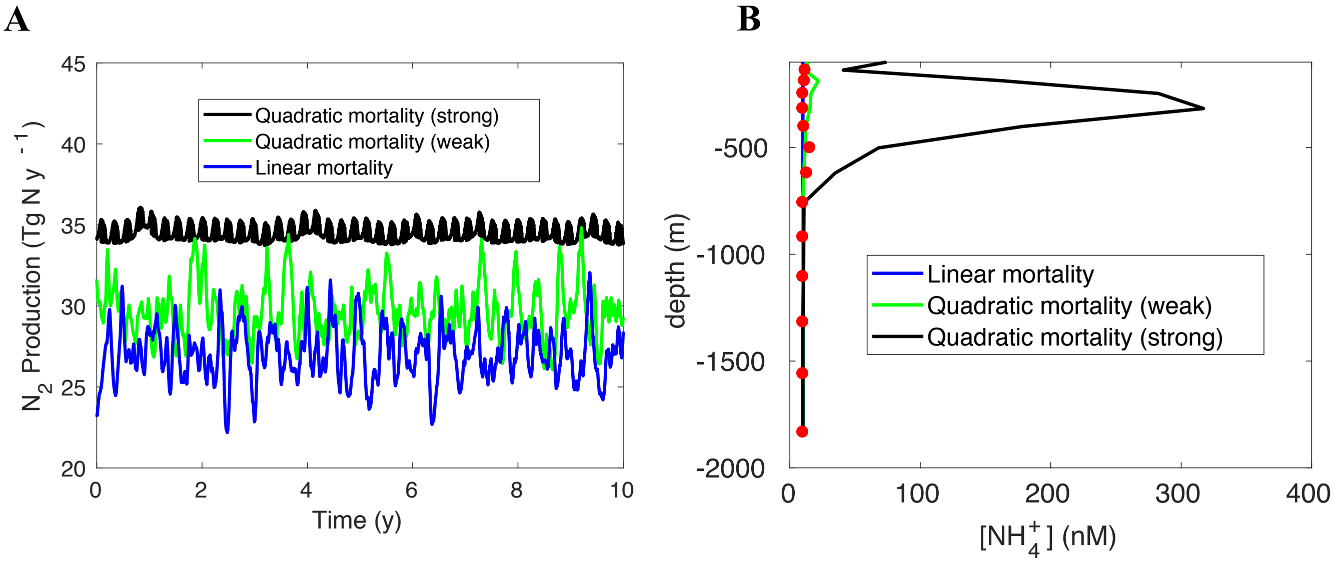

Figure 3.13. The impact of grazing on the microbial ecosystem fluctuations and time-mean distribution of NH_4^+. We tested the impact of grazing on the microbial ecosystem dynamics by applying a quadratic mortality term (M, in μM N d^{-1}) to the microbial biomass growth equations (Chapter 2) according to: $M = m_2 \cdot B \cdot B_{tot}$ (e.g., *137*). Here m_2 is the intrinsic predation rate constant (in units of μM N^{-1} d^{-1}), B is the biomass (μM N) of the heterotrophs, anammox, NH_4^+ oxidizers or NO_2^- oxidizers, and B_{tot} is their combined biomass (μM N). This form of mortality can be thought of as representing predation from a non-selective grazing community whose biomass scales with that of the total prey population (B_{tot}) on which they feed. (*A*) Time-series of the regional rate of N loss in the standard model simulation, which assumes linear mortality (blue; Table 3.1; Chapter 2), and in cases with an additional strong (m_2 = 10 μM N^{-1} d^{-1}; black) and weak (m_2 = 1 μM N^{-1} d^{-1}; green) quadratic mortality term. (*B*) Time-mean NH_4^+ depth profiles within the ODZ in each model scenario (lines) and in observations (red circles). In the case of strong predation, NH_4^+ persistently accumulates to unrealistically high levels.

3.8 Tables

Table 3.1 Microbial ecosystem model parameter sensitivity tests in addition to those documented in Table 2.1.

Parameter	**Symbol**	**Units**	**Standard Value**	**Prior Range**	**Posterior Range**	**References**
O_2 half-saturation	K_{O2}	nM	20 AO 20 NOB	20 – 333 20 – 778	20 - 333 20 - 778	AO, NOB: (10-13)
Critical O_2 threshold for heterotrophic denitrification	O_2^{crit}	µM	5 (255 nM – 5 µM in box model)	1 - 10	1 – 10	(10, 11, 14-19)
50 % O_2 inhibition of anammox	K_{O2}^{inh}	µM	8.1 (886 nM – 8.1 µM in box model)	1 - 15	1 – 15	(10, 14, 15)
Fraction of heterotrophic NO_2^- uptake to DNRA	σ^{DNRA}	unitless	0 (0.5 in DNRA sensitivity test)			(14)

Model equations are detailed in section 2.7. Abbreviations H, AX, AO, and NOB stand for heterotrophic bacteria, anammox bacteria, ammonium oxidizing archaea and bacteria, and nitrite oxidizing bacteria, respectively. Standard value column refers to the base case model parameter set. The prior range column provides the range of model parameters that were tested against geochemical data from the ODZ (Figure 3.6). The posterior range column provides the parameter values that reproduce this data and were used for further analysis (e.g. Figure 3.1). Where no range is given, only the standard value reproduces the data. In the sensitivity test that includes dissimilatory nitrite reduction to ammonium (DNRA) as a heterotrophic growth pathway, DNRA converts NO_2^- to NH_4^+ and remineralizes DON to NH_4^+. We use the same the kinetic parameter values for DNRA as for heterotrophic denitrification. Parameters not listed here are the same as in Table 2.1.

Chapter 4

Temperature-dependent hypoxia explains biogeography and severity of end-Permian marine mass extinction

4.1 Abstract[3]

Rapid climate change at the end of the Permian Period (~252 million years ago) is the hypothesized trigger for the largest mass extinction in Earth's history. We present model simulations of the Permian/Triassic climate transition that reproduce the ocean warming and oxygen (O_2) loss indicated by the geologic record. The effect of these changes on animal survival is evaluated using the Metabolic Index (Φ), a measure of scope for aerobic activity governed by organismal traits sampled in diverse modern species. Modeled loss of aerobic habitat predicts lower extinction intensity in the tropics, a pattern confirmed with a spatially explicit analysis of the marine fossil record. The combined physiological stresses of ocean warming and O_2 loss can account for more than half the magnitude of the "Great Dying."

---

[3] An edited version of this chapter was published as Penn, J.L., Deutsch, C., Payne, J.L., and Sperling, E.K. (2018), Temperature-dependent hypoxia explains biogeography and severity of end-Permian marine mass extinction, *Science*, 362 (6419), eaat1327. DOI: 10.1126/science.aat1327

4.2 Introduction

Volcanic greenhouse gas release is widely hypothesized to have been the geological trigger for the largest mass extinction event in Earth's history at the end of the Permian Period [~252 million years ago (Ma)] (*39*, *45*). At least two-thirds of marine animal genera and a comparable proportion of their terrestrial counterparts were eliminated, but the mechanisms connecting environmental change to biodiversity collapse remain strongly debated. Geological and geochemical evidence points to high temperatures in the shallow tropical ocean (*43*, *44*), an expansion of anoxic waters (*40–42*, *109*), ocean acidification (*110–113*), changes in primary productivity (*114*, *115*), and metal (*116*) or sulfide (*117*, *118*) poisoning as potential culprits. However, a quantitative, mechanistic framework connecting climate stressors to biological tolerance is needed to assess and differentiate among proposed proximal causes. In this study, we tested whether rapid greenhouse warming and the accompanying loss of ocean O_2—the two best-supported aspects of end-Permian environmental change—can together account for the magnitude and biogeographic selectivity of end-Permian mass extinction in the oceans. Specifically, we simulated global warming across the Permian/Triassic (P/Tr) transition using a model of Earth's climate and coupled biogeochemical cycles, validated with geochemical data. We then used key physiological and ecological traits measured in a diverse group of extant species to predict the magnitude and distribution of habitat loss due to the temperature-driven increase of metabolic O_2 demand amid declining supply (*119*). To assess the explanatory power of this model, we compared the predicted patterns of extinction to the global marine fossil record.

4.3 Climate warming and ocean O_2 loss

We simulated the P/Tr climate transition using the Community Earth System Model, which com- putes the exchanges of mass, energy, and momentum among interacting atmosphere, ocean, land surface, and sea ice components (Section 4.9 Supplemental Methods). Embedded in the ocean circulation are biogeochemical cycles of O_2, carbon, and nutrients driven by multiple plankton types. An initial climate state was equilibrated under low greenhouse gas concentrations and reconstructed paleogeography (Section 4.9 Supplemental Methods, *120*). The model was then subjected to an instantaneous increase in greenhouse gas concentration that was sustained for 3000 years in order to reach a warm, near-equilibrium climate (Figure 4.5). The initial climate and subsequent radiative forcing were achieved by manipulating atmospheric pCO_2 (partial pressure of CO_2) across levels chosen to reproduce tropical ocean temperatures implied by isotopic proxy records (Section 4.9 Supplemental Methods, *43*, *44*, *121*). Because the rate and timing of climate change, as well as of the resulting biotic disturbance, are not precisely known, the analysis of model output was based on pre-disturbance and post-disturbance equilibrium states, which we refer to simply as Permian and Triassic, respectively.

The modeled Permian and Triassic climates are consistent with geological proxy data for ocean temperature. The imposed increase in atmospheric pCO_2 raises model near-surface temperatures by ~11°C in the Paleo-Tethys sea (Figure 4.1A), consistent with reconstructions from the $\delta^{18}O$ of biogenic (conodont microfossil) apatite ($\delta^{18}O_{apatite}$; Figure 4.1B). Modeled warming is amplified in the near-surface ocean outside of the tropics (Figure 4.1A) and throughout the upper ocean relative to the deep (Figure 4.1C). Warming and fresh water input to the high-latitude surface ocean (Figure 4.6) together strengthen density stratification and weaken deep-water formation. From its near-modern state in the Permian, the meridional overturning circulation slows in the Triassic by more than 80% in both hemi- spheres (Figure 4.7). Deep ocean stagnation reaches its full extent after just ~300 years and persists unabated for the duration of the simulation (~3000 years).

The modeled Permian and Triassic climates are also consistent with geological proxies for marine anoxia. Abrupt warming and its attendant effects deplete the global marine O_2 inventory by ~76% (~140 mmol/m^3), leading to extensive Triassic seafloor anoxia (Figure 4.1D) that spans the entire northern portion of the Panthalassa Ocean and the eastern tropics, similar to the observed distribution of deeper-ocean sediments deposited under anoxic conditions [e.g., (*40*, *122*)]. The global fraction of anoxic bottom water (f_{anox}) in the Permian (~0.1%) is close to modern values (~0.2%) but rises to ~40% in the Triassic (Fig. 1E), consistent with the expansion inferred from uranium isotopes in marine carbonates (*41*, *42*).

O_2 loss is nearly complete in the abyss, but varies strongly with latitude throughout the upper ocean (Figure 4.1F). At high latitudes, anoxia develops in waters as shallow as 150 m. In contrast, O_2 declines weakly or increases in portions of the tropical thermocline. This pattern of O_2 change cannot be explained by decreases in gas saturation alone. It requires additional changes in the cumulative loss of O_2 from microbial respiration below the surface ocean. Warming increases the rate of phytoplankton growth, whereas stratification increases their exposure to adequate sunlight, especially in high latitudes where deep convection and sea ice cover decline markedly. As a result, surface nutrients are drawn down in mid- and high latitudes and are exported in sinking particles to the deep sea (*115*), thereby reducing the nutrient supply to the tropical surface ocean (*123*) (Figure 4.8). This shift in nutrient distribution in turn lessens the microbial O_2 demand in the tropical thermocline, partially counteracting the lowered gas saturation and limiting O_2 loss, even while anoxia develops elsewhere.

4.4 Aerobic habitat loss

The effect of warming and O_2 loss on biodiversity in the end-Permian ocean depends not only on the magnitude and pattern of environmental change, but also on the sensitivities of marine animals. Tolerances to hypoxia and warming are physiologically related (*124*) and can be represented in a single metric, the Metabolic Index (Φ), derived from the ratio of temperature-dependent rates of O_2 supply and demand (Section 4.9 Supplemental Methods, *27*):

$$\Phi = \frac{A_o pO_2}{exp\left\{\frac{-E_o}{k_B}\left[\frac{1}{T} - \frac{1}{T_{ref}}\right]\right\}} \qquad \text{Equation 4.1}$$

where pO_2 and T are the O_2 partial pressure and temperature of ambient water, respectively; k_B is Boltzmann's constant; and the parameters A_o (kPa^{-1}) and E_o (eV) represent fundamental physiological traits of a species. The inverse of A_o (i.e., $1/A_o$, in kPa) is the minimum pO_2 that can sustain the resting metabolic rate (i.e., the "hypoxic threshold") at a reference temperature (T_{ref}), and E_o is the temperature sensitivity of that threshold (Figure 4.2A). The Metabolic Index measures the capacity of an environment to support aerobic activity by a factor of Φ above an organism's minimum requirement in a complete resting state ($\Phi = 1$). For both marine and terrestrial animals, the energy required for growth and sustained activity (e.g., feeding, reproduction, defense) is elevated by a factor of ~1.5 to 7 above resting metabolic demand (*27*, *125*) and represents an ecological trait, termed Φ^{crit}. If climate warming and O_2 loss reduce the Metabolic Index for an organism below its species-specific Φ^{crit}, the environment would no longer have the capacity to support active aerobic metabolism and, by extension, long-term population persistence.

We evaluated the range and frequency of traits governing the Metabolic Index across diverse modern species (Section 4.9 Supplemental Methods). Physiological traits ($1/A_o$ and E_o) were estimated in 61 species that span benthic and pelagic habitats in all ocean basins across four phyla (Arthropoda, Chordata, Mollusca, and Cnidaria). The species include 28 malacostracans, 21 fishes, three bivalves and cephalopods, two copepods, and one each for gastropods, ascidians, scleractinian corals, and sharks (Table 4.1); their range of body mass spans eight orders of magnitude. The ecological trait (Φ^{crit}) was estimated for 26 species with adequate biogeographical data. All parameters exhibited well-defined distributions reflecting the diversity and frequency of key metabolic traits among modern taxa at multiple levels of taxonomic hierarchy (Figure 4.9) (Section 4.9 Supplemental Methods). We used the observed trait distributions to define a set of model ecophysiotypes and populate the model Permian ocean with each ecophysiotype wherever its traits and ocean conditions provide viable habitat ($\Phi \geq \Phi^{crit}$). Although modern species and the environments they encounter differ from those present during the Permian, the use of modern hypoxia traits to define Permian ecophysiotypes is grounded in two considerations. First, among well-sampled modern taxonomic groups, including arthropods, chordates,a nd mollusks, the distributions of hypoxia traits are not significantly different (Figure 4.9B to D) (Section 4.9 Supplemental Methods). This overlap of distributions implies a strong selective pressure for diverse physiological strategies for hypoxia tolerance and would apply to any cosmopolitan taxonomic group, including Permian phyla not well represented in our database. Second, the broad similarity in the temperature and O_2 conditions encountered today and in the simulated Permian climate (Figure 4.10) suggests that, whatever their other anatomical and physiological differences, the Permian aerobic environment should have selected for a range and frequency of hypoxia traits comparable to those of modern species. To test the adaptive suitability of modern trait diversity to the Permian ocean, we examined whether all ecophysiotypes find suitable habitat, and whether every region of the Permian ocean would be habitable by some subset of modern ecophysiotypes. Variations in Permian environmental conditions and the three Metabolic Index traits give rise to a diverse set of biogeographic ranges (Figure 4.2B to D). For average physiological traits of the studied species ($1/A_o \sim 4.5$ kPa and $E_o \sim 0.4$ eV), Φ decreases with depth in the upper 1000 m but increases with latitude, restricting ecophysio- types with higher ratios of active to resting metabolic rates to the extratropics (Figure 4.2B). , Variations in the hypoxic threshold have an effect on the distribution of habitat similar to that of Φ^{crit} . In contrast, the temperature sensitivity parameter determines where Φ reaches its extreme values for a given distribution of temperature and O_2 (Figure 4.2C and D). For ecophysiotypes whose hypoxic thresholds are only weakly temperature-dependent (E_o <0.1 eV), Φ is maximized in the shallow low-latitude ocean (Figure 4.2C). For the most temperature-sensitive ecophysiotypes ($E_o \sim 1.0$ eV), Φ is greatest in the relatively cold waters of the high-latitude upper ocean and aerobic habitat expands with depth (Figure 4.2D). The predicted niche partitioning leaves virtually no part of the Permian ocean uninhabited, partially confirming the relevance of modern trait diversity for the Permian.

Metabolic Index traits also have a strong impact on the predicted volume of available aerobic habitat (Figure 4.3A). Ecophysiotypes with higher temperature sensitivities are able to inhabit the largest ocean volumes because most deep waters in the simulated Permian ocean are cold. In turn, ecophysiotypes with low hypoxic thresholds and/or low values of Φ^{crit} can occupy the largest ocean regions for a given temperature sensitivity. Simulated Permian habitat is available for ~95% of modern Metabolic Index trait combinations, both as global ocean volume (points in Figure 4.3A) and as area on the seafloor (Figure 4.11A), further confirming that extant trait diversity is well adapted to the end-Permian ocean and is thus a sensible baseline for examining habitat loss and extinction.

Across the simulated climate transition, warming and O_2 loss remove a major fraction of aerobic habitat in the upper 1000 m for most ecophysiotypes (Figure 4.3B) by lowering their metabolic indices below Φ^{crit}. The loss of habitat exceeds 90% for an ecophysiotype with the average traits; the vast majority (~95%) of ecophysiotypes experience declines, with magnitudes ranging from ~20% to 100% (Figure 4.12). Habitat loss preferentially selects against organisms with high hypoxic thresholds, high ratios of active to resting metabolic rates, and/or high temperature sensitivities. The former two traits impart low initial habitat volumes (Figure 4.3A), whereas high temperature sensitivities amplify the decline in Φ per degree of warming. These patterns of differential habitat loss across ecophysiotypes are also found for coastal seafloor habitats (Figure 4.11B), and are qualitatively similar across ocean depths, but the average magnitude of habitat loss increases in the abyss because of the more complete O_2 loss (Figure 4.13).

4.5 Geography of global extinction

The severity of aerobic habitat loss predicted across the warming interval implies a high likelihood of extinction for many ecophysiotypes. We simulated the extinction of ecophysiotypes, defined by a fractional loss of global aerobic habitat volume (ΔV_i, where i indexes ecophysiotype) exceeding a specified critical threshold (V^{crit}; Figure 4.4A) (Section 4.9 Supplemental Methods), in waters above a maximum depth. Because maximum habitat depth and V^{crit} are poorly known ecological traits that are likely to vary across species, we computed the extinction across a wide range of values for these parameters. However, the geographical signature of the predicted mass extinction remains essentially the same irrespective of habitat depth and V^{crit}; extinction intensity should have been lower for tropical communities than for those at higher latitudes.

The latitudinal gradient of extinction predicted from the Metabolic Index arises from the fundamental niche partitioning of Permian ecophysiotypes across latitude prior to the warming (Figures 4.4B and 4.14A). Ecophysiotypes with higher hypoxic thresholds and/or ratios of active to resting metabolisms are preferentially exterminated when the high latitudes warm and lose O_2 because they have no escape from in hospitable conditions. In contrast, ecophysiotypes whose Permian habitat includes the tropics must have traits pre-adapted to warm, low-O_2 environments and can better exploit these conditions when they arise globally. The extinction gradient is thus predicted to occur as long as the temperature-dependent hypoxia tolerance varies among ecophysiotypes, and as long as those with lower tolerance are confined to higher-latitude waters with a greater capacity to support aerobic activity. Under these conditions, the extinction pattern is only weakly dependent on the spatial gradients of climate warming and O_2 loss (Figure 4.14B), and holds regardless of the precise frequency distribution of Permian traits (Figures 4.14B, 4.15, and 4.16); the pattern also holds if habitat is defined by area on the seafloor or volume in the water column (Figure 4.17).

To test the predicted geographic selectivity of aerobic habitat loss, we compared the model extinction patterns to the reconstructed distribution of genus extinction across latitude (Figure 4.4A and Table 4.2) derived from fossil occurrences in the Paleobiology Database (Section 4.9 Supplemental Methods). The global mean magnitude of extinction estimated from the fossil compilation (~65% of genera) agrees with globally aggregated estimates (*126*) but displays a previously undescribed gradient across latitude, consistent with the model predictions. The observed extinction intensity increases by ~20% from the tropics to high latitudes, reaching at least 75% of genera outside of the tropics in both hemispheres. This trend is found in multiple taxonomic groupings, including those phyla with traits multiply sampled among modern taxa (arthropods, chordates, and mollusks) and in those that are not (Figure 4.18A). It is also robust to latitudinal differences in sampling intensity (Figure 4.18, B to D) and changes in the preservation of major depositional environments (Figure 4.19) (Section 4.9 Supplemental Methods). The correspondence between the simulated and observed geographic patterns of selectivity strongly implicates aerobic habitat loss, driven by rapid warming, as a main proximate cause of the end- Permian extinction.

4.6 Magnitude of regional extinction

Unlike the global extinction of ecophysiotypes, regional extinction (i.e., extirpation) in the model does not depend on V^{crit} or habitat depth. The simulated extirpation is defined at a given location by the percentage of ecophysiotypes whose Metabolic Index is pushed below Φ^{crit} by Triassic climate change (Section 4.9 Supplemental Methods). Similar to global extinction, the extirpation of ecophysiotypes is elevated at higher latitudes but increases less systematically from the tropics (Figure 4.4C). This pattern of ecophysiotype loss arises from the counteracting influences of global warming and O_2

loss on local aerobic habitat. Declining seawater O_2 concentrations drive extirpation in up to ~70% of ecophysiotypes in the high latitudes, but its impact diminishes to less than ~20% of ecophysiotypes in the tropics, where O_2 loss is weak (Figure 4.1F). The effect of warming predicts the opposite pattern, with peak extirpation of ~65% at the equator dropping to ~20% at the poles. Local aerobic habitat is more sensitive per degree of warming in the tropics than in the high latitudes because Φ is already close to Φ^{crit} for the majority of Permian ecophysiotypes (Figure 4.2, B to D). The realized impact of temperature on local habitat is therefore largest in the tropics because the pattern of upper-ocean warming is relatively constant across latitude (Figure 4.1C), in contrast to the pattern of O_2 loss (Figure 4.1F).

To test the predicted intensity of regional extinction, we used fossil occurrence data to estimate the extirpation of marine genera across the end-Permian extinction (Section 4.9 Supplemental Methods). The fossil extirpation intensities are more severe than fossil extinction intensities across all latitude bands (global mean ~93% ± 8% spatial SD) but show a similar gradient, increasing outside of the tropics (Figure 4.4D). Extirpation exceeds extinction because not all locally lost genera disappeared globally, whereas all extinct genera were, by definition, extirpated everywhere. We can account for the effect of globally extinct ecophysiotypes in the model extirpation by using a combination of V^{crit} and habitat depth that predicts an equal contribution of aerobic habitat loss to both the observed regional and global extinction (Section 4.9 Supplemental Methods). Doing so increases the extirpation outside of the tropics, yielding a latitudinal gradient similar to the fossil data.

If we assume that the fossil occurrences primarily reflect habitat conditions above 500 m water depth (*127*), the global mean magnitude of ecophysiotype extirpation (67% ± 18% spatial SD) accounts for ~72% of the mean observed magnitude of genera extirpation (i.e., 93%; Figure 4.4D). Including in this comparison the spatial variations in model extirpation yields a range explaining ~53 to 92% of the observed extirpation magnitude. Additional extinctions due to temperature-dependent hypoxia would have likely arisen from ecological interactions (*128*), including food web effects, because hypoxia-tolerant species could still be eliminated if they were dependent on hypoxia-vulnerable ones. Temperature-dependent hypoxia can thus account for the majority of biodiversity losses during the end-Permian mass extinction.

4.7 Discussion

Global warming and ocean O_2 loss were accompanied by other Earth system changes during the end-Permian crisis that likely added to the effects of temperature-dependent hypoxia. In our simulations, net primary productivity is reduced by ~40% globally, with strongest declines in the low latitudes, where essential nutrient supply to phytoplankton is most curtailed (Figure 4.8). Thus, acting alone, productivity losses would amplify extinction risk outside of the high latitudes, opposite to the pattern observed in the fossils.

Outgassing of CO_2 from the Siberian Traps would also have acidified the ocean (*113*), causing additional impacts via hypercapnia and/or reduced calcification (*110*, *129*). These CO_2 effects are hypothesized to drive taxonomically selective extinctions, which may account for the ~10% lower mean genus extinction intensity for arthropods, chordates, and mollusks than for other less physiologically buffered phyla (Figure 4.18A). For the most heavily calcified animals in our modern trait dataset, the cold-water coral *Lophelia pertusa* and the scallop *Pecten maximus*, predicted losses of aerobic habitat are ~94% and ~100%, respectively, suggesting a high extinction risk for calcifiers even without a direct CO_2 effect. Attributing taxonomically selective extinction (*110*, *129*) to physiological mechanisms will require more metabolic trait data, including from CO_2 effects on both calcification and aerobic habitat (hypercapnia), and from Permian phyla underrepresented in our database. However, the latitudinal gradient of extinction arising from the carbon cycle perturbation is unlikely to explain higher rates of tropical species persistence, for the same reason that hypoxia increases extinction at higher latitudes. Because the most corrosive waters are found poleward, species least tolerant of low pH or carbonate saturation would have been confined to the tropics and thus without refuge in an acidifying ocean.

The end-Permian mass extinction resulted in the largest loss of animal diversity in Earth's history, and its proposed geologic trigger—volcanic greenhouse gas release—is analogous to anthropogenic climate forcing. Predicted patterns of future ocean O_2 loss under climate change (*10*, *130*) are broadly similar to those simulated here for the P/Tr boundary. Moreover, greenhouse gas emission scenarios projected for the coming centuries (*9*) predict a magnitude of upper ocean warming by 2300 CE that is ~35 to 50% of that required to account for most of the end-Permian extinction intensity. Given the fundamental nature of metabolic constraints from temperature-dependent hypoxia in marine biota, these projections highlight the potential for a future mass extinction arising from depletion of the ocean's aerobic capacity that is already under way.

4.8 Acknowledgements

We gratefully acknowledge the technical support of H. Frenzel, C. Bitz, S. Leung, and A. Winguth, data contributions from B. Seibel and all those who contributed to the PaleoBiology Database, the suggestions of three anonymous reviewers, and high-performance computing support from Yellowstone (ark:/85065/d7wd3xhc) provided to JP1 by NCAR's Computational and Information Systems Laboratory. This work was made possible by grants from the Gordon and Betty Moore Foundation (GBMF#3775) and the National Science Foundation (OCE-1419323 and OCE-1458967). EAS was supported by a Sloan Research Fellowship.

4.9 Supplemental Methods

4.9.1 Climate Simulation

We used the Community Earth System Model (CESM 1.2.2) with coupled atmosphere, ocean, land surface, and sea-ice components to simulate a climate perturbation during the end-Permian. The horizontal resolution of the atmosphere (CAM5) is 3.75° x 3.75° with 26 vertical layers, and nominally 3° x 3° in the ocean (POP2) with 54 vertical layers and a flat-bottom deep ocean condition. Unless otherwise specified, boundary conditions are taken from previous work (*120*, *131*), including a reduced solar constant to ~98% of the modern value, and an end-Permian land configuration.

The partial pressure of atmospheric CO_2 is used to tune the magnitude of the greenhouse effect in the model atmosphere to match geochemical proxy records of Permian/Triassic (P/Tr) near-surface ocean temperature (Figure 4.1B) (*43*, *44*, *121*). The Permian simulation is spun-up for ~2000 years with atmospheric CO_2 set to 150 ppmv, until the top of the atmosphere radiative imbalance is within -0.05 W m^{-2} over the last ~100 years and the trend in the meridional overturning circulation is small (~0.2 Sv/100 years). The Triassic simulation is initiated with an instantaneous increase in atmospheric pCO_2 to 5500 ppmv (net radiative forcing of ~18 W m^{-2} after the first year). The Triassic simulation is run under the high pCO_2 levels for ~3000 years, at which point the net energy input to the top of the atmosphere has reached < 5 % of its initial perturbation, the rates of global marine O_2 loss and upper ocean warming (0-1000m) have declined by >95% (Figure 4.5), and the meridional overturning circulation is stable (Figure 4.7C). The last 10 years of each climate simulation was used for further analysis of model output. For simplicity, we refer to the two climate states as Permian and Triassic, acknowledging that the former represents the climate of a more precise time-period of the latest Permian, and that the main extinction pulse slightly pre-dated the earliest Triassic.

A microbial ecosystem model (BEC) (*49*, *132–134*) is embedded within a general circulation model (POP2) to simulate the time-dependent global biogeochemical cycles. The internal sources and sinks of carbon (C), oxygen (O_2), phosphorus (P), nitrogen (N), and iron (Fe), are driven by 3 functional groups of phytoplankton and 1 zooplankton. Phytoplankton groups include N-fixing diazotrophs, and small and large phytoplankton. The parameterization of large, fast-growing phytoplankton is based on modern diatoms but without a silica quota, because diatoms did not evolve until well after the end-Permian (*135*). Fields of ocean temperature, salinity, O_2, alkalinity, DIC, inorganic and organic P and Fe are initialized using the end-Permian simulation output of ref. (*136*). A global temperature anomaly of 5°C is subtracted from the initial temperature field to reach climate equilibrium more rapidly. The ocean's total inventory of P is set to the modern value as determined from climatological observations (*69*). The concentration of N in the deep ocean (>1500 m) is restored to 15 times the P inventory, to mimic the effect of the oceanic "nutrient thermostat" (*137*). Riverine sources and sediment losses of C, P, and N were set to zero. We use the simulated atmospheric dust fields of ref. (*131*) as inputs of Fe to the surface ocean, assuming a Fe to dust ratio of 0.035, and scaling the global magnitude to the modern value (*138*). The BEC model was modified to include

O_2-dependent sediment Fe release according to the parameterization based on the measurements of ref. (*139*).

4.9.2 Metabolic Index Calibration

The Metabolic Index (Φ) is calibrated from laboratory measurements of hypoxic thresholds (O_2^{crit}) at multiple temperatures. Hypoxic thresholds define the condition in which the physical O_2 supply and resting metabolic demand are balanced, allowing the Metabolic Index parameters to be estimated from:

$$\Phi = A_o B^n \frac{pO_2^{crit}}{\exp\left[\frac{-E_o}{k_B}\left(\frac{1}{T} - \frac{1}{T_{ref}}\right)\right]} = 1 \qquad \text{Equation 4.2}$$

This formula is identical in content to the one presented by ref. (*27*). It differs in form because it is normalized to a reference temperature (T_{ref}), to give a coefficient (A_o) whose biological relevance is more easily interpreted. In this formulation, A_o is the inverse of pO_2^{crit}, when $T = T_{ref}$ (here specified at 15°C). The earlier version had an implicit T_{ref} of infinity so that A_o was not a directly observable quantity. While the numerical values of A_o differ between this study and ref. (*27*), the values of Φ are identical. In principle, the Metabolic Index also varies with body size (B). However, for the small number of species where that dependence can be empirically determined (i.e., 4 species), allometric scaling of the Metabolic Index is small (i.e., $n \approx 0$; (*27*)). Thus, the available data does not currently permit a quantitative test of the potential for changes in body size (the "Lilliput Effect") to ameliorate reductions in the Metabolic Index.

4.9.3 Experimental data

We expanded the database of published hypoxic thresholds at multiple temperatures (*27*), from 16 to 61 marine species (Table 4.1) (*29*, *140-163*).

Hypoxic thresholds were determined either as the onset of anaerobic metabolism (O_2^{hypox}) or mortality (O_2^{LC50}). O_2^{hypox} is identified from respirometry measurements as the ambient O_2 level at which rates of respiratory O_2 consumption begin to decline. Because suppressed metabolic rates below those required for a physiological resting state will eventually lead to mortality, both metrics approximate the metabolic threshold at which O_2 uptake falls below resting demand (i.e., $\Phi = 1$). O_2^{hypox} and O_2^{LC50} are therefore taken as interchangeable quantities, denoted O_2^{crit}. We calibrate O_2^{crit} with both O_2^{hypox} and O_2^{LC50} for species in which both estimates are available. We combine multiple estimates of O_2^{crit} for a given species if based on the same metric (2 species). When the original hypoxic threshold measurements were reported in concentration or percent saturation units, we converted them to partial pressure (pO_2) using the solubility of O_2 in seawater under experimental temperature, a salinity of 35 psu, and at standard atmospheric pressure.

The hypoxic threshold coefficient, $\frac{1}{A_o}$ (kPa), of the metabolic index and its temperature dependence, E_o (eV), were determined from the intercept at a reference temperature (T_{ref}) and the slope of the linear regression of ${}^{1}\!/_{k_B T}$ versus the natural log of pO_2^{crit} (Figure 4.9A). 15 species (two with separate $O_2^{hypoxic}$ and O_2^{LC50} measurements) display statistically significant relationships between pO_2^{crit} and temperature ($p < 0.05$). These studies all have at least 3 experimental temperatures, spanning a range of $> 5^oC$, and yield interspecies ranges of E_o from -0.09 to 1.06 eV, and of $\frac{1}{A_o}$ from 1.9 to 16 kPa (ie. A_o from 6.3 to 54 atm^{-1}). We also include additional O_2^{crit} data from the remaining species in the dataset if their estimated parameters lie within this prior range. Traits for each of these remaining species are derived from at least two O_2^{crit} measurements, spanning a temperature range of $\geq 3^oC$. The full distributions of E_o (n = 61;Figure 4.9B) and $\frac{1}{A_o}$ (n = 53; Figure 4.9C) are indistinguishable from those based only on species with statistically significant relationships between O_2^{crit} and temperature. We also find no difference between the distributions of estimated $\frac{1}{A_o}$ for the metabolic index based on O_2^{hypox} alone or with O_2^{LC50} measurements included.

We used analysis of variance (ANOVA) to look for differences in the metabolic traits E_o, $\frac{1}{A_o}$, and a third trait $\underline{\Phi^{crit}}$ (discussed in the section below) across phyla (i.e. Arthropoda, Chordata, Cnidaria, Mollusca). We find no statistically significant differences across phyla for any of the three traits, and that the majority of variation (78 - 99%) occurs within phyla. We additionally used ANOVA to determine the amount of variation in E_o and $\frac{1}{A_o}$ across and within genera. For both traits, we find the majority (>80%) of variation occurs across genera, implying that the observed trait diversity applies to both levels of taxonomic hierarchy. Not enough genera in the dataset contain multiple species with measured Φ^{crit} to perform this analysis for that parameter. To limit the introduction of variability from methodological differences between O_2^{hypox} and O_2^{LC50}, ANOVA analyses are based on metabolic traits calibrated using O_2^{hypox} data alone.

4.9.4 Determination of Φ^{crit}

The active to resting energy requirement, termed critical metabolic index (Φ^{crit}), was estimated for the species within our dataset by computing the Metabolic Index using the measurements of E_o and $\frac{1}{A_o}$, in combination with paired species biogeographic occurrence data, temperature and O_2 measurements. Occurrence and hydrographic data were downloaded from the Ocean Biogeographic Information System Mapper in May of 2017 (*164*). O_2 concentrations were converted to pO_2 using the solubility of O_2 in seawater under in situ temperature and pressure, and a salinity of 35 psu. For species whose allometric scaling parameter is known, their Metabolic Index is scaled by the ratio of in situ to laboratory body sizes raised to the allometric exponent (*27*).

The ecological parameter, Φ^{crit}, was estimated using two methods: statistically, as the value of the Metabolic Index above which 90% of occurrences are found (percentile method), and visually, as the first change point in the cumulative histogram of species occurrences (change point method). Both estimates yield similar results. We estimate Φ^{crit} for species in which at least 100 occurrences are available. Because paired hydrographic-occurrence data is unavailable for *Diplodus puntazzo* from the Ocean Biogeographic Information System, we use the value of Φ^{crit} estimated in (*27*). In rare instances (< 0.5%), species occurrences are found in waters in which mean climatological Φ falls below 1. This condition is physiologically unsustainable, and likely results from transient species movements, or a mismatch between the climatological temperature and O_2 fields used to compute Φ and the true *in situ* hydrographic conditions at the time occurrence data were recorded. These occurrences are removed from the Φ^{crit} analysis, despite having little impact on our estimates of Φ^{crit}. Of the 27 species for which Φ^{crit} can be measured, 26 estimates exceed the resting value (i.e. $\Phi^{crit} > 1$). One additional species, an oxygen minimum zone fish (*Melanostigma pammelas*) with relatively few occurrences in a region of strong temporal O_2 variability, exhibited a Φ^{crit} below a resting metabolic rate requirement. We use the remaining 26 species to build the histogram of Φ^{crit}, which ranges from 1.3 to 6.5 (Figure 4.9D). The frequency distribution of marine species is indistinguishable from that estimated independently from the ratio of field to resting metabolic rates in terrestrial animals (36 species), including birds, mammals and reptiles (*125*).

4.9.5 Fossil Data

Fossil occurrence data were downloaded from the Paleobiology Database on August 8, 2017 selecting all Phanerozoic occurrences of animals (*165*). Occurrences lacking genus resolution were then excluded. Subgenera were elevated to genus rank and genus names were replaced with senior synonyms as applicable. Occurrences not resolved to a geological age were excluded. Occurrences with collections identified to non-marine depositional environments were excluded. Occurrences lacking a phylum or class assignment were excluded. Occurrences assigned to protistan groups were excluded. Occurrences assigned to classes Insecta, Amphibia, and Reptilia were excluded as entirely non-marine during the interval of interest. Form taxa, ichnotaxa, and genus occurrences qualified by ‘‘aff.,’’ ‘‘cf.,’’ ‘‘ex gr.,’’ “informal,” ‘‘sensu lato,’’ ‘‘?,’’ and quotation marks were also excluded.

4.8.6 Survival Status

Genera with occurrences assigned to the Changhsingian Stage of the Permian Period but with no younger occurrences in the Paleobiology Database were considered to be extinction victims. Genera with occurrences assigned to the Changhsingian Stage of the Permian Period and with younger occurrences in the Paleobiology Database were considered to be survivors.

4.9.7 Data Analysis

Paleolatitudes of all occurrences were binned into 10° bands centered on the values 80° S through 80° N at 10° intervals (Table 4.2). For the analysis of extinction intensity, the percentage of genera occurring within the band that did not survive into the Triassic was tabulated. For the extirpation analysis, occurrences of Induan Age (earliest Triassic) were also binned by paleolatitude and the extirpation intensity was calculated as the percentage of genera with occurrences in a given paleolatitude band during the Changhsingian that did not have occurrences within the same paleolatitude band during the Induan. Latitude bands missing fossil collections in either the Changhsingian or Induan were excluded from the analysis. In each analysis, a single genus could be counted in more than one paleolatitude band if it had occurrences in more than one paleolatitude band during the Changhsingian. Of note, no Permian survivors have Olenekian but not Induan occurrences. Consequently, there is no effect on the results of assessing extinction and extirpation relative to the Induan fossil record versus the entire Lower Triassic fossil record.

The extinction analysis was performed for genera from three different taxonomic groupings: all phyla together, the three phyla multiply sampled in the modern physiological dataset (arthropods, chordates and mollusks), and all other phyla together (Figure 4.18A). We find a similar latitudinal pattern of extinction – increasing away from the tropics – regardless of taxonomic grouping. Because of differences in modes and potentials for fossil preservation between these groups, a similar latitudinal extinction pattern would not be expected if driven by taphonomic biases.

To test whether the observed latitudinal trends in extinction are driven by differences in sampling intensity across latitude, we plotted extinction percentage versus the change in the number of fossil collections within a latitude band as well as the change in the number of sampled genera from the Permian (Changhsingian) to the Triassic (Induan) (Figure 4.18B and C). Neither measure of sampling intensity shows a significant correlation with extinction intensity. We also evaluated whether the absolute sampling in the Triassic versus latitude was a control on the apparent extinction of Permian genera, but there is no significant correlation between the percent extinction and sampling intensity (Figure 4.18D). This lack of statistical association is inconsistent with a model in which the observed latitudinal variation in extinction reflected a latitudinal gradient in post-extinction sampling rather than a biological gradient in the intensity of extinction. Furthermore, the main latitudinal trend – increased extinction away from the tropics – is found when including all data together or when restricting to the best-sampled latitude bands in the Permian (Figure 4.18A).

We also examined the role of preferential changes in depositional environment with respect to latitude using the environmental information recorded for each collection in the Paleobiology Database (Figure 4.19). The analysis shows no evidence that the latitude trend in extinction intensity would be related to a change in preserved environments. Most collections (and their associated occurrences) are classified as either ‘marine indeterminate’ or ‘carbonate indeterminate’ for their depositional environment. There is a noticeable decline in the proportional representation of the carbonate indeterminate environment from the Permian to the Triassic. Because carbonate sediments are almost exclusively tropical in their distribution, this shift would be expected, if anything, to be associated with greater extinction intensity in the tropics, the opposite of the pattern actually observed.

4.9.9 Model Ecophysiotypes, Habitat, and Extinction

Here we define the primary metrics analyzed in the main text, including model ecophysiotypes, their potential aerobic habitat volume, extinction, and extirpation. Quantities that vary spatially are indicated as functions of location, x, while quantities that vary among ecophysiotypes are indexed with a subscript, *i*. For example, the spatial pattern of Metabolic Index for ecophysiotype *i* – the quantity from which all other metrics are derived - is denoted $\Phi_i(x)$.

We define a set of animal ecophysiotypes distinguished by the combination of the two physiological traits, A_o and E_o, and the ecological trait, Φ^{crit}. The frequency of ecophysiotypes with a given trait combination *i* is established based on Probability Density Functions (PDFs) constructed independently for each trait from the distributions observed in modern organisms (Figure 4.9B-D). These distributions are taken to be a random sampling of the temperature-dependent hypoxia traits of global species, and thus to reflect the true relative frequency of those traits in modern biota. This assumption should hold provided the studied species were not chosen specifically for their peculiar or extreme physiological characteristics, which would skew the distributions. The assumption of representative trait distributions is supported by the fact that the data reveal well-defined modal shapes, and the organisms within the dataset inhabit the full range of oceanic temperatures (-2 to 29.5°C) and oxygen levels (<5µM to 400 µM). One outlier species (*Pleuroncodes planipes*) was neglected in the construction of the PDFs because it was specifically targeted for its tolerance to near-anoxic conditions (*166*, *167*), and would therefore give undue weight to an extremophile physiology in the tails of the PDFs. Including its high A_o value (~340 atm^{-1}) would have further strengthened the predicted latitudinal extinction gradient by lowering extinction in the tropical oxygen deficient zones. However the impact on our results is minimal because the tails of the PDFs are thin, and the oxygen deficient zones are small in the Permian prior to warming (<1% of ocean volume).

We use a normal distribution to construct the trait PDF for E_o , and log-normal distributions for both A_o and Φ^{crit} (Table 4.3). We note that the latitudinal pattern and magnitude of the extinction do not rest on the choice of distribution functions (Figure 4.14B). The total frequency of each ecophysiotype (w_i) is computed as the product of its individual trait frequencies measured from the PDFs: $w_i = w_i^E \times w_i^A \times w_i^C$.

The total number of model ecophysiotypes is thus equal to the sum of frequencies across trait combinations: $n = \sum_i w_i$.

4.9.10 Metabolic Index

We populated the model ecophysiotypes throughout the simulated Permian (P) and Triassic (Tr) oceans by applying the Metabolic Index to the predicted fields of temperature and O_2 from the Community Earth System Model. The Metabolic Index is computed from fields of temperature and O_2, averaged over the last 10 years of each climate simulation. The distribution of the Metabolic Index was then used to define the potential aerobic habitat of each ecophysiotype. Potential aerobic habitat is defined as locations in which the annual mean Metabolic Index is equal to or exceeds an ecophysiotype's active to resting metabolic rate (i.e. $\Phi_i(x) \geq \Phi_i^{crit}$). Because of its nonlinearity, Φ was calculated for each month before averaged across time. We tested the impact of using annual minimum Φ, which ensures a specific region is viable year round, but find this has a negligible influence on the predicted extinction. We note that the predicted distribution of potential aerobic habitat indicates which regions of the ocean are capable of supporting an ecophysiotype's active metabolism, but does not imply that every region of its available habitat will necessarily be occupied.

The distribution of potential aerobic habitat is used to define a binary index [$h_i(x)$] of an ecophysiotype's occurrence as:

$$h_i(x) = \begin{cases} 0 & \Phi_i(x) < \Phi_i^{crit} \\ 1 & \Phi_i(x) \geq \Phi_i^{crit} \end{cases}$$

Equation 4.3

The index is assigned a value of 1 in locations that can support aerobic metabolism, and a value of zero where aerobic metabolism is not possible. It follows that the potential ecophysiotype richness at any location [$r(x)$] is equal to the sum of the occurrence index [$h_i(x)$] across ecophysiotypes, scaled by their relative frequencies (w_i), according to:

$$r(x) = \sum_i h_i(x) \cdot w_i \qquad \text{Equation 4.4}$$

The contribution of a given ecophysiotype to the potential richness of the local community [$f_i(x)$] is then given as the product of its trait frequency times its occurrence index [$h_i(x)$] and divided by the local potential richness as:

$$f_i(x) = \frac{w_i h_i(x)}{r(x)} \qquad \text{Equation 4.5}$$

4.9.11 Aerobic Habitat Volume

The ecophysiotype occurrence index is also used to quantify the total volume of aerobic habitat available for an ecophysiotype (V_i; m^3) in each climate simulation. V_i is computed as the sum of grid-cell volumes [$\delta V(x)$] above a maximum depth potentially inhabited by an ecophysiotype, according to its occurrence index [$h_i(x)$] as:

$$V_i = \sum_x h_i(x) \cdot \delta V(x) \qquad \text{Equation 4.6}$$

Changes in an ecophysiotype's volume of aerobic habitat are calculated relative to its Permian habitat volume (V_i^P). These changes are evaluated from the difference in an ecophysiotype's occurrence index [$\Delta h_i(x)$] between the Permian and Triassic simulations [i.e. $\Delta h_i(x) = h_i^P(x) - h_i^{Tr}(x)$] as:

$$\Delta V_i = \frac{\sum_x \Delta h_i(x) \cdot \delta V(x)}{V_i^P} \qquad \text{Equation 4.7}$$

In plots of relative habitat changes (i.e., Figures 4.3B, 4.11B,4.12,4.13), the sign of the relative habitat changes is reversed so that negative values indicate Permian habitat loss and positive values indicate habitat gain.

4.9.12 Ecophysiotype Global Extinction

Ecophysiotype extinction is calculated from the relative changes in Permian global aerobic habitat volume (ΔV_i) under Triassic warming and O_2 loss. ΔV_i is used to define a binary index [e_i] of ecophysiotype extinction (assigned 1) or survival (assigned 0). The value of e_i is determined by whether ΔV_i (in %) exceeds a specified critical threshold (V^{crit}) as:

$$e_i = \begin{cases} 0 & \Delta V_i < V^{crit} \\ 1 & \Delta V_i \geq V^{crit} \end{cases}$$

Equation 4.8

The extinction percentage of model ecophysiotypes in location x [i.e. $e(x)$] is then diagnosed as the sum of the extinction index [e_i], across ecophysiotypes, scaled by each ecophysiotype's fractional contribution to the total Permian community richness [$f_i^P(x)$] as:

$$e(x) = \sum_i f_i^P(x) \cdot e_i$$

Equation 4.9

The extinction index is computed across a range of maximum habitat depths and V^{crit}, from 500-4000 m and 40-95%, repectively (Figure 4.4A). Although the magnitude of the predicted extinction depends on both maximum habitat depth and V^{crit}, its latitudinal pattern is robust to uncertainty in these parameters.

4.9.13 Ecophysiotype Regional Extinction (i.e. Extirpation)

The geography of aerobic habitat loss can also be used to predict the magnitude of the regional extinction, termed extirpation. Extirpation occurs in locations where the Metabolic Index meets the active demand of an ecophysiotype in the Permian ($\Phi \geq \Phi^{crit}$), but falls below this threshold in the Triassic ($\Phi < \Phi^{crit}$). The extirpation of ecophysiotype *i* from location x is determined by the difference in $h_i(x)$, termed Δh(x), between the Permian and Triassic simulations, i.e. $\Delta h(x) = h_i^P(x) - h_i^{Tr}(x)$, and occurs when $\Delta h = 1$. Additionally, for globally extinct ecophysiotypes (i.e. $e_i = 1$), extirpation occurs in all locations. An ecophysiotype is therefore counted as extirpated from location *x* if either $h_i(x) = 1$ or if $e_i = 1$. Extirpation [$\Delta r(x)$] is diagnosed as the maximum of $\Delta h_i(x)$ and $e_i(x)$ scaled by their fractional contribution to the total community richness in the Permian [$f_i(x)^P$], and summed across ecophysiotypes *i* as:

$$\Delta r(x) = \sum_i f_i^P(x) \cdot \max\{\Delta h_i(x), e_i\} \qquad \text{Equation 4.10}$$

We first estimate the magnitude of regional extinction [$\Delta r(x)$] only considering local aerobic habitat change [$\Delta h_i(x)$; i.e. $e_i = 0$], which does not depend on V^{crit} or the maximum habitat depth (Figure 4.4C). To compute the contribution of globally extinct ecophysiotypes (e_i) to the regional extinction, we assume a combination of V^{crit} and the maximum habitat depth that explains a comparable fraction of regional and global extinction in the fossil record. Across V^{crit} and habitat depth combinations that satisfy this condition (i.e. V^{crit} = 70% at 500 m, 80% at 1000 m, and ~95% at 4000 m), the predicted magnitudes of regional and global extinction are roughly constant. The modeled latitudinal patterns of regional extinction intensity (Figure 4.4D) are therefore insensitive to which combination is assumed.

4.10 Figures

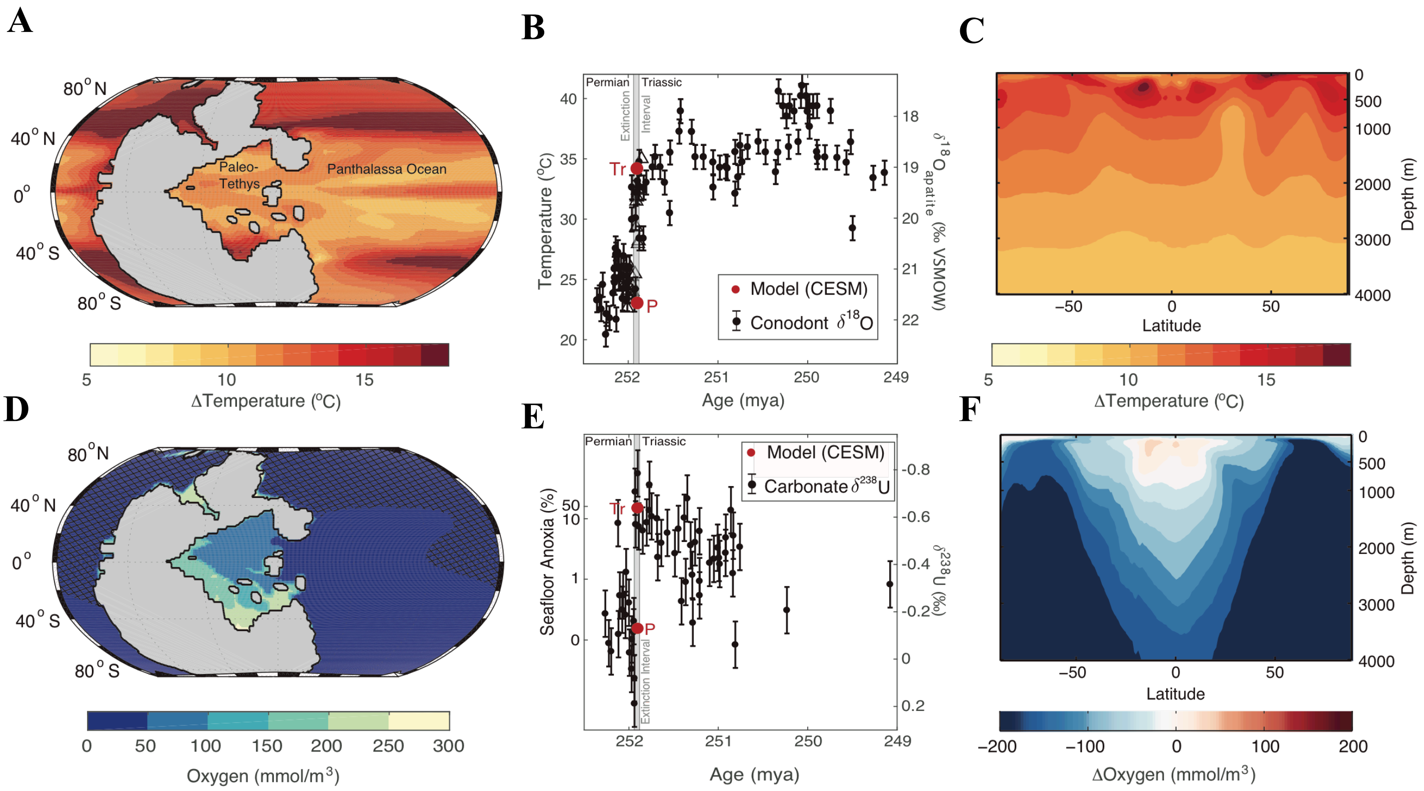

Figure 4.1. Permian/Triassic ocean temperature and O_2. (**A**) Map of near-surface (0-70m) ocean warming across the Permian/Triassic (P/Tr) transition simulated in the Community Earth System Model. The grey shaded region represents the supercontinent Pangea. (**B**) Simulated near-surface ocean temperatures (red circles) in the eastern Paleo-Tethys [5°S to 20°N] and reconstructed from conodont $\delta^{18}O$ apatite ($\delta^{18}O_p$) measurements (black circles; *44*). The timescale of the $\delta^{18}O_p$ data (circles) has been shifted by 0.7 my to align it with $\delta^{18}O_p$ calibrated by U-Pb zircon dates (triangles; *45*), which also define the extinction interval (gray band). Error bars are 1°C. (**C**) Simulated zonal mean ocean warming (°C) across the P/Tr transition. (**D**) Map of seafloor oxygen levels in the Triassic simulation. Hatching indicates anoxic regions ($O_2 < 5$ mmol/m³). (**E**) Simulated seafloor anoxic fraction f_{anox} (in %; red circles). Simulated values are used to drive a published one-box ocean model of the ocean's uranium cycle (*42*) and compared to $\delta^{238}U$ isotope measurements of marine carbonates formed in the Paleo-Tethys (black circles). Error bars are 0.1‰. (**F**) Same as in (**C**), but for simulated changes in O_2 concentrations (mmol/m³).

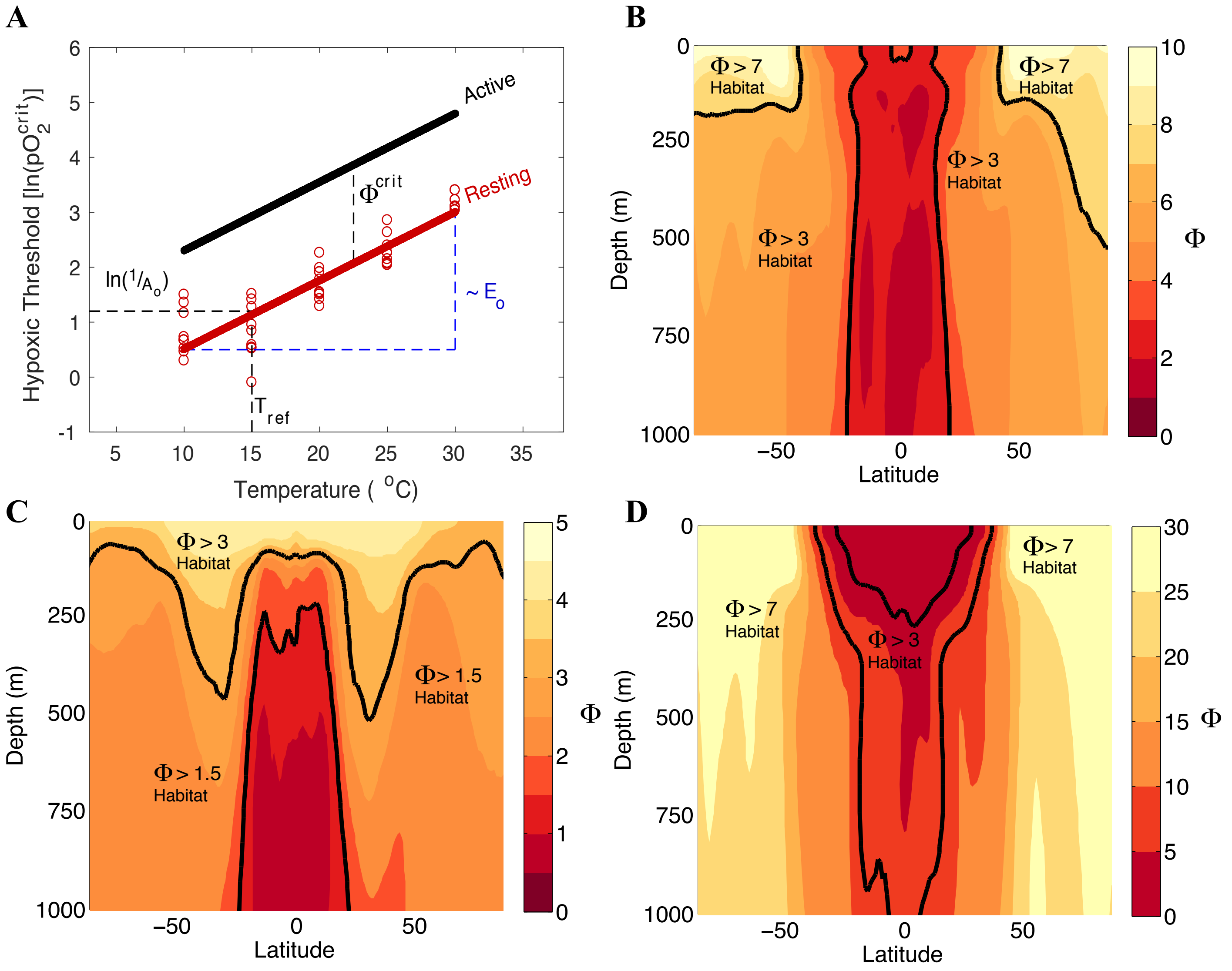

Figure 4.2. Physiological and ecological traits of the Metabolic Index (Φ) and its end-Permian distribution. (**A**) The critical O_2 pressure (pO_2^{crit}) needed to sustain resting metabolic rates in laboratory experiments (red circles, *Cancer irroratus*) vary with temperature with a slope proportional to E_o from a value of $1/A_o$at a reference temperature (T_{ref}), as estimated by linear regression when $\Phi = 1$ (Section 4.9 Supplemental Methods). Energetic demands for ecological activity increase hypoxic thresholds by a factor Φ^{crit} above the resting state, a value estimated from the Metabolic Index at a species' observed habitat range limit. (**B**) Zonal mean distribution of the Metabolic Index (Φ) in the Permian simulation, for ecophysiotypes with average $1/A_o$ and E_o (~4.5 kPa and 0.4 eV, respectively). (**C** and **D**) Variations in Φ for an ecophysiotype with weak (**C**) and strong (**D**) temperature sensitivities (E_o = 0 eV and 1.0 eV, respectively), both with $1/A_o$ ~ 4.5 kPa. Example active to resting metabolic rates (Φ^{crit}; black lines) outline different distributions of available aerobic habitat for a given combination of $1/A_o$ and E_o.

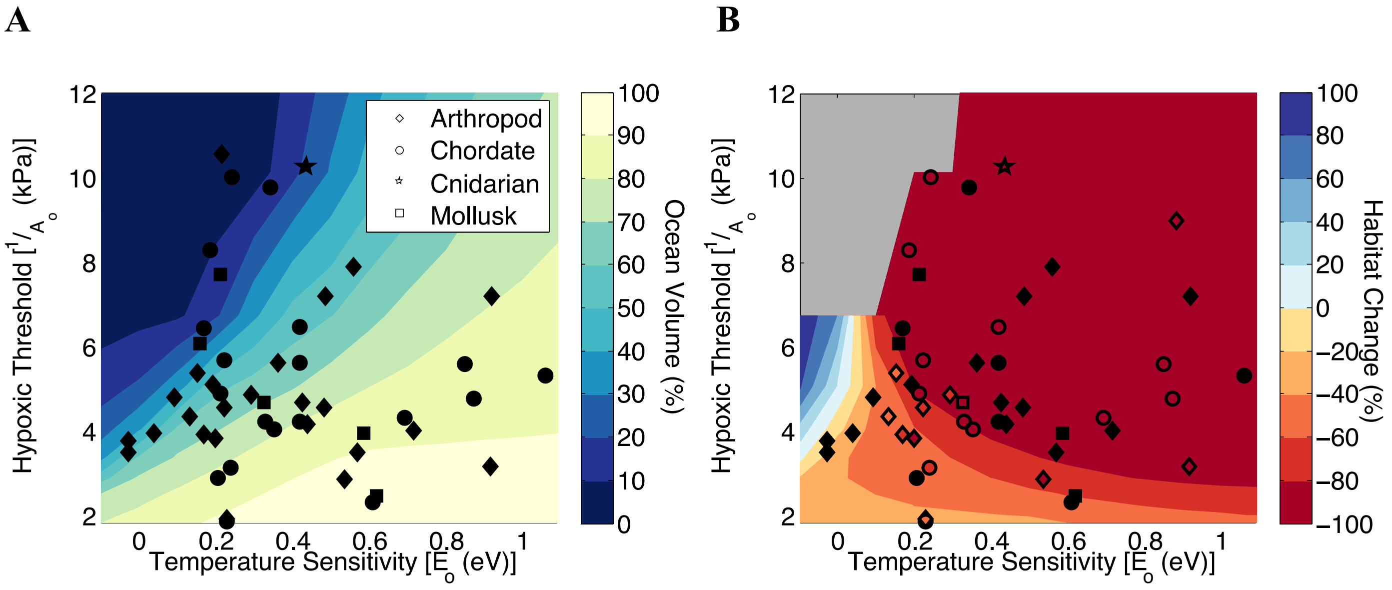

Figure 4.3. Aerobic habitat during the end-Permian and its change under warming and O_2 loss. (**A**) Percentage of ocean volume in the upper 1000 m that is viable aerobic habitat ($\Phi \geq \Phi^{crit}$) in the Permian for ecophysiotypes with different hypoxic threshold parameters [$1/A_o$ (kPa)] and temperature sensitivities [E_o (eV)]. (**B**) Relative (percent) change in Permian aerobic habitat volume (ΔV_i, where i indexes ecophysiotype) under Triassic warming and O_2 loss. Colored contours are for ecophysiotypes with $\Phi^{crit} = 3$. Measured values of $1/A_o$ and E_o in modern species are shown as black symbols, but in (**B**) these are colored by habitat changes at a species' specific Φ^{crit} where an estimate of this parameter is available. The grey region at upper left indicates trait combinations for which no habitat is available in the Permian simulation.

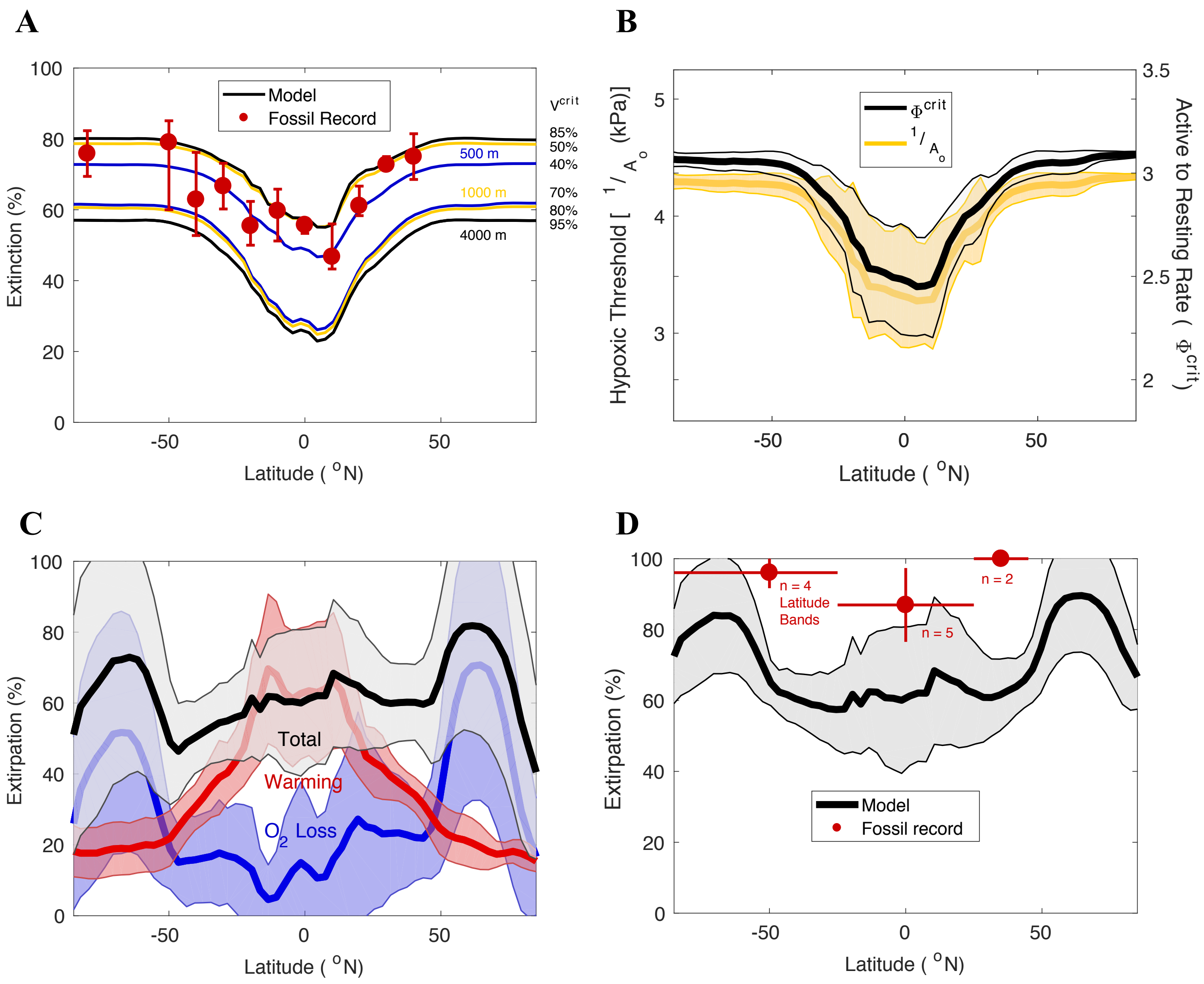

Figure 4.4. Global and regional extinction at the end of the Permian. (**A**) Global extinction versus latitude, as predicted for model ecophysiotypes and observed in marine genera from end-Permian fossil occurrences in the Paleobiology Database (PBDB). Model extinction is calculated from the simulated changes in Permian global aerobic habitat volume (ΔV_i) under Triassic warming and O_2 loss (Section 4.9 Supplemental Methods). The maximum depth of initial habitat and fractional loss of habitat resulting in extinction (V^{crit}) are varied from 500 – 4000 m (colors) and 40 – 95% (right-axis labels), respectively. The observed extinction of genera combines occurrences from all phyla in the PBDB (points). Error bars are the range of genera extinction across two taxonomic groupings: phyla multiply sampled in the modern physiology data (arthropods, chordates, and mollusks) and all other phyla. Latitude bins with fewer than five Permian fossil collections are excluded. The average range is used for latitude bins missing extinction estimates from both taxonomic groupings (i.e. 80°S, 30°S and 40°N). The main latitudinal trend – increased extinction away from the tropics – is found when including all data together and when restricting to the best-sampled latitudinal bins (Figure 4.18). In all panels, model values are averaged across longitude and above 500 m. (**B**) Average hypoxic threshold and Φ^{crit} across ecophysiotypes versus latitude in the Permian. In (B-D), shading represents the 1σ standard deviation at each latitude. (**C**) Regional extinction (i.e. extirpation) versus latitude for model ecophysiotypes, with individual contributions from warming and the loss of seawater O_2 concentration. Extirpation occurs in locations where the Metabolic Index meets the active demand of an ecophysiotype in the Permian ($\Phi \geq \Phi^{crit}$), but falls below this threshold in the Triassic ($\Phi < \Phi^{crit}$). (**D**) Same as in (C), but including globally extinct ecophysiotypes (using a maximum habitat depth of 1000 m and $V^{crit} = 80\%$), and as observed in marine genera from end-Permian and early-Triassic fossil occurrences of all phyla in the PBDB. Observed extirpation magnitudes are averaged across tropical and extra-tropical latitude bands (red points and horizontal lines). Regional 1σ standard deviations are shown as vertical lines.

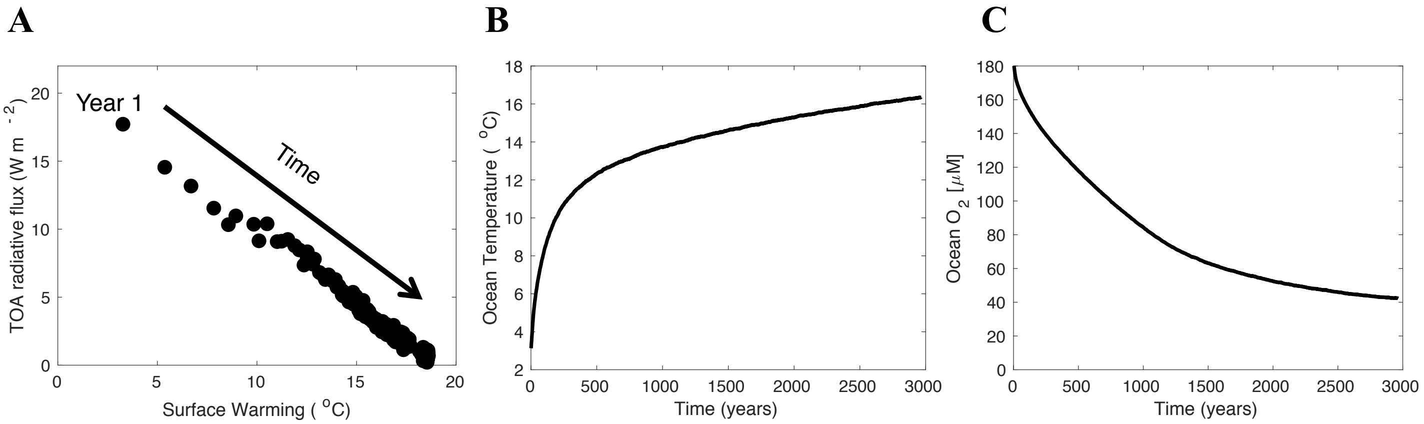

Figure 4.5. Permian/Triassic atmospheric energy balance and changes in ocean temperature and O_2. (**A**) Annual mean net radiation flux into the top of the atmosphere (W m^{-2}) versus mean surface warming (^{o}C) in the Community Earth System Model after an initial instantaneous increase in atmospheric pCO_2 at the start of the Triassic simulation, and for 3000 years thereafter. Atmospheric radiative forcing is ~18 W m^{-2} after the first model year, and < 5% of this value after 3000 years. (**B** and **C**) Time-series of simulated Triassic ocean temperature in the upper 1000 m and oxygen (O_2) in the upper 4000 m. In the last 100 years of the Triassic simulation, rates of ocean warming and O_2 loss have declined by >95% relative to the first 100 years.

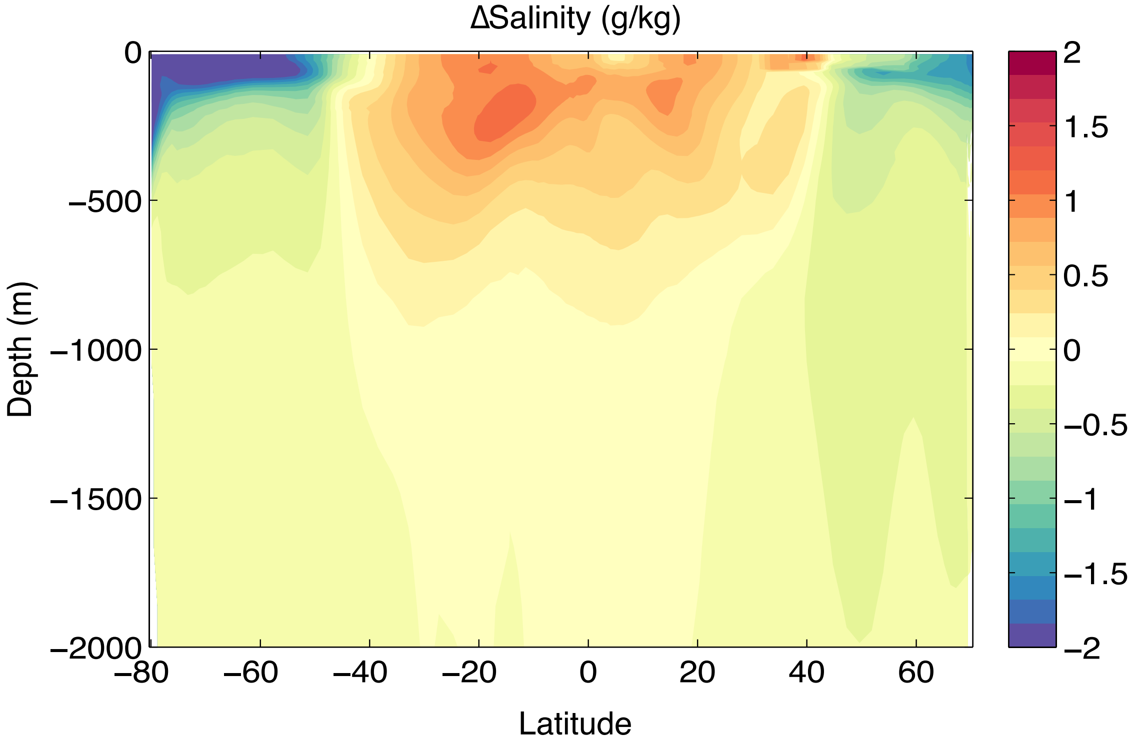

Figure 4.6. Permian/Triassic salinity changes. Triassic minus Permian zonal mean changes in ocean salinity (g/kg) predicted by the Community Earth System Model. Freshening of the high-latitudes results from a net increase in atmospheric moisture transport from the tropics to the poles in addition to the melting of sea-ice.

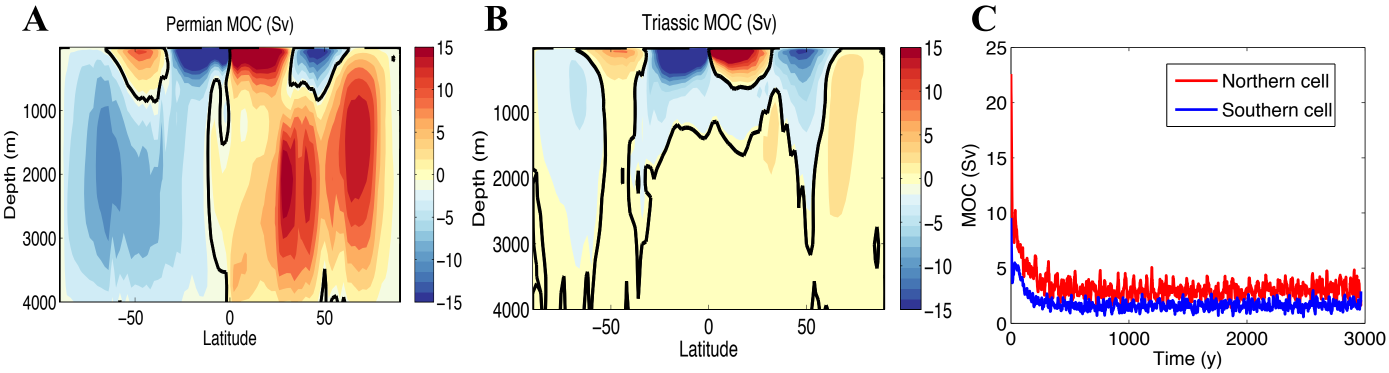

Figure 4.7. Permian/Triassic meridional overturning circulation (MOC). Simulated Permian (**A**) and Triassic (**B**) meridional overturning circulation (in Sv) in the Community Earth System Model, and an index of its strength over time from the southern and northern hemispheres (**C**). 1 Sv = 10^6 m^3 s^{-1}. The meridional overturning circulation index is defined as its maximum value at 2000 m in each hemisphere.

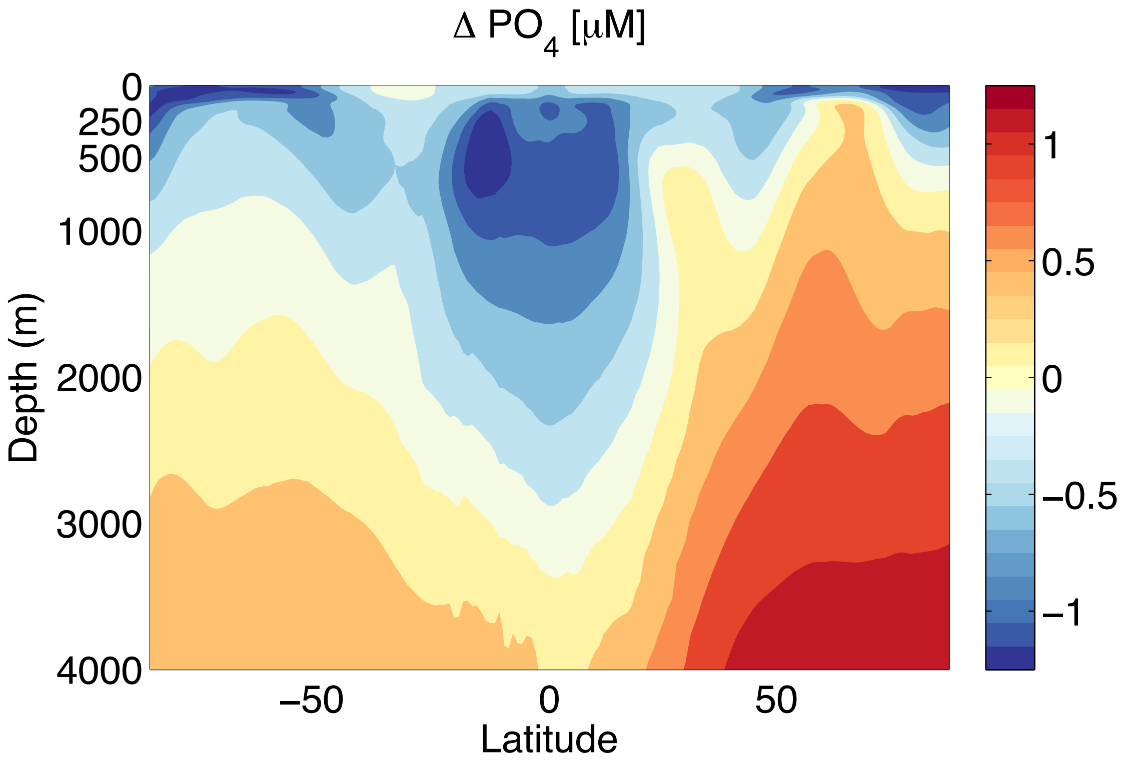

Figure 4.8. Permian/Triassic phosphate changes. Triassic minus Permian zonal mean changes in ocean phosphate (PO_4^{3-}, in μM) predicted by the Community Earth System Model. PO_4^{3-} declines in the upper ocean, but increases in the deep sea because of nutrient trapping by sinking particles under a slowed overturning circulation.

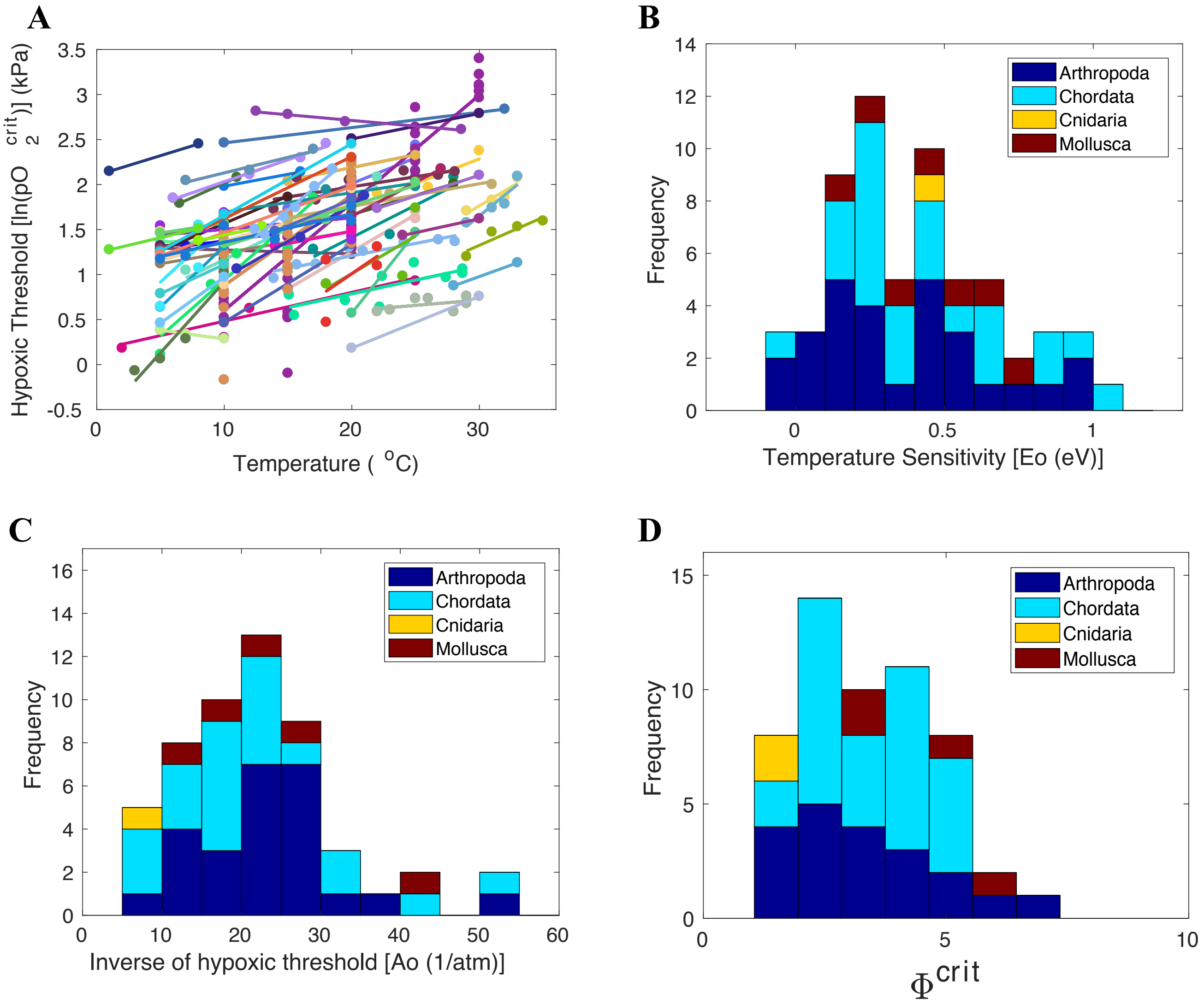

Figure 4.9. Physiological and ecological traits of the Metabolic Index. (**A**) The critical O_2 pressure (pO_2^{crit}) needed to sustain resting metabolic rates in laboratory experiments (circles) vary with temperature with a slope proportional to E_o from a value of $1/A_o$ at a reference temperature (T_{ref}), as estimated by linear regression (lines) when $\Phi = 1$. (**B** and **C**). Frequency distributions of the physiological traits E_o and A_o estimated from laboratory measurements. Of note, while most values of E_o are positive, a given species can exhibit an E_o below 0 eV if the physiological temperature sensitivity of its O_2 supply exceeds that of its metabolic demand (e.g. 142). (**D**) Distribution of an ecological trait, Φ^{crit}, the active to resting metabolic rate. Φ^{crit} values are estimated as the lowest values of the Metabolic Index in a species geographic range using the laboratory derived traits and species occurrence data (164). In (**B**-**D**) the distributions of all three traits are similar across phyla. The frequency distribution of Φ^{crit} in marine species is also indistinguishable from that of active to resting metabolic rates estimated in terrestrial animals (36 species), including birds, mammals, and reptiles (125).

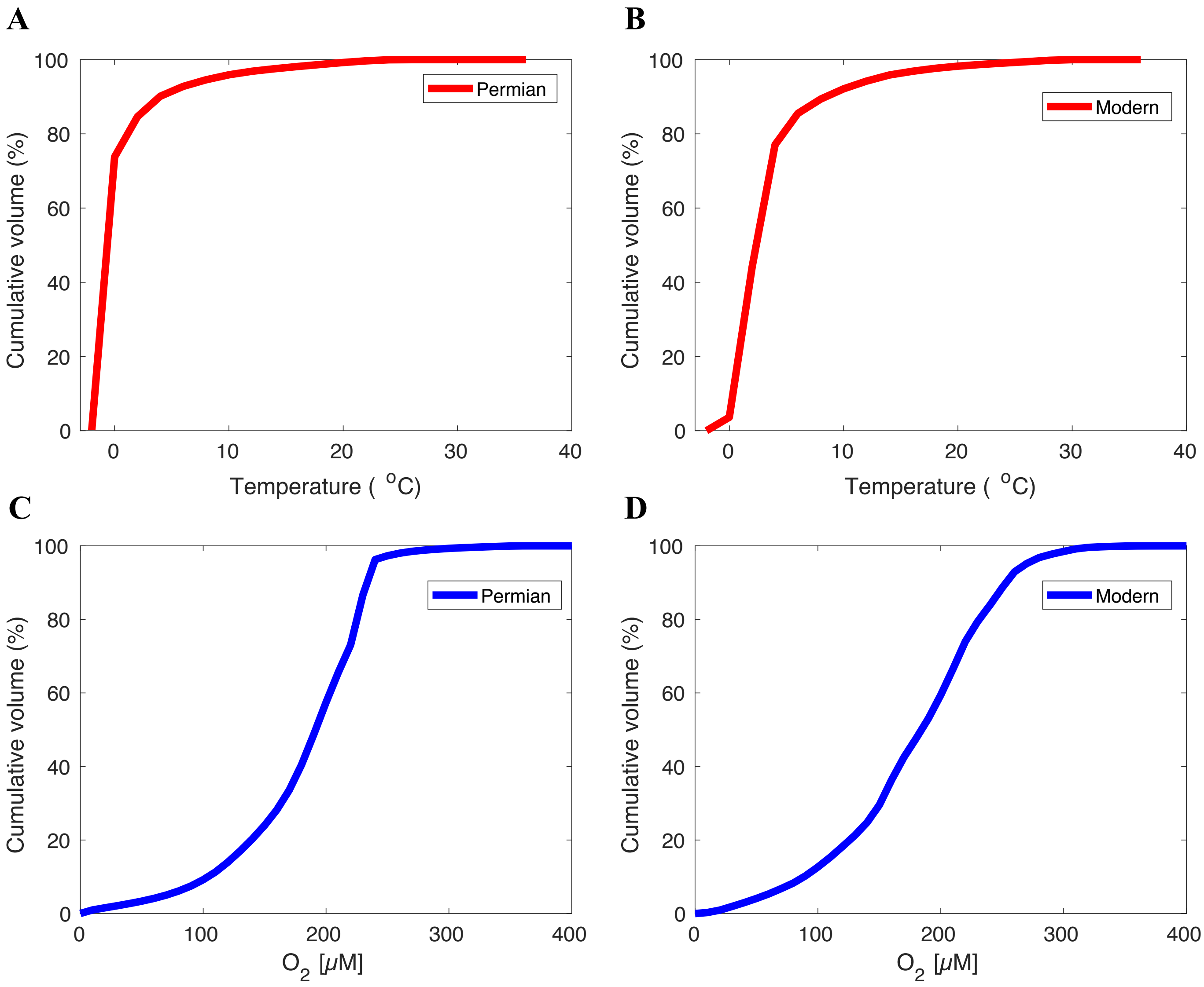

Figure 4.10. Comparison of end-Permian and modern climates. Cumulative histogram of the ocean's volume below a given temperature (°C) (**A** and **B**) and oxygen (O_2) concentration [μM] (**C** and **D**), in the Permian simulation of the Community Earth System Model (left panels) and in modern observations (right panels). Cumulative histograms are normalized to total ocean volume. Observed values are computed from the World Ocean Atlas monthly climatology (4,185). Monthly temperature and O_2 fields are annually averaged before analysis.

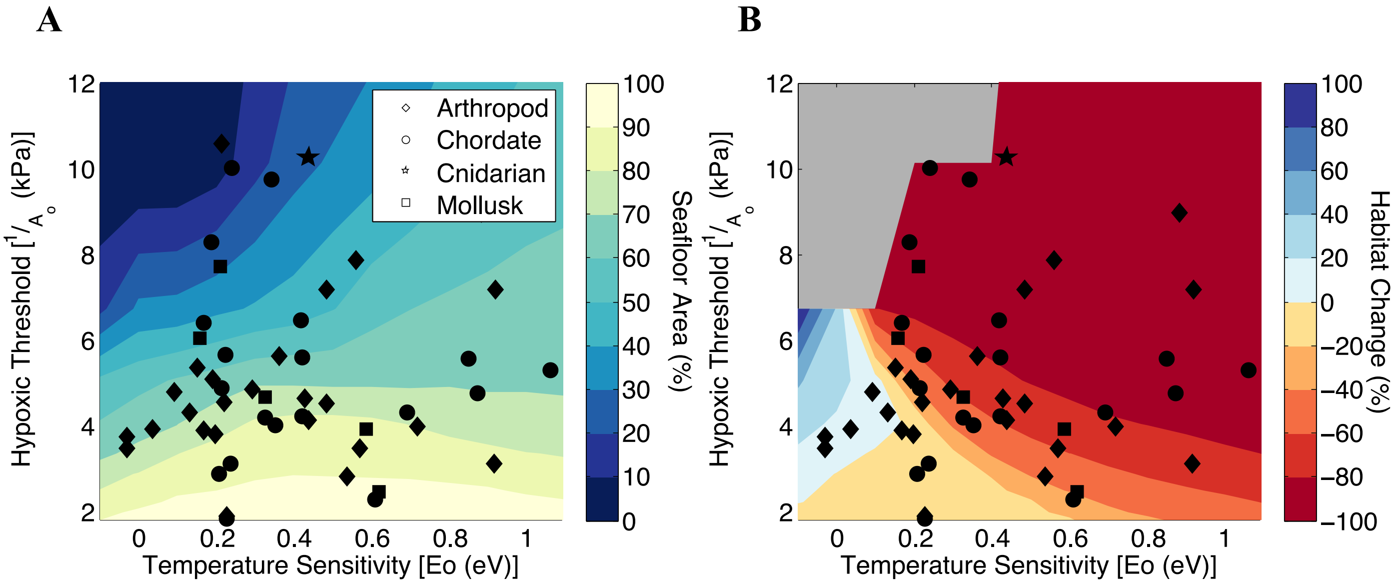

Figure 4.11. End-Permian seafloor aerobic habitat area and its change under warming and O_2 loss. (**A**) Fraction (%) of seafloor area in the upper 1000 m that is viable aerobic habitat ($\Phi \geq \Phi^{crit}$) in the Permian for ecophysiotypes with different hypoxic threshold parameters and temperature sensitivities. Seafloor above 1000 m is restricted to coastal regions. (**B**) Relative change in Permian aerobic habitat area (ΔA_i , in %, where *i* indexes ecophysiotype) under Triassic warming and O_2 loss. Colored contours are for ecophysiotypes with $\Phi^{crit} = 3$. Measured values of $1/A_o$ and E_o in modern species are shown as black symbols. The grey polygon indicates trait combinations for which no habitat is available in the Permian simulation.

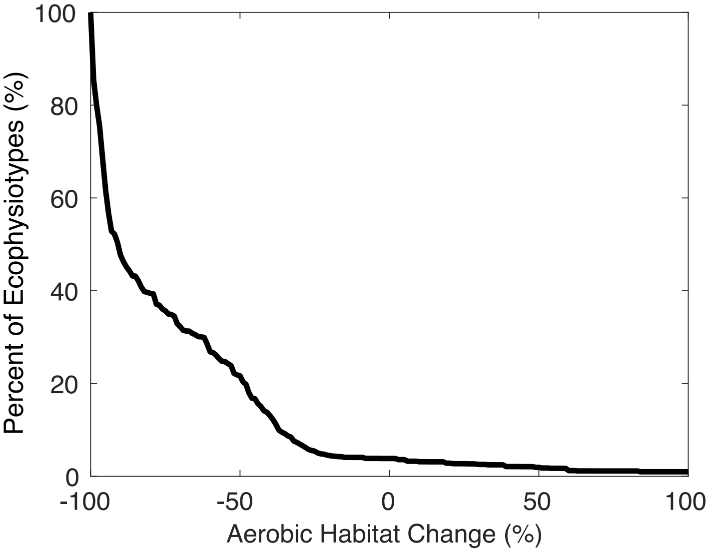

Figure 4.12. Percent of ecophysiotypes with aerobic habitat changes (%) exceeding a given value. Percent changes in aerobic habitat volume (ΔV_i, *i* denotes ecophysiotype) are calculated for the upper 1000 m. For the rare ecophysiotypes (~5%) whose Φ increases with temperature (i.e. $E_o < 0$ eV), their habitat volumes actually expand in response to warming (positive aerobic habitat change).

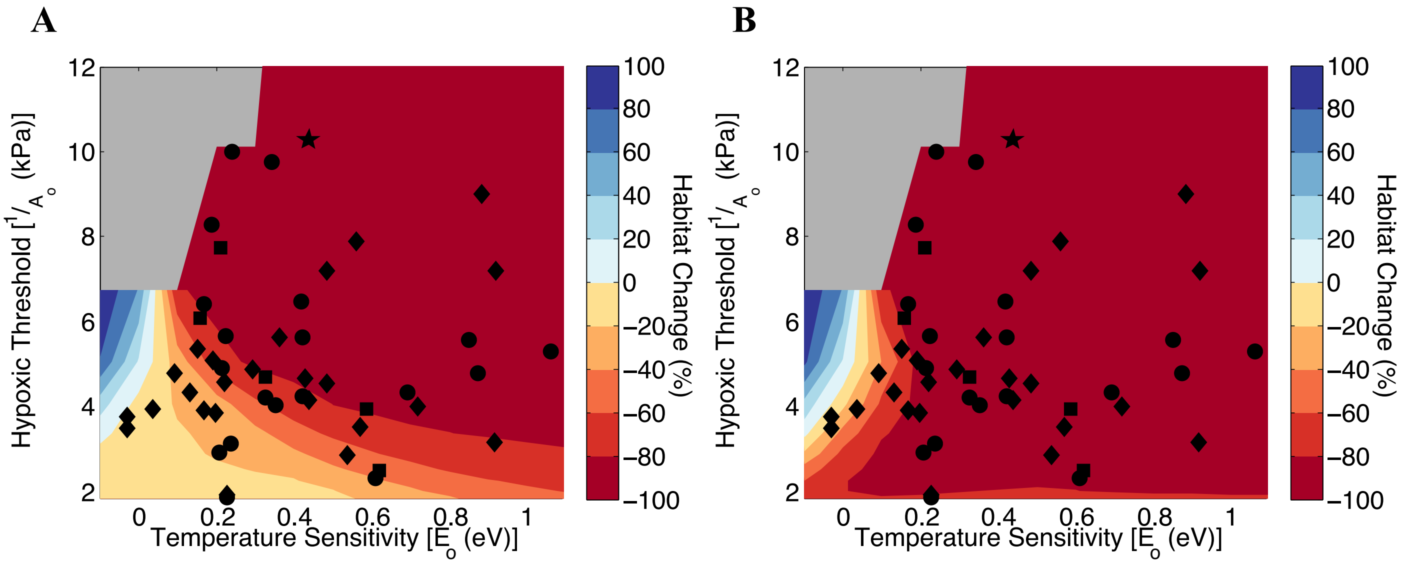

Figure 4.13. Sensitivity of aerobic habitat changes to depth. Same as in Figure 4.3B of the main text, but for aerobic habitat above 500 m (**A**) and above 4000 m (**B**). The patterns of differential habitat loss are qualitatively similar for each maximum depth interval, but the mean magnitude of habitat loss increases with depth.

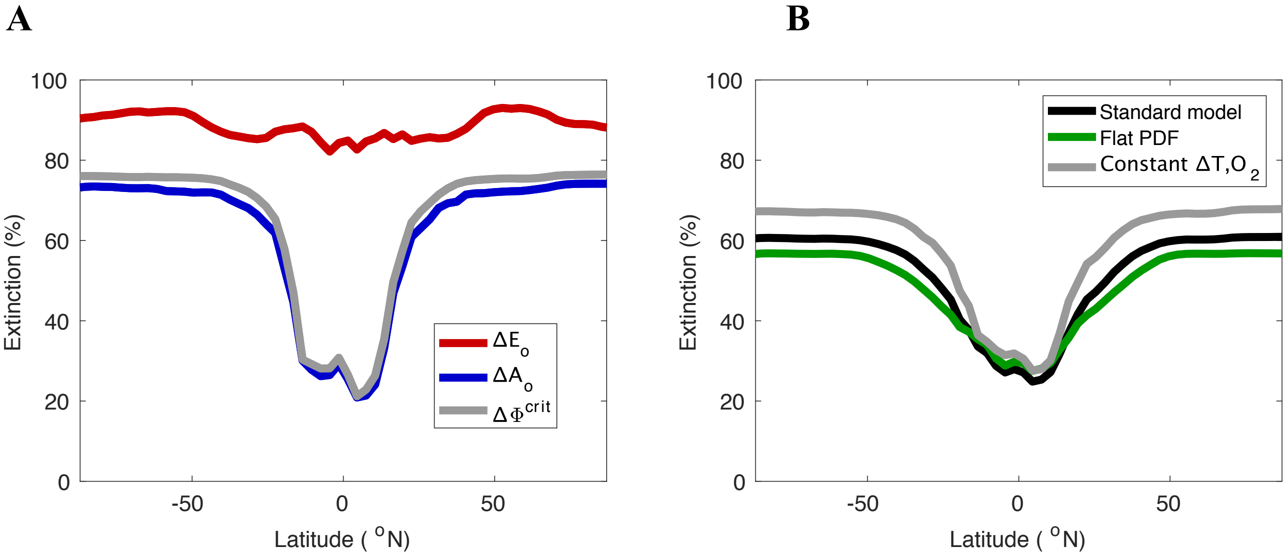

Figure 4.14. Mechanism of the simulated latitudinal pattern of global extinction. (**A**) Role of physiological and ecological traits. Simulated extinction is computed by varying a single trait across ecophysiotypes, while assigning the average values for remaining traits to all ecophysiotypes. Variations in either A_o or Φ^{crit} alone generate increased extinction outside of the tropics. In contrast, variations in E_o alone produce a relatively constant extinction across latitude. Model values are averaged across longitude and above 500 m, and use a maximum habitat depth of 1000 m and V^{crit} = 80%. (**B**) Role of the spatial patterns of global warming and O_2 loss and trait PDFs. Extinction is computed as in the main text (black), as well as with uniform anomalies (grey) of O_2 (ΔO_2 = -140 µM) and temperature (ΔT = 11°C), computed as the global mean difference between the Triassic and Permian simulations. The uniform anomalies are added everywhere to the Permian O_2 and temperature fields to compute global extinction in the Triassic. Extinction patterns and magnitudes are primarily unchanged relative to the case with spatially varying patterns of deoxygenation and warming (i.e. the standard model). A third experiment was conducted to test the role of ecophysiotype weighting (green). Extinction is computed as in the main text, but here equal weighting for all ecophysiotypes is assumed (i.e. a flat PDF for each trait, w_i = 1). The patterns and magnitudes of extinction are only weakly affected by the changed weighting, and thus do not rest on the precise shape of the trait PDFs.

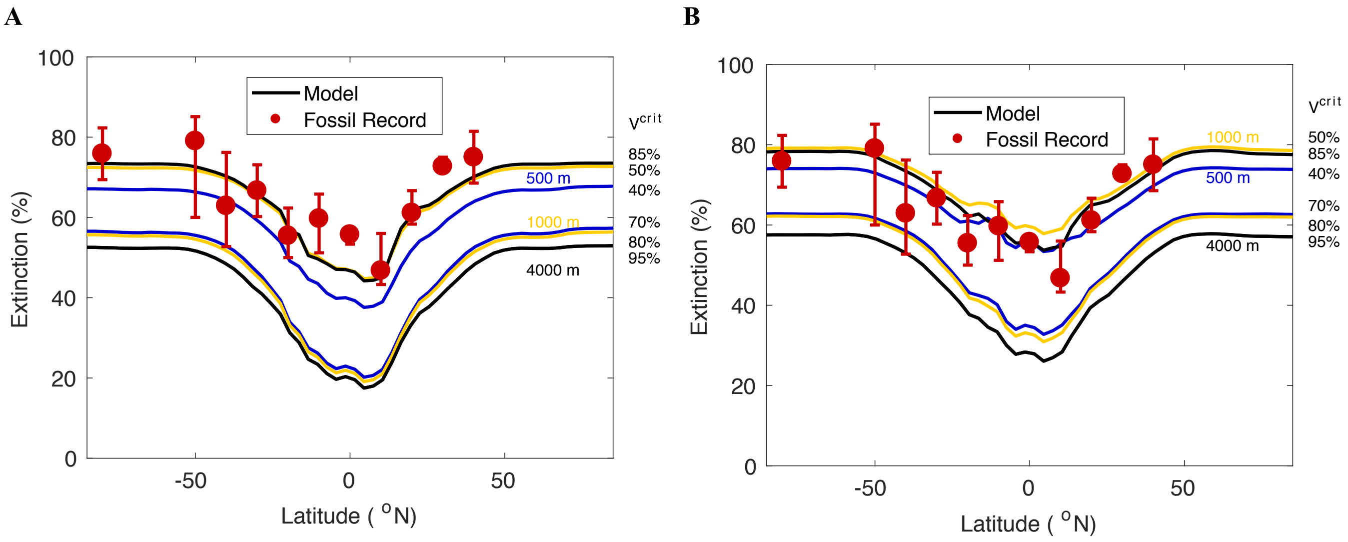

Figure 4.15. Sensitivity test of the model extinction gradient to expanded parameter ranges. Same as in Figure 4.4A of the main text, but assuming a 50% increase in the range and standard deviation of the (**A**) A_o and (**B**) E_o trait distributions. The overall latitudinal gradient of extinction is robust to whether Permian ecophysiotypes had traits outside the range of the modern distributions.

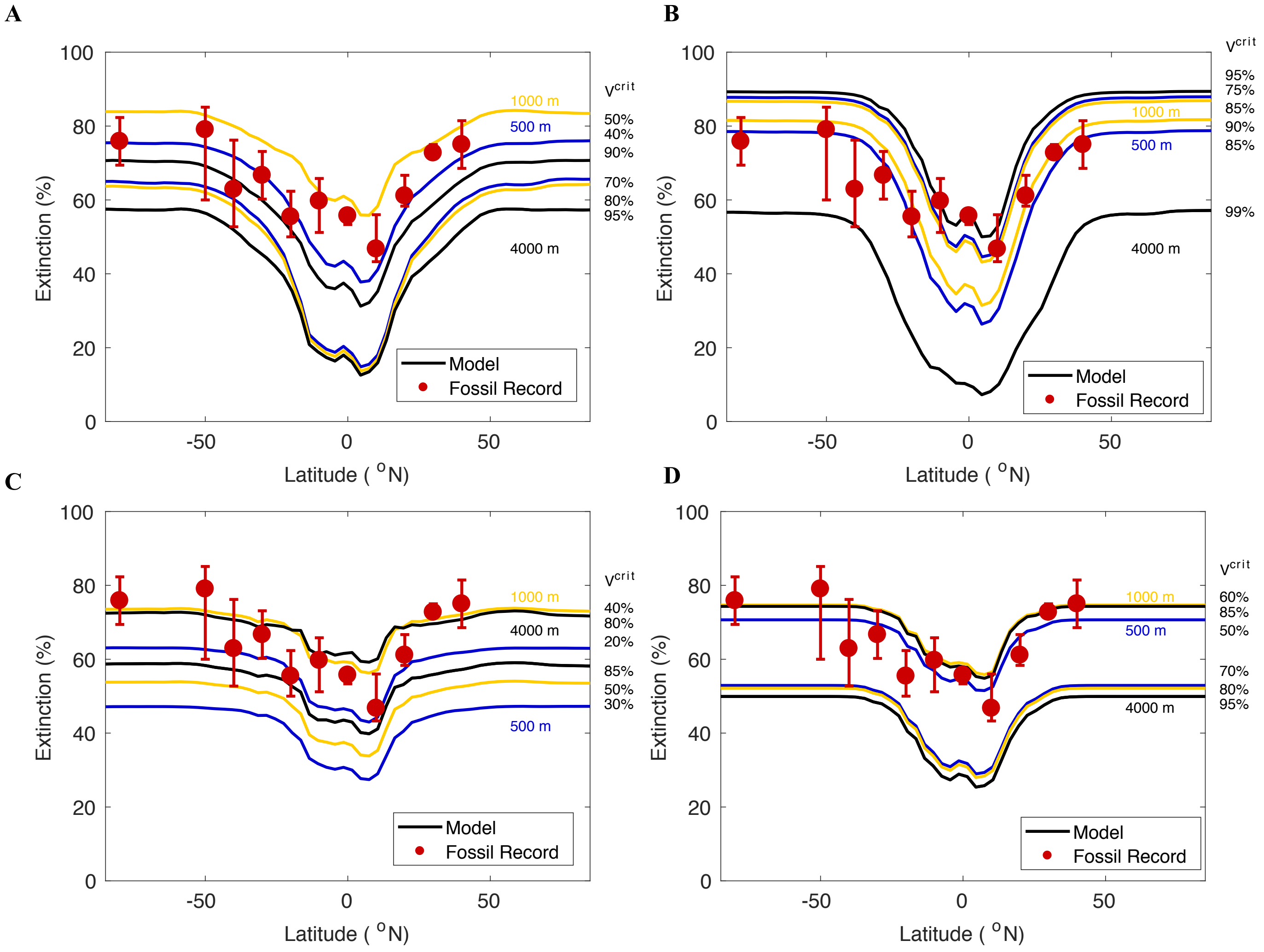

Figure 4.16. Sensitivity test of the model extinction gradient to narrowed parameter ranges. Same as in Figure 4.4A of the main text, but restricting Permian ecophysiotype E_o and A_o to different quadrants of modern trait space. Quadrants are defined by splitting each trait range in half. (A) quadrant 1: low E_o and A_o, (B) quadrant 2: high E_o and low A_o, (C) quadrant 3: low E_o and high A_o, and (D) quadrant 4: high E_o and A_o. The value of the critical habitat loss threshold (V^{crit}) is varied to infer similar magnitudes of extinction to Fig. 4.4A. While the precise latitudinal trend varies across parameter space, the general trend – increased extinction away from the tropics – is found for all quadrants of parameter space.

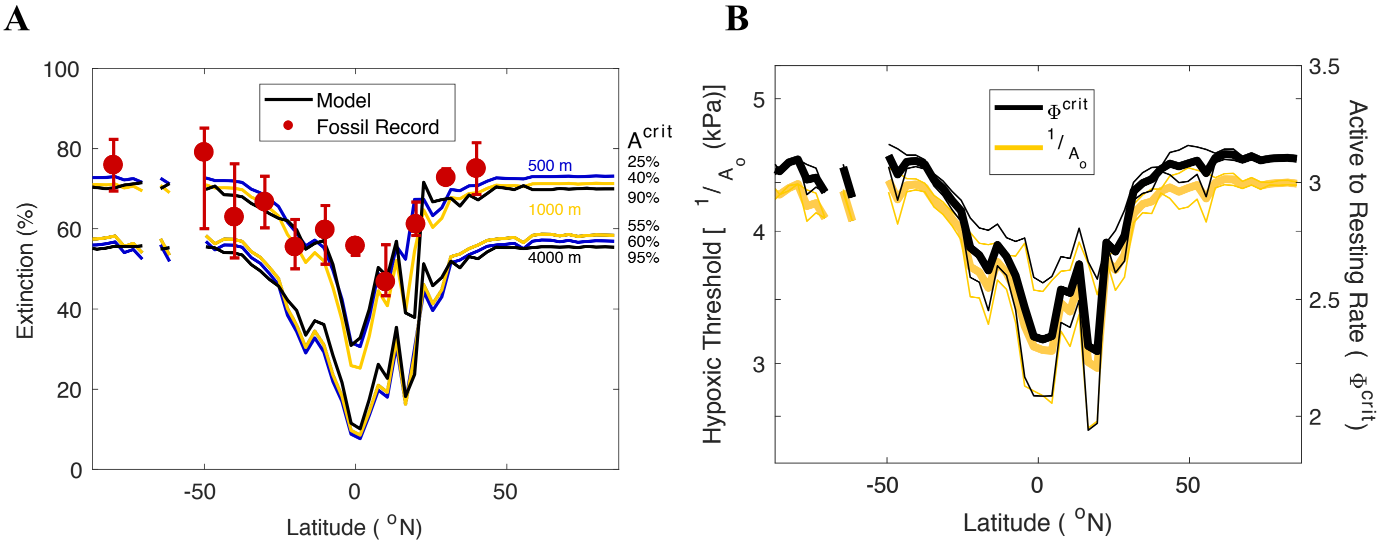

Figure 4.17. End-Permian global extinction in coastal seafloor regions. (**A**) Global extinction is calculated in the same way as in the main text, but from the simulated changes in Permian global aerobic habitat area (ΔA_i) at the seafloor under Triassic warming and O_2 loss. The fractional loss of Permian habitat area leading to extinction, A^{crit}, and the maximum depth of aerobic habitat are varied from 25 - 95% (right axis labels) and 500 m - 4000 m (colors), respectively, and influence the mean extinction, but not its latitudinal pattern. (**B**) Average hypoxic threshold and ratio of active to resting metabolic rate across ecophysiotypes versus latitude in coastal seafloor regions of the Permian. Shading represents the 1σ standard deviation at each latitude. Predicted extinction magnitudes and traits are averaged over longitude and above 500 m in near-shore regions. The main latitudinal patterns of extinction and hypoxia traits are robust to whether extinction is computed at the seafloor using area (ΔA_i) or across the water-column using ocean volume (ΔV_i; Figure 4.4A). However, seafloor patterns are noisy because of the poorly resolved Earth System Model bathymetry.

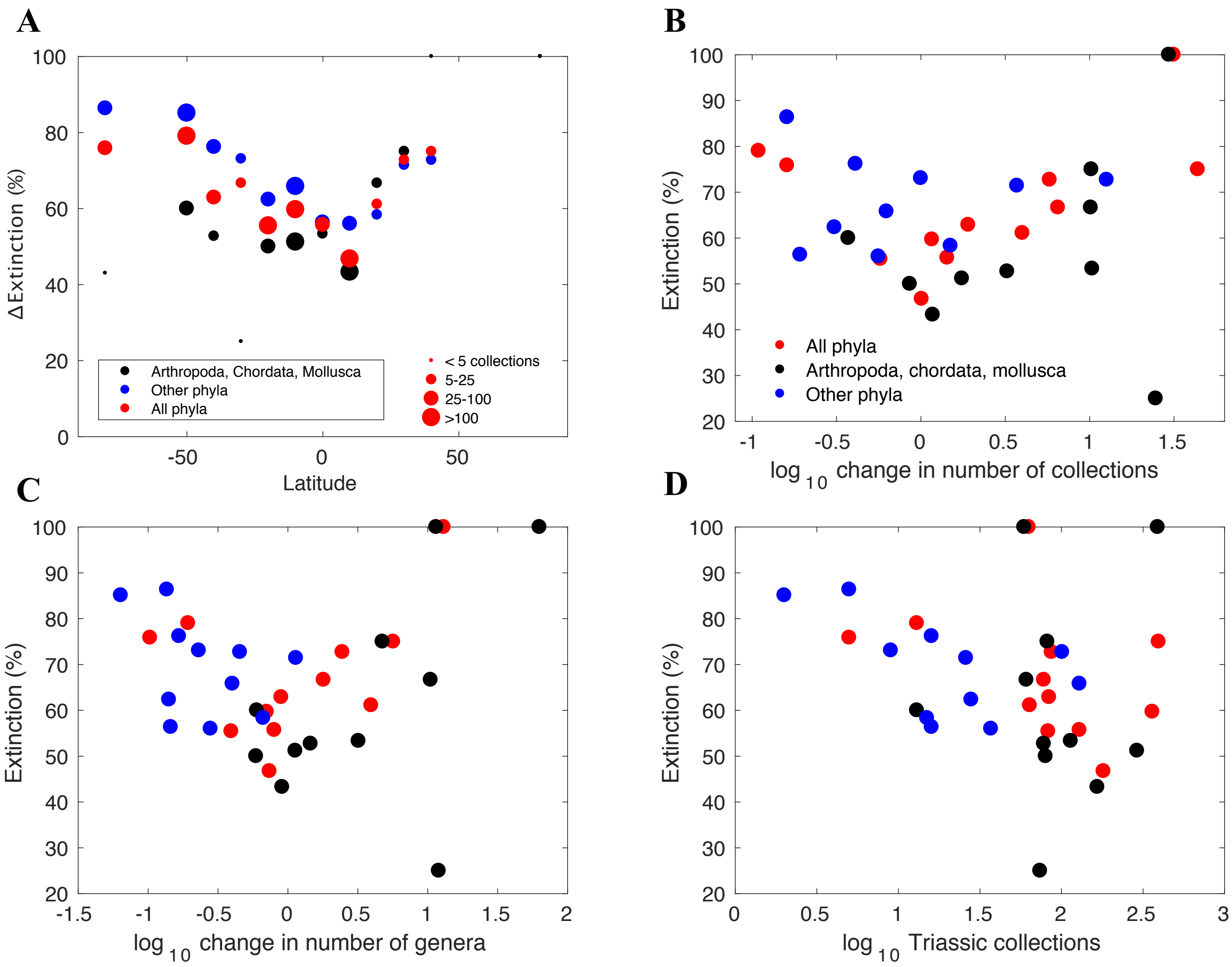

Figure 4.18. Latitudinal extinction pattern of end-Permian genera by taxonomic grouping and versus sampling intensity. (**A**) Extinction (%) is calculated as in Figure 4.4A of the main text, but here is also restricted to specific taxonomic groupings, including arthropods, chordates and mollusks together (black), all other phyla (blue), and all phyla together (red). Symbol size is scaled by the number of Permian fossil collections. The main latitudinal trend – increased extinction away from the tropics – is found for all groupings when including all data together or when restricting to the best-sampled latitude bands. (**B**-**D**) Extinction (%) versus metrics of sampling intensity by latitude band. (**B**) Extinction (%) versus $\log_{10}$ of the ratio of early-Triassic to end-Permian fossil collections. (**C**) Extinction versus $\log_{10}$ of the ratio of early-Triassic to end-Permian genera. (**D**) Extinction (%) versus $\log_{10}$ of early-Triassic fossil collections. There are no significant correlations between extinction (%) and any metric of sampling intensity.

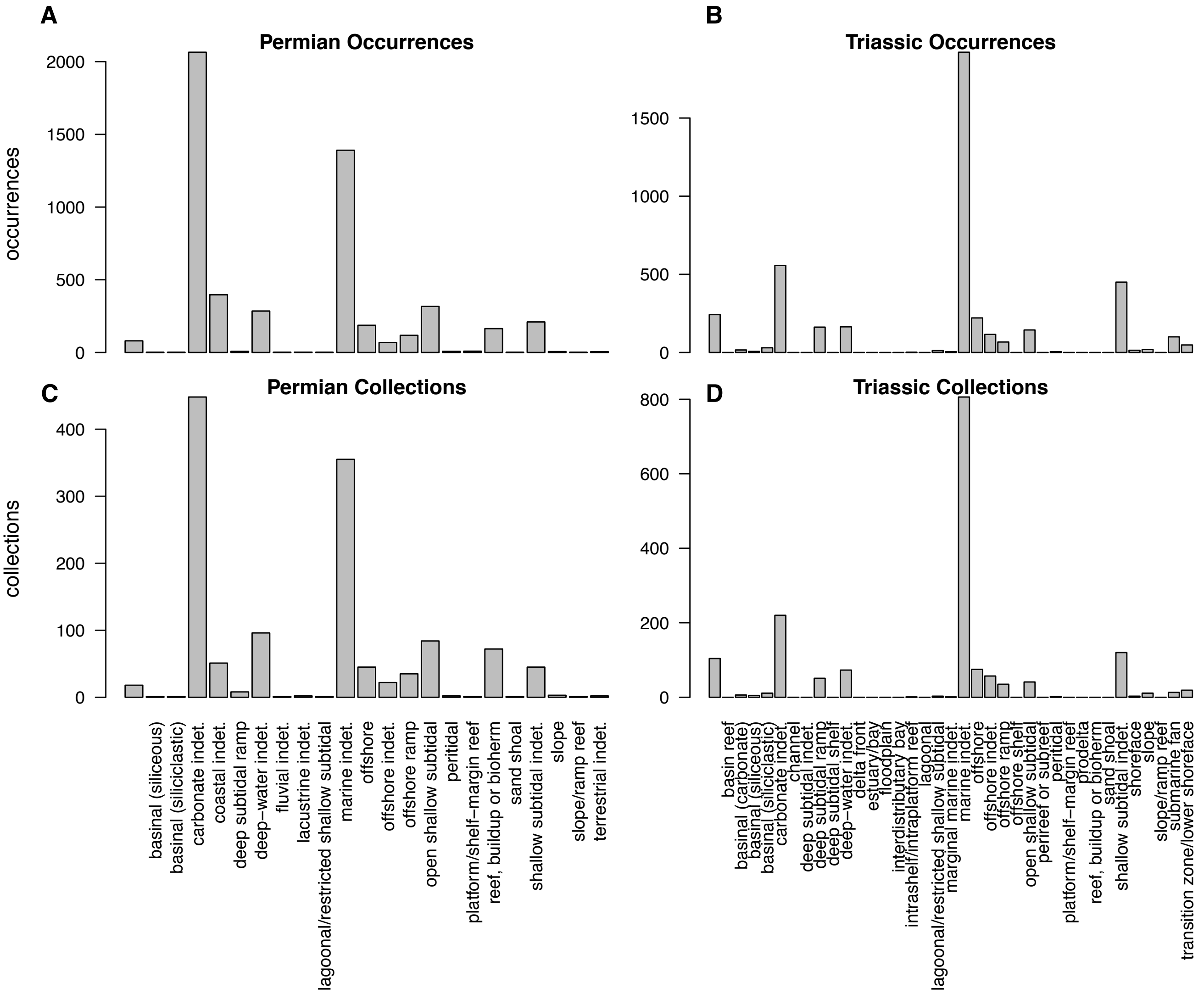

Figure 4.19. Depositional environments of end-Permian and early-Triassic fossil occurrences and fossil collections. (**A** and **B**) Fossil occurrences from the end-Permian and early-Triassic. (**C** and **D**) Fossil collections from the end-Permian and early-Triassic.

4.11 Tables

Table 4.1. Parameters for the Metabolic Index. E_o and A_o measurements derived by least-square regression of published pO_2^{crit} versus temperature data. Phyla are listed in parantheses: Arthropoda (A), Chordata (Ch), Cnidaria (Cn), Mollusca (M). Where both O_2^{hypox} and O_2^{LC50} data are available, trait estimates based on O_2^{LC50} are provided in parantheses. Φ^{crit} values from percentile and change point methods are listed in that order. If both methods yield the same estimate a single value is given. Data used to estimate Φ^{crit} are available at http://www.iobis.org/.

Species (Phylum)	**# Data**	**E_o (eV)**	**A_o (atm^{-1})**	**Φ^{crit}**
Acanthephyra acutifrons (A)	2	-0.03	26.8	
Acanthephyra curtirostris (A)	2	0.04	25.6	
Acanthephyra purpurea (A)	2	0.13	23.3	2.6 – 3.1
Acanthephyra smithi (A)	3	-0.03	29.0	
Acipenser brevirostrum (Ch)	6	0.42	23.9	
Anguilla japonica (Ch)	2	0.13	7.9	
Bellapiscis lesleyae (Ch)	3	0.42	18.0	
Bellapiscis medius (Ch)	3	0.61	43.6	
Bythograea thermydron (A)	3	0.23	52.8	
Callinectes sapidus (A)	3	0.54	35.5	3.8
Cancer irroratus (A)	50	0.92	32.1	6.5 – 6.0
Carcinus maenas (A)	3	0.48	22.3	
Chromis atripectoralis (Ch)	4	0.50	73.2	
Crassostrea gigas (M)	3	0.21	13.1	
Cyclopterus lumpus (Ch)	2	0.19	12.2	2.5 – 3
Dentex dentex (Ch)	8 (8)	0.17 (0.21)	15.8 (34.8)	
Diplodus Puntazzo (Ch)	9	0.23	53.9	4.2
Dosidicus gigas (M)	2	0.62	40.8	
Funchalia villosa (A)	2	0.17	25.9	3.2 – 3.6
Gadus morhua (Ch)	3 (6)	0.42 (0.87)	15.6 (21.2)	2.1 – 2.2 (4.3 – 4.0)
Gadus ogac (Ch)	2	0.29	6.5	2.1
Gammarus pseudolimnaeus (A)	27	0.72	25.3	
Gaussia princeps (A)	3	-0.13	83.4	
Gennadas valens (A)	2	0.20	26.4	3.5 – 4.0
Gibberulus gibbosus (M)	2	0.41	85.6	
Gobiodon erythrospilus (Ch)	4	0.67	66.0	
Gobiodon histrio (Ch)	4	0.93	123.0	
Lophelia pertusa (Cn)	2	0.44	9.9	1.4 – 1.3
Melanostigma pammelas (Ch)	4	1.06	19.1	

Morone saxatilis (Ch)	2	0.33	24.0	5.0 – 4.8
Mytilus species (M)	3	0.16	16.7	
Nautilus pompillius (M)	3	0.59	25.7	
Notostomus gibbosus (A)	2	0.92	14.1	
Notostomus elegans (A)	2	0.44	24.4	
Oplophorus gracilirostris (A)	5	0.09	21.1	
Oplophorus spinosus (A)	3	0.29	20.8	2.3 – 2.2
Palaemonetes pugio (A)	2	1.35	144.8	
Palaemonetes vulgaris (A)	3	0.62	56.3	
Pandalus borealis (A)	4	0.88	11.3	4.7 – 4.8
Pandalus platyceros (A)	2	0.15	18.9	1.8 – 1.7
Panulirus Cygnus (A)	3	0.19	19.9	
Panulirus interruptus (A)	2	0.57	28.9	
Paralichthys dentatus (Ch)	2	0.35	25.1	3.5 – 3.6
Pecten maximus (M)	3	0.33	21.6	5.4 – 5.5
Penaeus aztecus (A)	2	0.22	9.6	1.5 – 1.6
Penaeus vannamei (A)	7	0.09	59.4	
Salmo salar (Ch)	4	0.34	10.4	
Sciaenops ocellatus (Ch)	2	0.24	32.3	5.0 – 5.1
Scyliorhinus canicula (Ch)	3	0.24	10.1	2.2
Sepia officinalis (M)	2	0.72	60	3.4 – 3.2
Sergestes bisulcatus (A)	3	0.49	14.1	
Sergestes fulgens (A)	3	0.56	12.8	
Sergestes tenuiremis (A)	3	0.36	18.0	
Sergia grandis (A)	2	0.43	21.7	
Stenobrachius leucopsarus (Ch)	2	0.69	23.4	2.2 – 4.4
Styela plicata (Ch)	4	-0.09	6.3	1.4 – 1.3
Systellaspis debilis (A)	6	0.22	22.2	2.4 – 2.5
Tarletonbeania crenularis (Ch)	2	0.21	20.6	2.6 – 4.8
Tautogolabrus adspersus (Ch)	2	0.22	17.9	4.0 – 3.8
Tigriopus brevicornis (A)	2	0.44	114.3	
Zoarces Viviparus (Ch)	6	0.85	18.2	4.4 – 3.6

Table 4.2. Fossil record data by latitude from the Paleobiology Database. Data include the number of genera and fossil collections from the latest Permian (Changhsingian) and earliest Triassic (Induan), as well as the number and percentage of extinct and extirpated genera for three different taxonomic groupings.

Latitude (°N)	Changhsingian Genera	Induan Genera	Changhsingian Collections	Induan Collections	Extinct Genera	Extinction (%)	Extirpated Genera	Extirpation (%)
All phyla								
-80	29	3	31	5	22	75.9	29	100
-50	62	12	119	13	49	79	61	98.4
-40	97	87	44	84	61	62.9	93	95.9
-30	30	54	12	78	20	66.7	27	90
-20	193	76	144	83	107	55.4	172	89.1
-10	201	142	310	361	120	59.7	152	75.6
0	70	56	90	129	39	55.7	65	92.9
10	92	68	179	181	43	46.7	71	77.2
20	18	71	16	64	11	61.1	18	100
30	11	27	15	87	8	72.7	11	100
40	12	68	9	394	9	75	12	100
80	2	26	2	63	2	100	2	100
Arthropods, Chordates and Mollusks								
-80	7	0	3	0	3	42.9	N/A	N/A
-50	15	9	35	13	9	60	15	100
-40	55	80	24	78	29	52.7	51	92.7
-30	4	48	3	74	1	25	4	100
-20	108	64	93	80	54	50	92	85.2
-10	84	95	166	291	43	51.2	63	75
0	15	48	11	114	8	53.3	14	93.3
10	67	61	141	166	29	43.3	47	70.2
20	6	63	6	61	4	66.7	6	100
30	4	19	8	82	3	75	4	100
40	1	63	1	389	1	100	1	100
80	2	23	2	59	2	100	2	100
Other Phyla								
-80	22	3	31	5	19	86.4	22	100
-50	47	3	105	2	40	85.1	47	100
-40	42	7	39	16	32	76.2	42	100
-30	26	6	9	9	19	73.1	23	88.5
-20	85	12	91	28	53	62.4	80	94.2
-10	117	47	206	129	77	65.8	90	76.9
0	55	8	83	16	31	56.4	51	92.7
10	25	7	66	37	14	56	24	96
20	12	8	10	15	7	58.3	12	100
30	7	8	7	26	5	71.4	7	100
40	11	5	8	101	8	72.7	11	100

Table 4.3. Probability density functions (PDF) of physiological and ecological traits. PDFs are determined from the average and standard deviations of the trait distributions in modern organisms (Figure 4.9B-D). The PDF of E_o is described using a normal distribution. The PDFs of both A_o and Φ^{crit} are described using log-normal distributions. Constants c_E, c_A, and c_C are chosen to normalize the total number of ecophysiotypes in each trait PDF to 1.

Trait	**Probability Density Function**	**Constants**
Temperature sensitivity E_o	$w_i^E = \frac{1}{c_E\sqrt{2\pi\sigma_E^2}}\exp[\frac{-(E_o-\mu_E)^2}{2\sigma_E^2}]$	μ_E = 0.41 eV σ_E = 0.29 eV c_E = 1.40
Inverse of Hypoxic Threshold A_o	$w_i^A = \frac{1}{A_o c_A\sqrt{2\pi\sigma_A^2}}\exp[\frac{-(\ln A_o-\mu_A)^2}{2\sigma_A^2}]$	μ_A = 3.01 σ_A = 0.49 c_A = 0.05
Active to resting metabolic rate Φ^{crit}	$w_i^C = \frac{1}{\Phi^{crit} c_C\sqrt{2\pi\sigma_C^2}}\exp[\frac{-(\ln\Phi^{crit}-\mu_C)^2}{2\sigma_C^2}]$	μ_C = 1.10 σ_C = 0.42 c_C = 0.35

Chapter 5

Marine extinction risk from climate warming

5.1 Abstract[4]

Global warming threatens marine biota with losses of unknown severity. Here we quantify global and regional extinction risks in the ocean across a range of climate futures, based on diverse species' ecophysiological limits, and calibrated against the fossil record. Under accelerating future greenhouse gas emissions, species losses from warming and oxygen depletion are projected to surpass current direct human impacts on biodiversity within a century, en route to a mass extinction rivaling those in Earth history, by 2300 CE. Gravest regional risks overlap the world's most productive ecosystems and fisheries. "Flattening the curve" of global greenhouse gas emissions would diminish extinction risks by over 70%, protecting marine biodiversity and the numerous local efforts to conserve it.

---

[4] An edited version of this chapter is in preparation as Penn, J.L. and Deutsch, C. (in review), Marine extinction risk from climate warming.

5.2 Introduction

Human activities are altering global climate, physically transforming habitat, and overexploiting species on land and in the oceans (*168*, *169*). As a result, extinction rates have risen above natural background levels (*38*, *170*). Documented extinctions are largely confined to land, where direct human impacts began earlier and remain more pervasive, despite rapid growth in commercial fishing, marine pollution, and transport (*171*). However, climate change may eventually eclipse direct local human impacts, by causing widespread habitat loss via changes in the thermal and chemical conditions that reach even the most remote biomes on Earth, including the deep and open ocean (*9*, *11*). The emerging impact of climate change on global biodiversity is likely to be profound, but difficult to observe, especially for those perpetually under-sampled marine environments. Model projections of extinction risk from climate change can overcome current data limitations by synthesizing species ecophysiology, climate dynamics, and the mass extinction patterns in Earth history.

The capacity for dramatic loss of biodiversity driven by environmental change is illustrated by the five major mass extinctions in the fossil record (*38*). While their causes are uncertain and variable, they provide possible analogues for a potential "sixth mass extinction", and empirical benchmarks against which to evaluate its ultimate severity (*38*, *172*). The largest of these, the "Great Dying" at the end of the Permian Period (~252 million years ago), also shares striking similarities with large-scale environmental changes that are accelerating in the Anthropocene – rising temperatures, and declining dissolved oxygen (O_2) levels (Figure 5.1), productivity, and pH (*11*, *39*, *42*, *44*, *113*, *115*). Two of these factors – temperature and O_2 – have been shown to account for modern animal range limits (*27*, *28*, *35*) and the biogeography and severity of the end-Permian extinction (Chapter 4).

5.3 Methods

Here we project global and regional extinction risks to marine animals under climate change for the coming centuries by applying an ecophysiolocial model of species aerobic habitat availability, which was used to reproduce aspects of the end-Permian extinction (Chapter 4), to an ensemble of Earth System Models (ESMs) forced by historical emissions and future greenhouse gas scenarios (Section 5.7 Supplemental Methods). Extinction risks (% of species lost) are computed based on species' ecophysiological aerobic habitat limits defined by a combination of empirically derived traits sampled from modern taxonomic diversity (Chapter 4 and *28*), and by changing climate conditions projected by ESMs from the Coupled Model Intercomparison Project (CMIP) phases 5 and 6 (inset Figure 5.2A; Table 5.1; *9*, *11*, *173*). For ocean waters to be habitable for a given species, the local temperature must exceed a species-specific minimum (*174*), and local O_2 must be able to supply the temperature-dependent metabolic demand in a ratio (Φ) that meets or exceeds a threshold value (Φ^{crit}) required for maintenance, growth, and ecological activity (*27*, *28*). Wherever ocean warming and O_2 loss drive this O_2 supply to demand ratio below a species' critical threshold, aerobic habitat is lost, leading to regional extinction (extirpation) (Chapter 4, Section 5.7 Supplemental Methods; *35*, *175*, *176*). Global extinction occurs if total habitat loss exceeds a critical level, calibrated by the end-Permian extinction (Chapter 4, Section 5.7 Supplemental Methods), beyond which a viable population can no longer be sustained (e.g., *177*).

We evaluated extinction risks in two future climate change scenarios that span the widest plausible range in the trajectory of greenhouse gas emissions (inset Figure 5.2A). In the 'high emissions scenario' (the Shared Socioeconomic Pathway (SSP) 5-8.5), emissions accelerate with minimal constraints and yield a radiative forcing of 8.5 W/m^2 in 2100, while under 'low emissions' (SSP1-2.6), dramatic climate change mitigation is immediate (starting in 2020) and reduces end of the century radiative imbalances to 2.6 W/m^2. We also evaluated divergent biological scenarios that span an extreme range in rates of species dispersal into new habitat. In the first, species are restricted to their native ranges and can only lose habitat under warming ('No dispersal' lines; Figure 5.2A). In the second, habitat loss can be compensated for by instantaneous dispersal to waters outside of species' native ranges wherever temperatures rise above minimum physiological tolerances (*174*)('Dispersal' lines; Figure 5.2A). In reality, marine species likely fall between these scenarios, because dispersal to new habitat (by active swimming or passive advection) is not instantaneous, and population establishment might not be possible due to specific life-history or ecological requirements apart from aerobic and thermal habitat constraints.

5.4 Results

As anthropogenic climate change accelerates, so too do projected species losses. The rate of these losses over time depends strongly on the emissions scenario, which governs the rate of ocean warming (Figure 5.3). By the latter half of this century, the climate trajectories markedly diverge between scenarios, leading to growing disparities in extinction risk. However, for a given magnitude of accumulated heat in the upper ocean, extinction risk is largely similar between the two scenarios (Figures 5.2, 5.4). The small differences that arise do so because under slower warming slightly less O_2 is lost per degree, preserving more aerobic habitat globally (Figure 5.5).

The eventual magnitude of extinction risk is largely determined by total ocean warming, and thus the extent of future emissions (Figure 5.2). With a 'low emissions scenario', global temperature stabilizes by the end of the century (~ 0.7 – 1.2 ^{o}C of warming in the upper 500 m), and extinction risk increases only modestly beyond present-day levels. On the other hand, under a 'high emissions scenario', risks grow dramatically beyond 2100 CE. By 2300 CE, the upper ocean warms by ~5 – 11^{o}C, elevating extinction risks to approach the levels predicted in simulations of the end-Permian, and with a similar biogeographic pattern of selectivity: greater global extinction at higher latitudes and greater extirpation in mid to low latitudes (Figures 5.6, 5.7) (Chapter 4). Global extinction risk is also higher for non-dispersing species (Figure 5.2A). Dispersal into new regions at species' cold-edge range boundaries initially delays global extinction under low warming magnitudes, by partially compensating for aerobic habitat loss, but eventually ceases to maintain habitat as warming intensifies.

Our projections indicate that climate change will emerge as an increasingly dominant threat for marine species. To compare future warming to current anthropogenic stressors, we estimated modern extinction risks in the oceans using vulnerability assessments made by the International Union for Conservation of Nature (IUCN) (*178*) for 10,025 species globally and for 2,253 species in 10 marine regions (*Section 5.7 Supplemental Methods*). Between 9 to 14% of marine species would be driven to extinction if all taxa currently listed as 'near-threatened' or 'threatened' are eventually lost (Figure 5.2A; Table 5.2). Similarly, 11-16% of species are at risk of being extirpated on average across marine regions (Figure 5.2B; Table 5.3). Climate change currently affects ~45% of these ‘at risk’ species, and is the fifth largest stressor in the ocean overall, falling behind overfishing, transportation, urban development, and pollution (Figure 5.8). Relative to all assessed marine species, including those not at risk, climate change currently threatens just 4-6% of species in total (Table 5.2).

Under future warming, however, extinction risks from climate change lay along a trajectory that would surpass all modern anthropogenic threats combined (Figure 5.2). Under a ‘high emissions scenario’, this benchmark is met or surpassed by the end of the century for global extinction of non-dispersing taxa, while for dispersers it’s approached or exceeded by ~2300 CE (Figure 5.2A). Future extirpations from warming also meet or exceed modern threats by 2100 CE, reaching 2-6 times those levels two centuries later (Figure 5.2B). In contrast, under rapid emissions reductions, extinction risks are generally maintained at or below the severity of modern threat levels from all human perturbations. To the extent that climate and other anthropogenic extinction threats apply to separate species (*169*), future extinction risks in the ocean would be higher than from either factor alone.

Eventually, under a ‘high emissions scenario’, global extinction risks from warming rival the severity of past mass extinctions in Earth history (Figure 5.2A). By 2300 CE, extinctions of non-dispersers reach the intensity of the top four most severe marine extinctions: during the end-Triassic, end-Cretaceous, Late Ordovician and end-Permian. Even for dispersers, extinction risks could exceed all but the ‘Great Dying’. Limiting greenhouse gas emissions would cut the severity of a marine mass extinction due to anthropogenic warming by over 70%.

Beyond imperiling biodiversity, climate change is a growing threat to global fishing, which supplies almost 20% of dietary protein for humans (*179*). We compared the geography of marine species catch over the past ~65 years (*180*) to extirpations from aerobic habitat loss at the century’s end under the ‘high emissions scenario’ (Figue 5.9A). On global scales, both show a similar geographic pattern: highest catch rates occur in the mid to low latitudes where extirpations are also strongest (Figure 5.9A,B). Within these latitudes, hotspots of extirpation center on highly productive ecosystems where background O_2 supply to demand ratios (Φ) are already low and/or climate anomalies are particularly intense: the north Pacific, eastern boundary upwelling systems and equatorial regions of Indo-Pacific (Figure 5.9A). As warming and O_2 loss progress beyond 2100 to 2300 CE, over 50% of taxa are extirpated in the tropics and northern mid latitudes (Figure 5.9B). Including in these extirpation projections taxa that are also at risk of global extinction would further exacerbate losses, particularly at higher latitudes (Figure 5.6; Chapter 4).

Strong climate change mitigation policies would yield a similar long-term biogeographic pattern of extirpation risk as the 'high emissions scenario', but limit its intensity to near present-day levels (Figure 5.9B). Indeed, regional exclusion is predicted to have already occurred in the low to mid latitudes (black line, Figure 5.9B), potentially underlying well-documented local species losses from range contractions attributed to warming and/or O_2 loss in these areas (black points, Figure 5.9A; Figure 5.10) (*35*, *174*).

5.5 Discussion

Warming and declining O_2 levels are expected to be accompanied by additional biogeochemical changes and ecological dynamics that could amplify extinction risk even further, including through ocean acidification, hypercapnia, productivity declines, and higher-level food web dynamics (*11*, *177*, *181–183*). Moreover, anthropogenic threats unrelated to climate are likely to increase due to human population growth (*171*), further raising total extinction risk in the oceans. Limiting warming is critical to ensure current conservation investments protecting species from non-climate related stressors remain successful in the coming decades and centuries.

Future marine extinction risks from climate warming will be strongly influenced by policies to control greenhouse gas emissions (inset Figure 5.2A). While past emissions have followed an accelerating trajectory that continues under the 'high emissions scenario', achieving the critical reductions to curtail extinctions is not too late; the 'low emissions' scenario assumes emissions begin declining this year and continue hereafter. Any further delay in flattening the emissions curve will need to be compensated by more dramatic, and thus harder to achieve, reductions to fully avoid a worst-case scenario for animal life in the oceans.

5.6 Acknowledgements

We gratefully acknowledge insightful discussions with and input from K. Armour, the technical support of H. Frenzel, and contributors to OBIS and the Sea Around Us, including data acquisition assistance from G. Tsui. This work was supported by grants from National Science Foundation (OCE-1737282), the Gordon and Betty Moore Foundation (GBMF#3775), the National Oceanic and Atmospheric Administration (NA18NOS4780167), California SeaGrant and Ocean Protection Council. JP was supported by a graduate student fellowship from the Program on Climate Change at the University of Washington.

5.7 Supplemental methods

5.7.1 Climate data

We analyzed projections of future climate states under divergent greenhouse gas emissions scenarios from an ensemble of 12 different Earth System Models (ESMs) participating in the Climate Model Intercomparison Project (CMIP phases 5 and 6) (Table 5.1) (*9*, *11*, *184*). Climate models are forced by historical greenhouse gas emissions until the early 21st century and then by two divergent future emissions scenarios: 1) the 'high emissions scenario', in which emissions accelerate throughout the 21st century and reach a nominal radiative forcing of 8.5 W/m^2 in 2100, corresponding to the Shared Socioeconomic Pathway (SSP) 5-8.5 for CMIP6 and Representative Concentration Pathway (RCP) 8.5 for CMIP5, and 2) the 'low emissions scenario', in which emissions peak by the year 2020, decrease thereafter, and reach a nominal radiative forcing of 2.6 W/m^2 in 2100, which corresponds to SSP1-2.6 and RCP-2.6 (*173*). CO_2 emissions projections from the SSPs are qualitatively similar to those based on the RCPs. For simplicity, we plot the newer SSP projections in the inset of Figure 5.2A (data downloaded from https://tntcat.iiasa.ac.at/SspDb/dsd?Action=htmlpage&page=about). Nine ESMs were projected to the end of the 21st century, while four were run to the end of the 23rd century (Table 5.1). To avoid double counting ESMs that ran simulations for both CMIP5 and CMIP6, we only analyze output from the latter (newer generation) if available. For a single model (MPI), both CMIP generations were analyzed because the earlier CMIP5 simulation was projected further in the future than its CMIP6 counterpart.

Climate anomaly fields were computed by subtracting each model's pre-industrial fields (time-mean 1850-1900) from annual averages of the model fields under greenhouse gas forcing. To correct for potential model biases in the baseline spatial distributions of temperature and O_2, pre-industrial climate states were reconstructed from climatological observations of these tracers after removing the historical climate anomalies for each model from the observational period (time-mean 1955-2012) relative to the pre-industrial era. Climatological fields were analyzed at 1^o latitude and 1^o longitude over 33 depth levels from the World Ocean Atlas (*4*, *185*). All model fields were interpolated to the World Ocean Atlas grid for analysis.

Climate states under greenhouse gas forcing were analyzed for 2020 CE and from 2050 CE to the end of each model simulation in 50-year intervals, by adding ~30-year averages of annual climate anomalies around each corresponding time-period to the reconstructed pre-industrial climate state. For climate states at the end of each simulation, averages of both the last ~30 and ~10 years were analyzed. To account for uncertainty in future climate change projections across ESMs, the Metabolic Index (Φ) and corresponding extinction metrics were computed for each model individually.

The end-Permian climate and extinction scenarios analyzed here are described in Chapter 4, with the addition of cold edge habitat limits (described below).

5.7.2 Cold tolerance limits

To account for habitat constraints on marine species at cold edges of their range limits (*174*), cold tolerances of marine species (T^{cold}) were estimated by pairing geo-referenced occurrence data from OBIS with climatological fields of temperature (T) from WOA (Figure 5.11)(*186*). Species occurrences were paired to hydrographic data by binning to the WOA grid for every month based on the specimen locations provided in OBIS. Specimen depth was computed as the midpoint between the reported minimum and maximum depth, or from either depth alone if only one estimate was provided.

Species cold limits were estimated from the cumulative distribution function of inhabited temperature, as the temperature below which occurrences are rare (10th percentile of inhabited temperature). Cold limits were estimated for all species with over 100 geo-referenced occurrences in OBIS, yielding an estimate for 14,949 species. Estimated cold limits display a bimodal distribution that spans the entire range of ocean conditions (Figure 5.11). The overall distribution of this trait is insensitive to the minimum intra-species occurrence density threshold (varied from >10 to > 1000 occurrences) and to whether 5th or 10th percentile values are used to estimate T_{cold}.

5.7.3 Model extinction risk metrics

Here we briefly summarize the model metrics analyzed in this work. A detailed explanation, including mathematical notation, can be found in Chapter 4. We model a set of animal species types that vary in their Metabolic Index traits (E_o, A_o, Φ^{crit}) and cold limit trait (T^{cold}). The frequency of species with a given trait combination is established based on Probability Density Functions (PDFs) of Metabolic Index traits (Table 4.2) and the histogram of cold limits (Figure 5.11) that are each constructed independently from empirically-estimated distributions. We note that the distributions of Metabolic Index traits established in Chapter 4 are consistent with those from a recent dataset update, which increased the number of species with laboratory data (for E_o and A_o) from 61 to 72, and with biogeographic data (for Φ_{crit}) from 26 to 55 (now >1.5 million total occurrences) (*28*).

For each trait combination, we applied the Metabolic Index (Equation 4.1) to the reconstructed pre-industrial climate fields of temperature and O_2 and to the fields forced by anthropogenic greenhouse gas emissions. Model species were populated throughout the pre-industrial ocean in waters where aerobic and thermal habitat is available ($\Phi \geq \Phi^{crit}$ and $T \geq T^{cold}$). Regional extinction (extirpation) risk is computed in every model grid cell as the local fraction of pre-industrial species whose local Φ is driven below Φ^{crit} by warming and/or O_2 loss. To model global extinction, global habitat volumes (m^3) in the upper 500 m of the water-column were computed for each species in the pre-industrial climate state and under anthropogenic climate change. Global extinction risk is computed as the percent of pre-industrial species whose relative (%) loss of global habitat volume exceeds a critical threshold leading to extinction (V^{crit}). Global extinction risk metrics were computed both as a fraction of the entire global community (lines and circles Figures 5.2A, 5.3C,D, and 5.4A), and locally in every model grid cell (Figures 5.6, Figures 5.12, and vertical error bars in Figures 5.2A and 5.4A). Two global extinction scenarios were evaluated: 1) species that can instantaneously disperse to and inhabit previously unoccupied waters in the pre-industrial state wherever temperatures rise above minimum physiological tolerances (*174*) ('Dispersal' lines; Figure. 5.2A) and 2) species that can only inhabit waters previously occupied in the pre-industrial state ('No dispersal' lines; Figure 5.2A).

Estimated V^{crit} values are constrained by comparing the magnitudes of model extinction metrics for the end-Permian to reconstructions from the global marine fossil record, and assuming that aerobic habitat loss accounts for an equal fraction of observed global extinction as extirpation (Figure 5.12; Chapter 4). This constraint yields estimates of the critical habitat loss threshold parameter (V^{crit}) equal to 50% and 70% for 'Dispersal' and 'No dispersal' scenarios, respectively. We assume the same loss of habitat leading to global extinction (V^{crit}) in the Permian would lead to extinction in the modern ocean. These inferred V^{crit} values fall within the range of this parameter predicted from multispecies metapopulation models (*177*) and are consistent with limited historical observations, which suggest extant marine species have survived apparent range contractions less than 50% of their native range sizes (*171*).

5.7.4 IUCN assessments of extinction risk

We used the IUCN Red List (v. 2019-3; *178*) to estimate the regional and global extinction risk of marine animals (Tables 5.2, 5.3). The IUCN characterizes species threat statuses (ranging from least to most severe) as follows: 'least concerned', 'near-threatened', 'vulnerable', 'endangered', 'critically endangered', and 'extinct'. We used threat statuses to categorize species as either "not at risk" or "at risk" of extinction, following the approach previous workers (*38*, *172*). We consider two scenarios of extinction risk that vary in magnitude: 1) in our 'low estimate', species listed with a threat status of 'vulnerable' or more severe are considered 'at risk' of extinction, and 2) in our 'high estimate', species listed with a threat status of 'near-threatened' or more severe are considered 'at risk'. Extinction risk is calculated as the percent of assessed species that fall into the 'at risk' of extinction category. Species with threat statuses listed as ‘data deficient’ are not included in our analysis. We restricted our analysis to any species whose listed environment included the keyword “Marine”. To focus our analysis on water-breathing animals (i.e. species affected by temperature-dependent hypoxia in seawater), we excluded species in the classes Amphibia, Aves, Diplopoda, Insecta, Mammalia and Reptilia, which are air-breathers. For estimates of global extinction risk, 10,024 marine animal species were analyzed from the classes Actinopterygii, Anthozoa, Bivalvia, Cephalaspidomorphi, Cephalopoda, Chondrichthyes, Clitellata, Echinoidea, Enopla, Gastropoda, Holothuroidea, Hydrozoa, Malacostraca, Maxillopoda, Merostomata, Myxini, Ostracoda, Polychaeta, and Sarcopterygii (Table 5.2). Regional extinction risk was computed using the IUCN’s regional assessments for 10 marine regions and 2,253 species from the classes Actinopterygii, Anthozoa, Bivalvia, Chondrichthyes, Gastropoda and Myxini (Table 5.3). Regional extinction risk was estimated in regions with at least 10 marine species assessments (i.e. excluding northern, eastern and northeastern African regions).

We additionally analyzed extinction risk at the genus level. Following ref. (*172*), this was done in two ways: 1) based on the most threatened species in each genus and 2) based on the least threatened species in each genus. We find similar magnitudes of extinction risk at both the species and genus taxonomic levels (Tables 5.2,5.3).

To diagnose the drivers of current extinction risk in the IUCN assessments we utilized threat information from the IUCN for globally ‘at risk’ species. Twelve threats due to human activities are distinguished by the IUCN for ‘at risk’ species, including: 1. “Residential and Commercial Development”, 2. “Agriculture and Aquaculture”, 3. “Energy Production and Mining”, 4. “Transportation and Service Corridors”, 5. “Biological Resource Use”, 6. “Human Intrusions and Disturbance”, 7. “Natural System Modifications”, 8. “Invasive and Other Problematic Species, Genes and Diseases”, 9. “Pollution”, 10. “Geological Events”, 11. “Climate Change and Severe Weather”, and 12. “Other Options”. Of the 943-1379 species considered globally ‘at risk’ in our assessment, ~90% have threat factors listed by the IUCN. We tallied the total number of ‘at risk’ species threatened by each factor (Figure 5.8). The top five major threat factors for marine species are given shortened names in the main text: 1. “Urban Development”, 4. “Transportation”, 5. “Overfishing”, 9. “Pollution”, 11. “Climate change”. To compute the fraction of total marine species that are at risk of extinction due to climate change, we first computed the fraction of ‘at risk’ species affected by climate change and then multiplied this by the fraction of assessed species that are ‘at risk’ of extinction in general (Table 5.2).

5.8 Figures

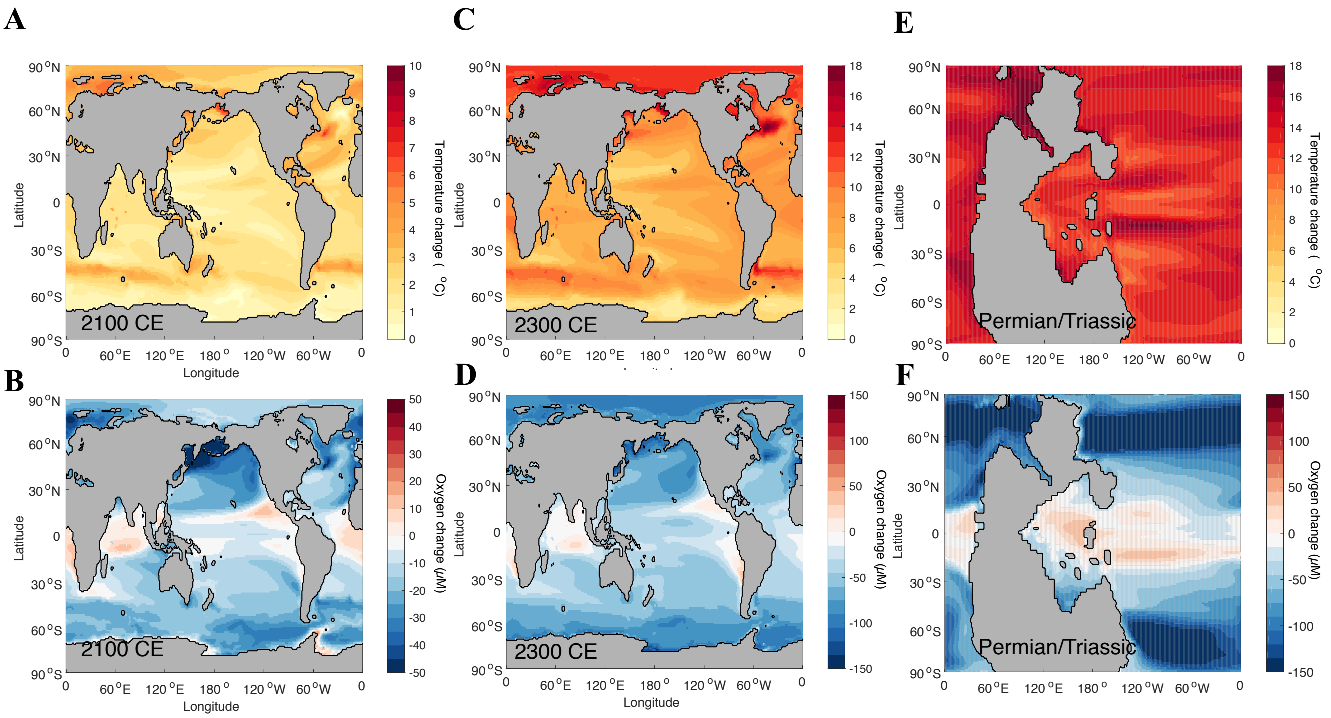

Figure 5.1. Climate change simulated under future greenhouse gas emissions and for the end-Permian extinction. Changes are computed as the difference between the last decade of the 21st (A, B) and 23rd centuries (C, D), relative to the pre-industrial climate (1850-1900) for the 'high emissions' scenario (see inset Figure 5.2A). Changes are averaged over the upper 500 m of the water-column and across 12 ESMs for the 21st century, and 4 ESMs for the 23rd century (Table 5.1; Section 5.7 Supplemental Methods). In (*E*, *F*) end-Permian ocean changes are computed from decadal averages as the difference between before and ~3000 years after an instantaneous increase in atmospheric greenhouse gas concentrations leading to a radiative forcing of >18 W/m^2 (Chapter 4). Grey shaded region is the land surface (modern continental configuration, A-D; Pangea supercontinent, E,F).

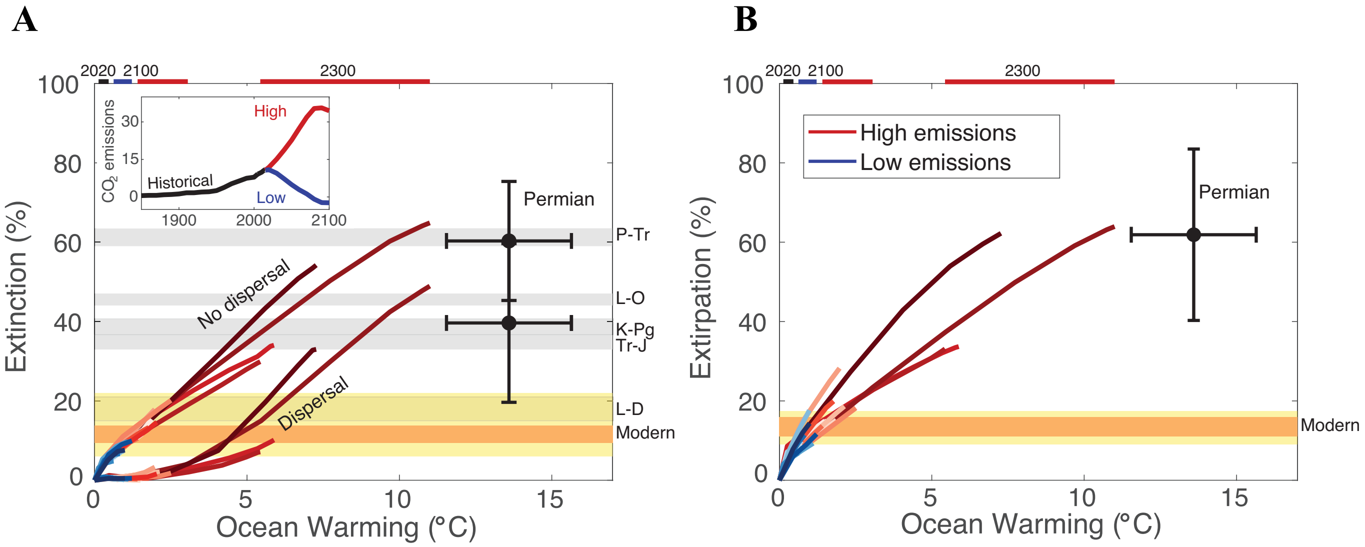

Figure 5.2. Marine extinction and extirpation risk from climate warming. Projected (A) global extinction and (B) regional extinction (extirpation) risks (% of species lost) driven by anthropogenic warming under divergent future climate scenarios (red and blue lines; n = 12 ESMs; Section 5.7 Supplemental Methods). Ocean warming is plotted relative to the pre-industrial state (time-mean 1850-1900). In the 'high emissions' scenario, greenhouse gas emissions (Pg C y^{-1}) continue accelerating with minimal constraints and yield a radiative forcing of 8.5 W/m^2 in 2100, while under 'low emissions', reductions are immediate (starting in 2020) and dramatic, lowering radiative imbalances to 2.6 W/m^2 in 2100 (inset in A; Section 5.7 Supplemental Methods). Simulated end-Permian extinction risks are shown as black symbols. IUCN-based estimates of current (A) global and (B) regional extinction risk for species (dark orange shading) and genera (light orange shading) are shown across 'high' and 'low' scenarios (labeled 'Modern'; Table 5.2, 5.3; Section 5.7 Supplemental Methods). The severity of five major past marine extinctions (% of genera lost) is shown (grey shading; *126*,*188*): end-Permian (P-Tr), Late Ordovician (L-O), end-Cretaceous (K-Pg), end-Triassic (Tr-J), Late Devonian (L-D). Warming and extirpation are globally averaged over the upper 500 m of the water-column. Horizontal lines on top axis show the inter-model range of global mean ocean warming for 2020, 2100 and 2300 CE. Error bars for the end-Permian simulation are spatial standard deviations. See Figure 5.3 for extinction risk plotted versus time and Figure 5.4 for warming plotted on a $\log_{10}$ scale.

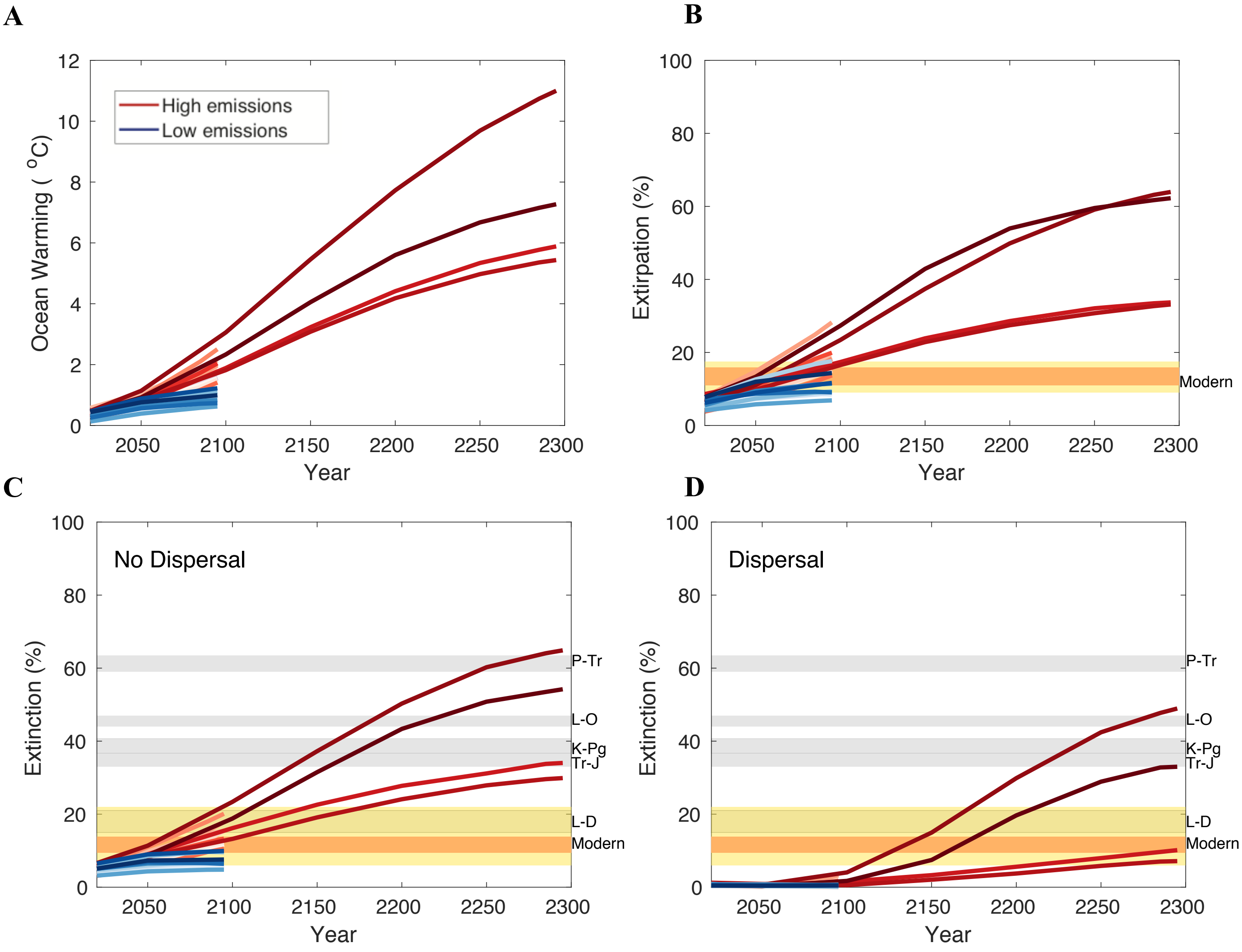

Figure 5.3. Marine extinction and extirpation risk from climate warming over time. Time-series of the projected magnitude of upper ocean warming (A), and risk of (B) extirpation, and (C and D) global extinction (% of species lost) under divergent future climate scenarios (inset Figure 5.2A; n = 12 ESMs). Two global extinction scenarios are presented: species that can only inhabit previously occupied habitat (C) and species that can instantaneously disperse to new aerobic habitat as it becomes available (D). Warming magnitudes and extirpation risks are globally averaged across grid cells over the upper 500 m of the water-column. The percentage of marine biodiversity currently at risk of going extinct (C, D) globally and (B) regionally, from IUCN data (labeled 'Modern'; *178*), is shown across a range of 'high' and 'low' scenarios for species (dark orange shading) and for genera (light orange shading) (Table 5.2,5.3; Section 5.7 Supplemental Methods). The severity of past marine extinctions (% of genera lost) is also shown for 5 major events in Earth history (grey shading) (*126*,*188*): end-Permian (P-Tr; ~252 million years ago (Ma)), Late Ordovician (L-O; ~443 Ma), end-Cretaceous (K-Pg; ~65 Ma), end-Triassic (Tr-J; ~200 Ma), Late Devonian (L-D; ~359 Ma).

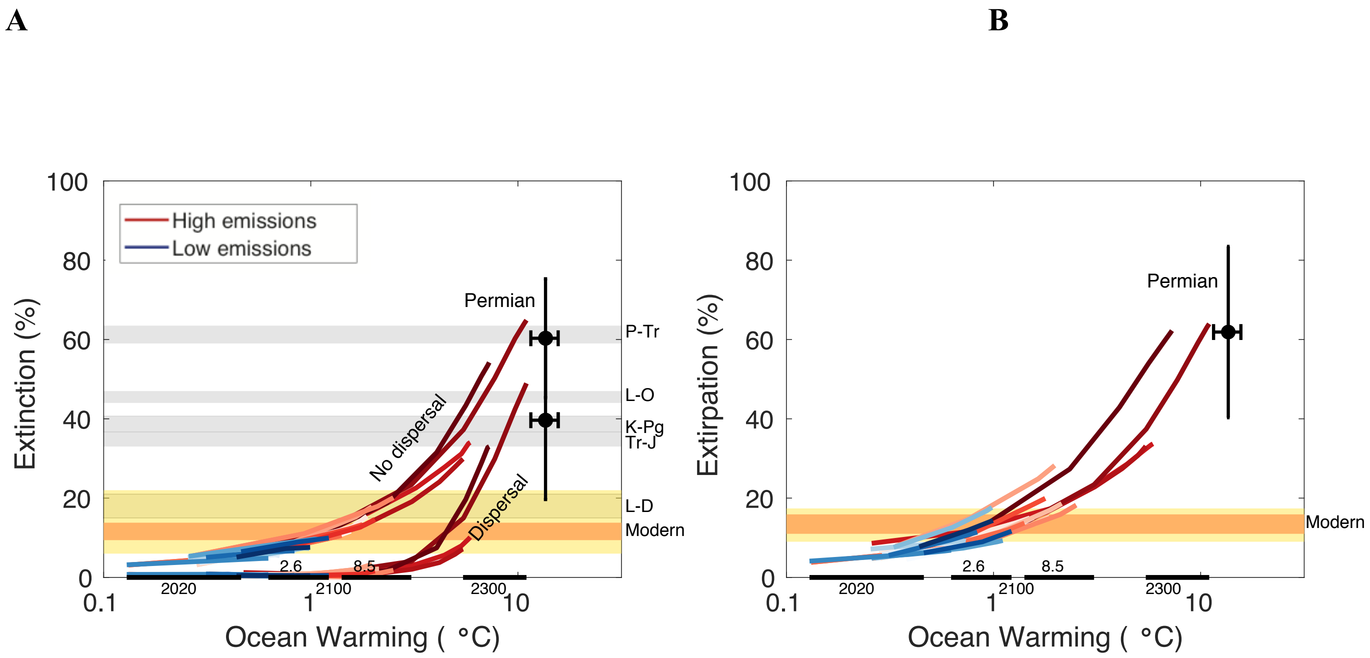

Figure 5.4. Marine extinction and extirpation risk from climate warming. Same as Figure 5.1, but with ocean warming plotted on a $\log_{10}$ scale for visual clarity at low warming magnitudes.

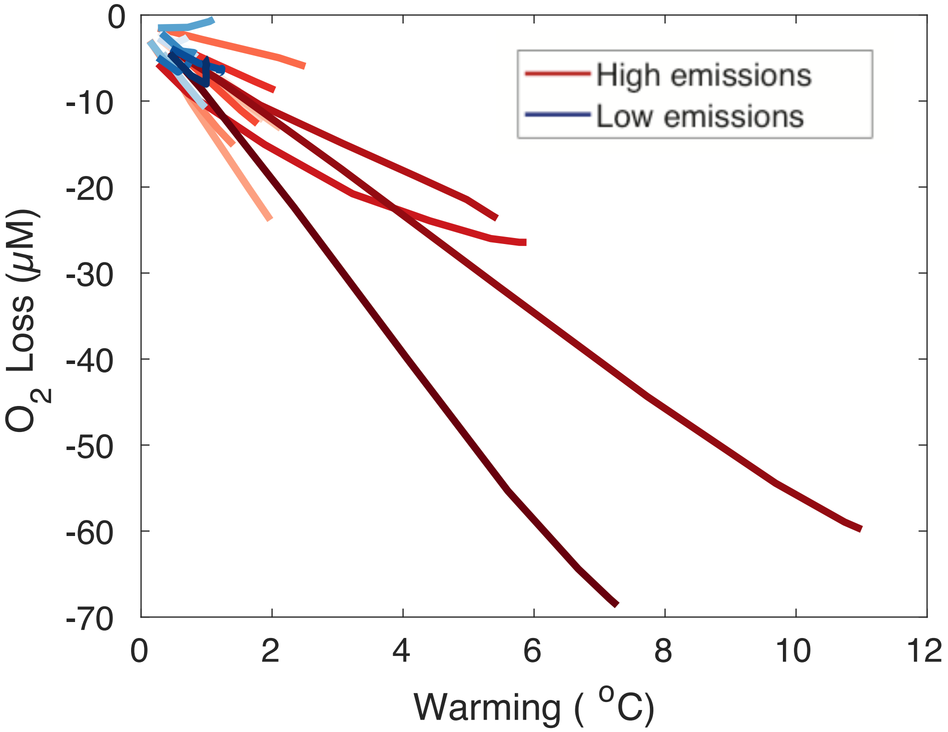

Figure 5.5. Future anomalies in ocean warming and O_2 loss under divergent climate change mitigation scenarios. Global mean O_2 loss and warming anomalies in the upper ocean (0-500 m) projected under 'high' and 'low' emission scenarios (n = 12 ESMs; inset Figure 5.2A; Table 5.1). Anomalies are plotted starting in the year 2020 and are relative to the pre-industrial period (1850-1900). Four models project changes to 2300 CE (darkest red and blue), while all others project changes to 2100 CE.

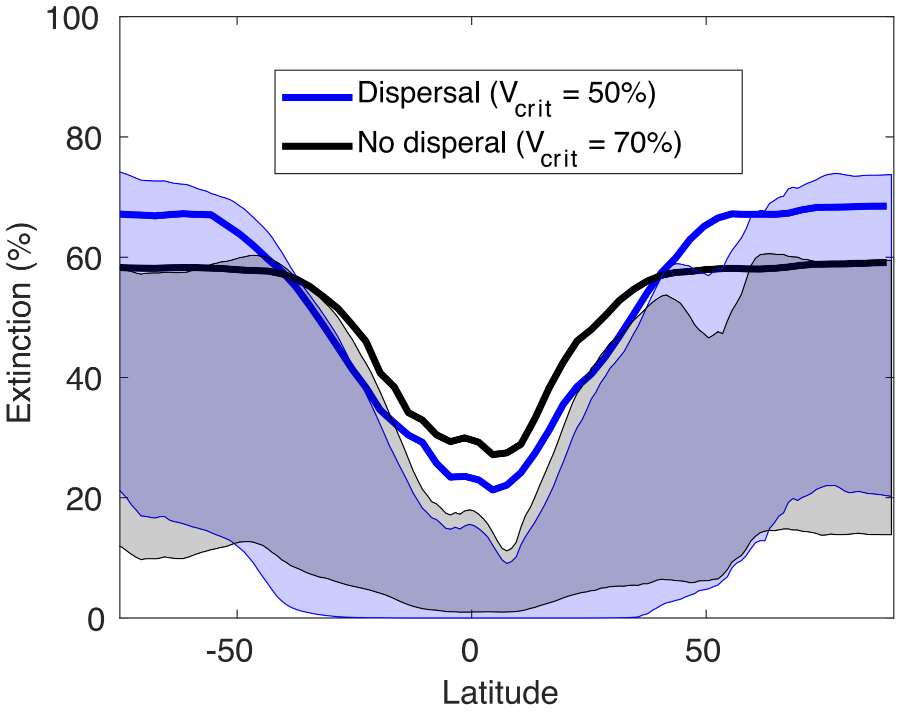

Figure 5.6. Latitudinal pattern of marine extinction under climate warming. Global extinction (%) versus latitude projected under the 'high emissions' scenario for 2300 CE (shading), and predicted under end-Permian climate change (lines). Two extinction scenarios are analyzed: species that instantaneously move to new aerobic habitat as it becomes available ('Dispersal'; blue) and species that can only inhabit previously occupied habitat ('No Dispersal'; black). Extinction intensity is averaged across longitude and over the upper 500 m of the water column. Shading outlines the inter-model range.

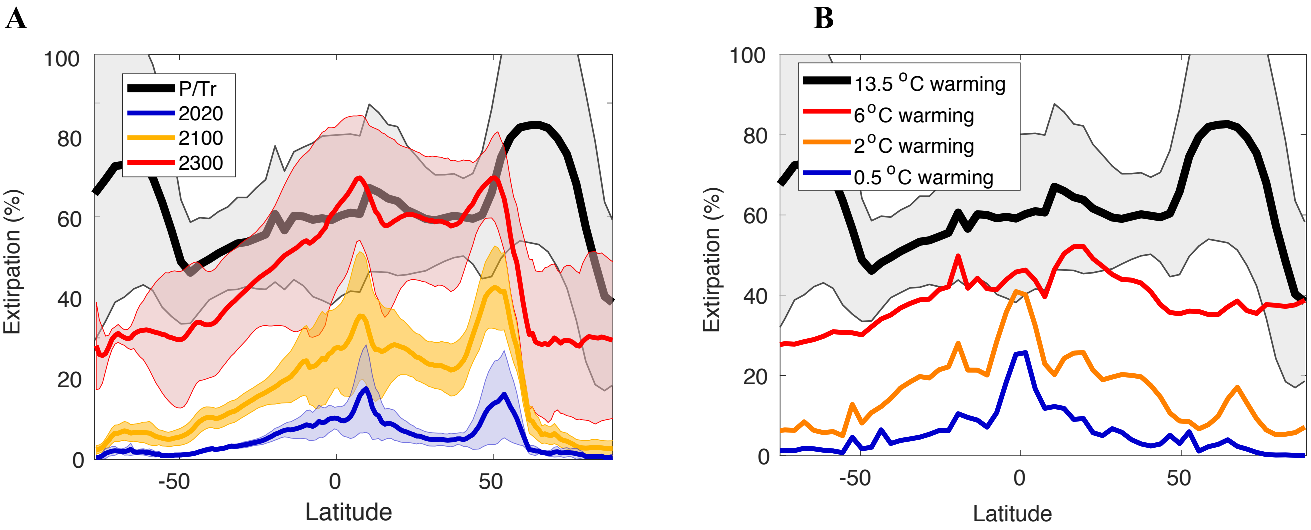

Figure 5.7. Latitudinal pattern of marine extirpation under climate warming. (A) Extirpation is projected under the 'high emissions' scenario for 2020 (blue), 2100 (orange), and 2300 CE (red). (B) Extirpations under transient end-Permian climate change for warming magnitudes of 0.5°C (blue), 2°C (orange), and 6°C (red), which approximate the global mean temperature anomalies projected for 2020, 2100, and 2300 CE, respectively. End-Permian extirpation under equilibrium warming is shown in black in both (A) and (B). Extirpation is averaged across longitude and over the upper 500 m of the water column. In A, thick lines show inter-model mean and shading shows inter-model standard deviation. For the end-Permian, shading shows the spatial standard deviation of extirpation.

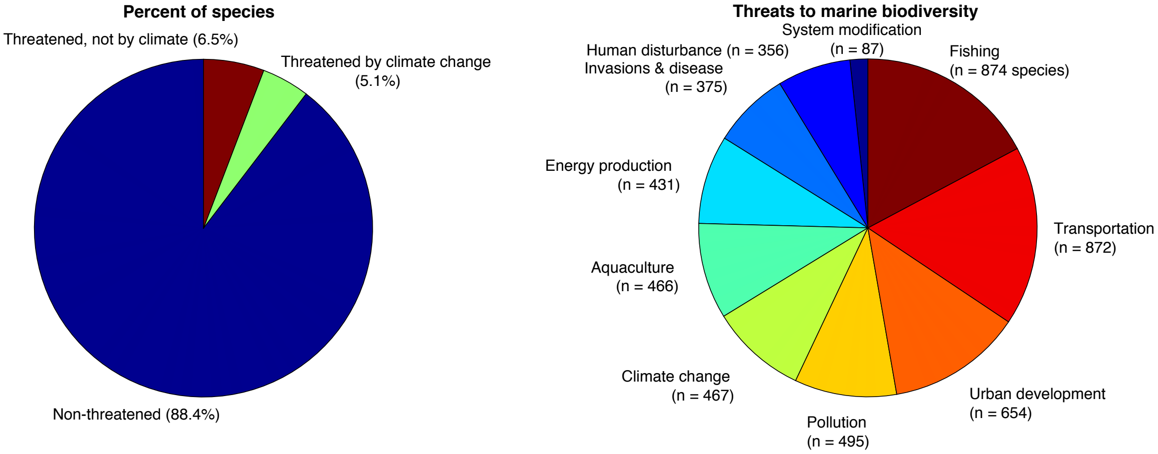

Figure 5.8. IUCN-based estimates of global extinction risk and drivers of extinction risk for assessed marine species. (A) Pie chart of the percent of marine species that are currently 'at risk' of global extinction and threatened by climate change (green), are 'at risk', but are not threatened by climate changes (red), and are not 'at risk' of extinction (blue). (B) Number of species threatened by each factor. The sum of species across threat factors exceeds the total number of threatened species because the same species can be threatened by multiple factors. Threats from "Geological Events" and "Other options" are not shown as they affect a small fraction of species. Pie charts show the average of high and low estimates. See Table 5.2 for details.

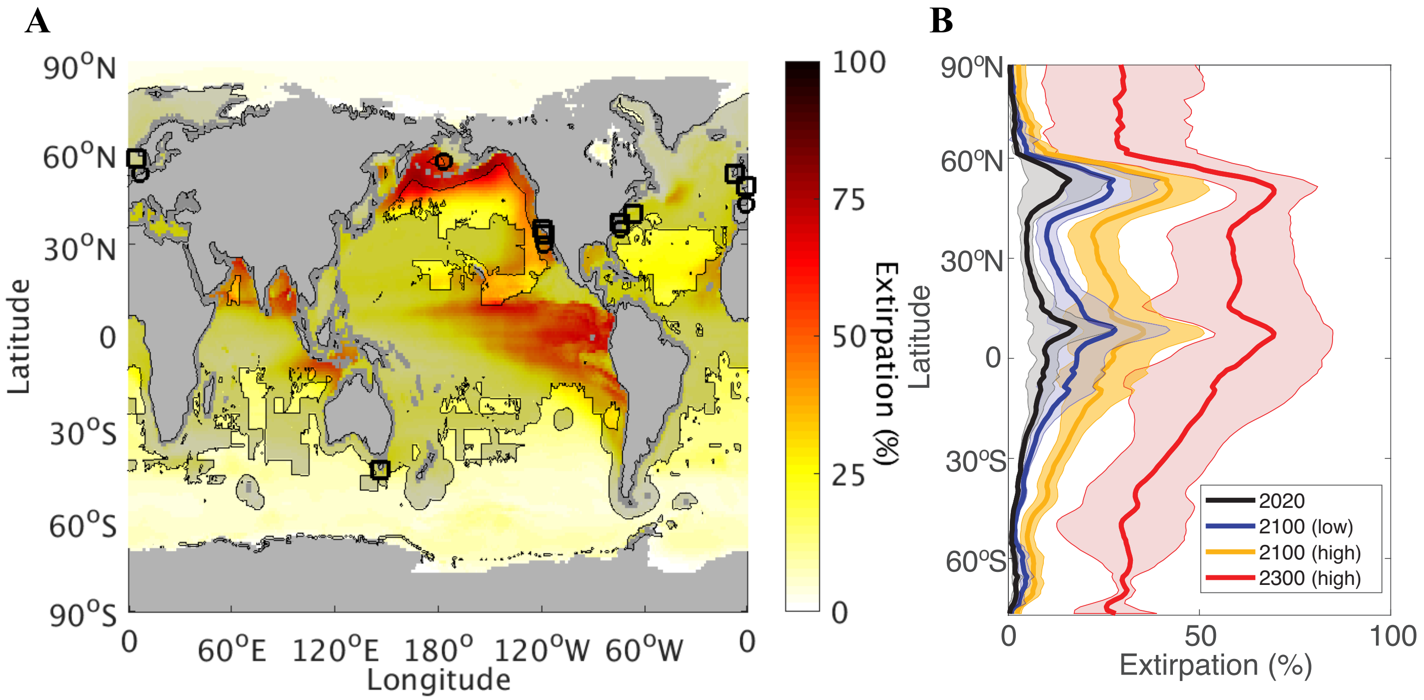

Figure 5.9. Biogeography of extirpation risk from climate warming. Map of extirpation risk (% of species lost) projected for the end of the 21st century under the 'high emissions' scenario (colors), the historical distribution of productive fisheries (shading), and documented species poleward range shifts (circles) and population declines (squares) at equatorial range limits previously attributed to warming and/or O_2 loss (n = 22; *35*,*174*) (A). Productive fisheries are locations with time-mean species catch rates exceeding the global median value, from reconstructions covering the period 1950-2014. (B) Latitudinal pattern of extirpation risk from climate warming under divergent greenhouse gas emission scenarios. Extirpation is averaged over the top 500 m of the water column, across ESMs, and in B, across longitude (thick lines are inter-model mean; shadings are standard deviation).

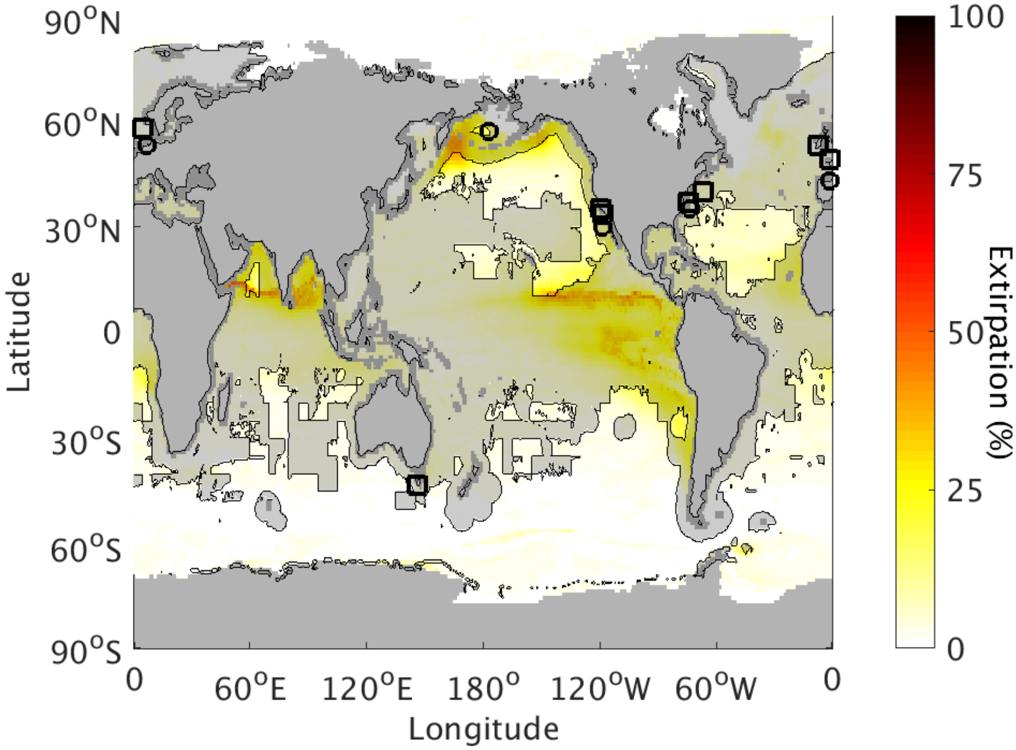

Figure 5.10. Biogeography of current extirpation risk from climate warming. (A) Same as Figure 5.9A, but mapped for the year 2020 CE (colors). Extirpation risk (%) is compared to the historical distribution of productive fisheries (shading) and documented species' extirpations and/or range shifts (black symbols). Productive fisheries are defined as locations with time-mean species catch rates exceeding the global median value, from reconstructions covering the period 1950-2014. Documented poleward shifts (circles) and population declines (squares) at species' equatorial range limits that have been previously attributed to warming and/or O_2 loss are shown as black symbols (n = 22; *35*,*174*).

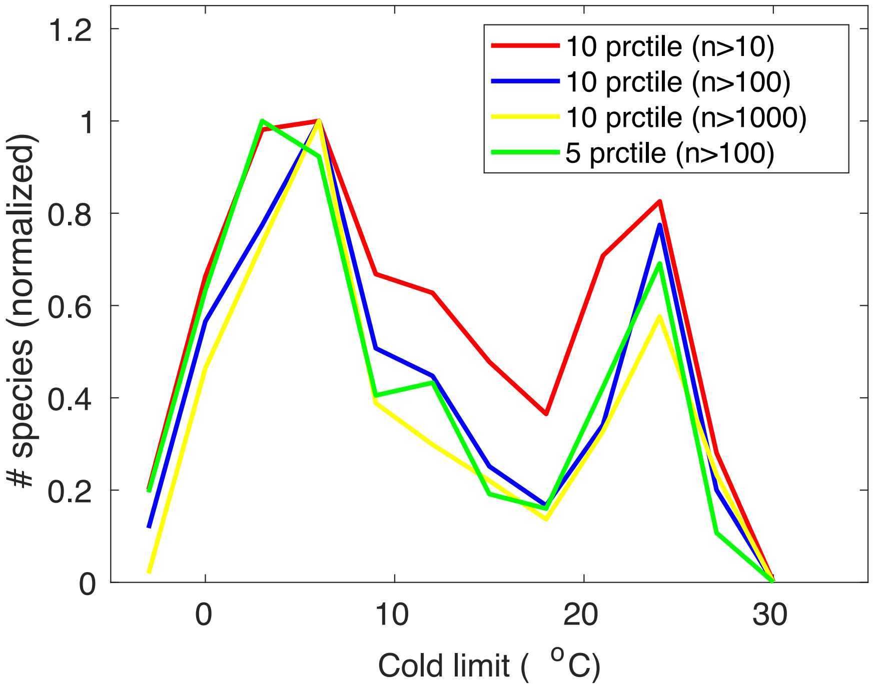

Figure 5.11. Histogram of species cold tolerances inferred from biogeographic occurrence data. The distribution of species cold limits (T^{cold}) inferred from geo-referenced species occurrence data from OBIS (186) paired to hydrographic conditions from WOA (185). Cold limits are inferred from a lower percentile of occupied temperature above which most specimen occurrences are found. The distribution of species cold limits is insensitive to whether the 5th or 10th percentile is used as the lower threshold and is also insensitive to the minimum occurrence sampling density per species.

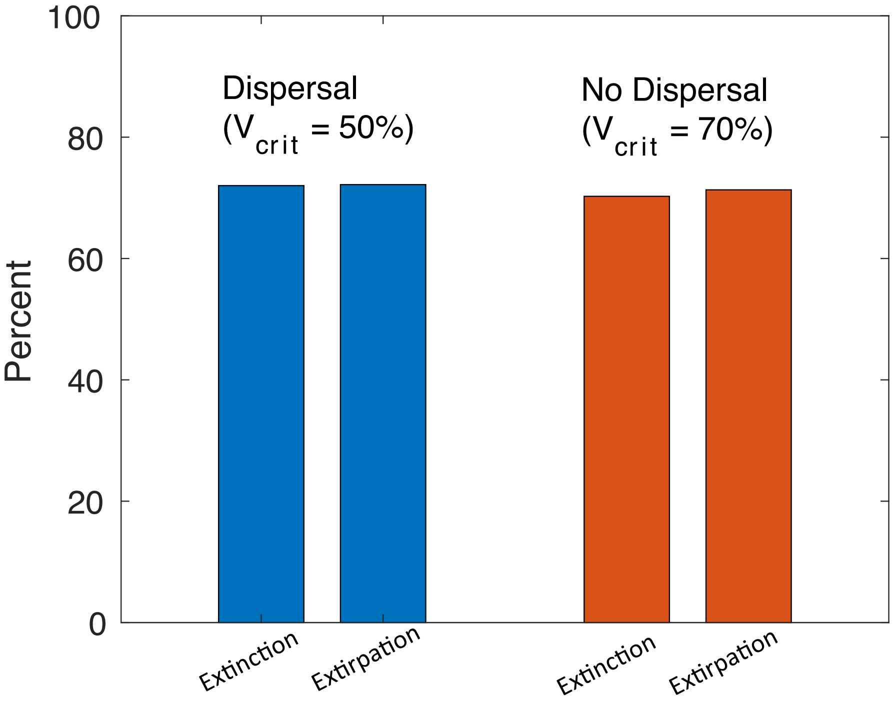

Figure 5.12. Fraction of end-Permian extinction magnitudes in the fossil record accounted for by model extinction risks. Spatial mean of global extinction and extirpation risks from end-Permian model simulations plotted relative to corresponding values reconstructed from the fossil record (Chapter 4). Two global extinction scenarios are analyzed: species that instantaneously move to newly available habitat ('Dispersal'; blue bars) and species that can only inhabit previously occupied habitat ('No dispersal'; orange bars). We constrained V_{crit} in the model such that aerobic habitat loss accounts for a similar fraction of the observed global extinction as extirpation in the fossil record. This constraint yields estimates of the critical habitat loss threshold parameter (V_{crit}) equal to 50% and 70% for 'Dispersal' and 'No dispersal' scenarios, respectively. When comparing model metrics to the fossil record, extirpation includes losses via both regional and global extinction mechanisms to facilitate a more direct comparison to the reconstructions (Chapter 4). Model fields are averaged globally and over the upper 500 m of the water-column. Fossil record reconstructions are averaged across latitude.

5.9 Tables

Table 5.1. Earth System Models used to project future changes in ocean temperature and oxygen. Models were run for CMIP6 using both SSP1-2.6 and SSP5-8.5 scenarios, except where noted. [a]Models run for CMIP5. [b]Models without SSP1-2.6 or RCP-2.6 available.

Modeling Center (or Group)	**Model Name**	**End year**
Canadian Centre for Climate Modelling and Analysis	CanESM5	2300
Community Earth System Model Contributors, NCAR	CESM1 (BGC)	2100[a,b]
National Centre for Meteorological Research	CNRM-ESM2-1	2100
Commonwealth Scientific and Industrial Research Organisation	ACCESS-ESM1-5	2100
NOAA Geophysical Fluid Dynamics Laboratory	GFDL-ESM4	2100
Met Office Hadley Centre (additional HadGEM2-ES realizations contributed by Instituto Nacional de Pesquisas Espaciais)	HadGEM2-ES	2300[a]
Institut Pierre-Simon Laplace	IPSL-CM6A-LR	2300
Model for Interdisciplinary Research on Climate, University of Tokyo, NIES, JAMSTEC	MIROC-ES2L	2100
Max-Planck-Institut für Meteorologie (Max Planck Institute for Meteorology)	MPI-ESM1-2-LR MPI-ESM-LR[a]	2100, 2300[a]
Meteorological Research Institute, Japan Meterological Agency	MRI-ESM2-0	2100[b]
Norwegian Climate Center	NorESM2-MM	2100
Met Office Hadley Centre and Natural Environment Research Council	UKESM1-0-LL	2100

Table 5.2. Modern global extinction risk based on IUCN Red List data. Extinction risks are analyzed at the species and genus levels. The percent of 'at risk' taxa are shown across a range of low and high estimates. High estimates include taxa with a threat status of 'near-threatened' or worse. Low estimates use 'threatened' taxa as the lower threshold for 'at risk'. For genera, extinction risk is computed based on the most and least threatened species in each genus. Extinction risks linked to climate change are calculated at the species level. For ~ 90% of 'at risk' species, associated threat factors are also known. These species are used to compute the central estimate of percent of species 'at risk' and affected by climate change[a]. The range of values (parentheses) includes 'at risk' species without threat information, assuming all or none of these species are affected by climate change.

Taxonomic level	Assessed taxa	'At risk' (%) (number)	'At risk' species (%) and affected by climate change[a]	'At risk' species w/ threat information	'At risk' species (%) threatened by climate change (number of species)
Species	10025	9.4-13.8% (943-1379)	4-6.2% (3.6 - 6.8%)	850 - 1269	42.7-45.1% (363-572)
Genera	2181	6-21.9% (144-522)			

Table 5.3. Modern regional extinction risk based on IUCN Red List data. Extinction risks are analyzed at the species and genus levels. For each region, the percent of ‘at risk’ taxa are shown across a range of low and high estimates. For genera, extinction risk is computed based on the most and least threatened species in each genus. High estimates of ‘at risk’ taxa include those with a threat status of ‘near-threatened’ or worse. Low estimates use ‘threatened’ taxa as the lower threshold for ‘at risk’. The range of values reported in Figure 5.2B are the average of low estimates across regions and high estimates across regions.

Region	Assessed Species	‘At risk’ species (%) (number of species)	Assessed Genera	‘At risk’ genera (%) (number of genera)
Arabian Sea	20	35-60% (7-12)	16	25-62.5% (4-10)
Caribbean	244	12.3-12.7% (30-31)	98	5.1-13.3 (5-13)
Central Africa	30	0% (0)	20	0% (0)
Europe	829	8.2-11.5% (68-95)	502	6.6-13.3% (33-67)
Gulf of Mexico	847	4-5.1% (34-43)	385	1.8-6.8 (7-26)
Mediterranean	448	14.5-20.8% (65-93)	308	14.9-22.7 (46-70)
Persian Gulf	376	8.2-10.9% (31-41)	228	7.5-12.7 (17-29)
South Africa	12	8.3% (1)	10	10% (1)
West Africa	22	9.1-13.6% (2-2)	20	10-15% (2-3)
Average	314	11-15.9%	176	9-17.4%

Data Availability

Microbial ecosystem model output for Chapters 2 and 3, including NH_4^+ data from Chapter 3, is available at https://figshare.com/articles/Data_for_Penn_et_al_2019_Microbial_ecosystem_dynamics_drive_fluctuating_nitrogen_loss_in_marine_anoxic_zones_PNAS_/7627439. P/Tr climate model output from Chapter 4 is available at https://figshare.com/articles/dataset/End-Permian_Climate_Change/7357193. The most current database and code for extracting Metabolic Index traits from species laboratory and field data (Chapters 4 and 5) can be found at https://github.com/cadeutsch/Metabolic-Index-Traits (*28*). Model extinction code for Chapter 5 will be made available upon publication at https://github.com/jlpenn/Metabolic-Index-6extinct. All other code can be made available upon request.

Bibliography

1. J. Sarmiento, N. Gruber, Ocean Biogeochemical Dynamics. *Princeton University Press* (2006).
2. S. Emerson, J. Hedges, Chemical Oceanography and the Marine Carbon Cycle. *Cambridge University Press* (2008).
3. R. F. Keeling, A. Körtzinger, N. Gruber, Ocean Deoxygenation in a Warming World. *Ann. Rev. Mar. Sci.* **2**, 199–229 (2010).
4. H. E. Garcia *et al. World Ocean Atlas 2013, Volume 3: Dissolved Oxygen, Apparent Oxygen Utilization, and Oxygen Saturation. S. Levitus, Ed., A. Mishonov Technical Ed.; NOAA Atlas NESDIS 75, (2014).*
5. S. Schmidtko, L. Stramma, M. Visbeck, Decline in global oceanic oxygen content during the past five decades. *Nature.* **542**, 335–339 (2017).
6. D. Breitburg *et al.*, Declining oxygen in the global ocean and coastal waters. *Science.* **359** (2018), doi:10.1126/science.aam7240.
7. L. Stramma, G. C. Johnson, J. Sprintall, V. Mohrholz, Expanding oxygen-minimum zones in the tropical oceans. *Science.* **320**, 655–658 (2008).
8. D. Roemmich, W. John Gould, J. Gilson, 135 years of global ocean warming between the Challenger expedition and the Argo Programme. *Nat. Clim. Chang.* **2**, 425–428 (2012).
9. M. Collins, E. Al, "Climate Change 2013: The Physical Science Basis. Contribution of Working Group I to the Fifth Assessment Report of the Intergovernmental Panel on Climate Change" (Cambridge Univ. Press, 2013).
10. L. Bopp *et al.*, Multiple stressors of ocean ecosystems in the 21st century: Projections with CMIP5 models. *Biogeosciences*. **10**, 6225–6245 (2013).
11. L. Kwiatkowski *et al.*, Twenty-first century ocean warming, acidification, deoxygenation, and upper-ocean nutrient and primary production decline from CMIP6 model projections, *Biogeosciences*. **17**, 3439–3470 (2020).
12. D. A. Stolper, N. P. Revsbech, D. E. Canfield, Aerobic growth at nanomolar oxygen concentrations. *Proc. Natl. Acad. Sci.* **107**, 18755–18760 (2010).
13. T. Kalvelage *et al.*, Aerobic microbial respiration in oceanic oxygen minimum zones. *PLoS One*. **10**, 1–17 (2015).

14. L. A. Bristow *et al.*, Ammonium and nitrite oxidation at nanomolar oxygen concentrations in oxygen minimum zone waters. *Proc. Natl. Acad. Sci.* **113**, 10601–10606 (2016).
15. C. Deutsch, T. Weber, Nutrient Ratios as a Tracer and Driver of Ocean Biogeochemistry. *Ann. Rev. Mar. Sci.* **4**, 113–141 (2012).
16. J. Karstensen, L. Stramma, M. Visbeck, Oxygen minimum zones in the eastern tropical Atlantic and Pacific oceans. *Prog. Oceanogr.* **77**, 331–350 (2008).
17. P. Lam, M. M. M. Kuypers, Microbial Nitrogen Cycling Processes in Oxygen Minimum Zones. *Ann. Rev. Mar. Sci.* **3**, 317–345 (2011).
18. P. G. Brewer, A. F. Hofmann, E. T. Peltzer, W. Ussler, Evaluating microbial chemical choices: The ocean chemistry basis for the competition between use of O_2 or NO_3^- as an electron acceptor. *Deep. Res. Part I Oceanogr. Res. Pap.* **87**, 35–42 (2014).
19. T. Kalvelage *et al.*, Nitrogen cycling driven by organic matter export in the South Pacific oxygen minimum zone. *Nat. Geosci.* **6**, 228–234 (2013).
20. T. Devries, C. Deutsch, F. Primeau, B. Chang, A. Devol, Global rates of water-column denitrification derived from nitrogen gas measurements. *Nat. Geosci.* **5**, 547–550 (2012).
21. T. Tyrrell, The relative influences of nitrogen and phosohorus on oceanic primary production. *Nature*. **400**, 525–531 (1999).
22. T. Weber, C. Deutsch, Oceanic nitrogen reservoir regulated by plankton diversity and ocean circulation. *Nature*. **489**, 419–422 (2012).
23. D. S. Grundle *et al.*, Low oxygen eddies in the eastern tropical North Atlantic : Implications for N_2O cycling, *Scientific Reports*. **7**, 1–10 (2017).
24. D. Bianchi, T. S. Weber, R. Kiko, C. Deutsch, Global niche of marine anaerobic metabolisms expanded by particle microenvironments. *Nature Geoscience*. **11**, 263-268 (2018), doi:10.1038/s41561-018-0081-0.
25. A. H. Devol, Denitrification, anammox and N_2 Production in Marine Sediments. *Ann. Rev. Mar. Sci. 7, 403-423* (2015), doi:10.1146/annurev-marine-010213-135040.
26. R. Vaquer-sunyer, C. M. Duarte, Thresholds of hypoxia for marine biodiversity.

PNAS. **105**, 15452-15457 (2008).

27. C. Deutsch, A. Ferrel, B. Seibel, H.O. Pörtner, R. B. Huey Climate change tightens a metabolic constraint on marine habitats. *Science.* **348**, 1132–1136 (2015).
28. C. Deutsch, J. L. Penn, B. Seibel, Metabolic trait diversity shapes marine biogeography. *Nature*. **585** (2020), doi:10.1038/s41586-020-2721-y.
29. N. J. Rogers, M. A. Urbina, E. E. Reardon, D. J. Mckenzie, R. W. Wilson, A new analysis of hypoxia tolerance in fishes using a database of critical oxygen level (P_{crit}). *Conservation physiology*. **4**, 1–19 (2016).
30. K. F. Wishner *et al.*, Ocean deoxygenation and zooplankton : Very small oxygen differences matter, *Science Adv.* 1–9 (2018).
31. J. F. Gillooly, J. H. Brown, G. B. West, Effects of Size and Temperature on Metabolic Rate. *Science*. **293**, 1–6 (2001).
32. B. A. Grantham *et al.,* Upwelling-driven nearshore hypoxia signals ecosystem and oceanographic changes. *Nature*. **429**, 749–754 (2004).
33. F. Chan *et al.*, Emergence of Anoxia in the California Current Large Marine Ecosystem. *Science* **319** (2008), doi:10.1126/science.1149016.
34. J. A. Koslow, R. Goericke, A. Lara-lopez, W. Watson, Impact of declining intermediate-water oxygen on deepwater fishes in the California Current. *Mar. Eco. Prog. Ser.* **436**, 207-218 (2011), doi:10.3354/meps09270.
35. E. M. Howard, J. L. Penn, H. Frenzel, B. A. Seibel, D. Bianchi, L. Renault, F. Kessouri, M. A. Sutula, J. C. McWilliams, C. Deutsch, Climate-driven aerobic habitat loss in the California Current System, *Science Adv.* **6**, 1–12 (2020).
36. C. Deutsch, H. Brix, T. Ito, H. Frenzel, L. A. Thompson, Climate-forced variability of ocean hypoxia. *Science.* **333**, 336–339 (2011).
37. C. Deutsch *et al.*, Centennial changes in North Pacific anoxia linked to tropical trade winds. *Science.* **345**, 665–668 (2014).
38. A. D. Barnosky *et al.*, Has the Earth's sixth mass extinction already arrived? *Nature*. **471**, 51–57 (2011).
39. J. L. Payne, M. E. Clapham, End-Permian Mass Extinction in the Oceans : An Ancient Analog for the Twenty-First Century? *Ann. Rev. Earth Planet. Sci.* ***40**, 89-111* (2012), doi:10.1146/annurev-earth-042711-105329.

40. Y. Isozaki, Permo-Triassic Boundary Superanoxia and Stratified Superocean: Records from Lost Deep Sea. *Science.* **276**, 235–238 (1997).

41. G. A. Brennecka, A. D. Herrmann, T. J. Algeo, A. D. Anbar, Rapid expansion of oceanic anoxia immediately before the end-Permian mass extinction. PNAS. **108**, 17631–17634 (2011).

42. K. V. Lau *et al.*, Marine anoxia and delayed Earth system recovery after the end-Permian extinction. *Proc. Natl. Acad. Sci.* **113**, 2360–2365 (2016).

43. M. M. Joachimski *et al.*, Climate warming in the latest Permian and the Permian-Triassic mass extinction. *Geology*. **40**, 195–198 (2012).

44. Y. Sun, et al, Lethally Hot Temperatures During the Early Triassic Greenhouse. *Science*. **366** (2012), doi:10.1126/science.1224126.

45. S. D. Burgess, S. Bowring, S. Shen, High-precision timeline for Earth ' s most severe extinction. *Proc. Natl. Acad. Sci.* **111**, 3316–3321 (2014).

46. C. Sagan, *Cosmos* (The Random House Publishing Group, 1980).

47. D. G. Capone, D. A. Bronk, M. R. Mulholland, E. J. Carpenter, *Nitrogen in the Marine Environment* (Academic Press Elsevier, ed. 2nd, 2008).

48. A. Paulmier, I. Kriest, A. Oschlies, A. O. Stoichiometries of remineralisation and denitrification in global biogeochemical ocean models, *Biogeosciences.* **6**, 923–935 (2009).

49. J. K. Moore, S. C. Doney, Iron availability limits the ocean nitrogen inventory stabilizing feedbacks between marine denitrification and nitrogen fixation. *Global Biogeochem. Cycles*. **21**, 1–12 (2007).

50. D. Bianchi, J. P. Dunne, J. L. Sarmiento, E. D. Galbraith, Data-based estimates of suboxia, denitrification, and N_2O production in the ocean and their sensitivities to dissolved O_2. *Global Biogeochem. Cycles*. **26**, 1–13 (2012).

51. Dalsgaard T., Canfield D.E., Peterson J., Thamdrup B., Acuna-Gonzales J., N_2 production by anamox in the anoxic water column of Golfo Dulce, Costa Rica. *Nature*. **422**, 606–608 (2003).

52. A. J. J., A. Okubo, A. S. Robbins, F. A. Richards, A model for nitrite and nitrate distributions in the oceanic oxygen minimum zones. *Deep Sea Res. Part A, Oceanogr. Res. Pap.* **29**, 1113–1140 (1982).

53. M. M. M. Kuypers *et al.*, Massive nitrogen loss from the Benguela upwelling system through anaerobic ammonium oxidation. *PNAS.* **102**, 6478‑6483 (2005).

54. B. B. Ward *et al.*, Denitrification as the dominant nitrogen loss process in the Arabian Sea. *Nature*. **461**, 78–81 (2009).

55. J. M. Beman, J. Leilei Shih, B. N. Popp, Nitrite oxidation in the upper water column and oxygen minimum zone of the eastern tropical North Pacific Ocean. *ISME J.* **7**, 2192–2205 (2013).

56. T. Dalsgaard, B. Thamdrup, L. Farías, N. P. Revsbech, Anammox and denitrification in the oxygen minimum zone of the eastern South Pacific. *Limnol. Oceanogr.* **57**, 1331–1346 (2012).

57. B. B. Ward, How Nitrogen Is Lost. **341**, 352–354 (2013).

58. X. Peng, C. A. Fuchsman, A. Jayakumar, S. Oleynik, W. Martens-habbena, Ammonia and nitrite oxidation in the Eastern Tropical North Pacific. *Global Biogeochem. Cycles*. **29**, 2034–2049 (2015).

59. A. H. Devol, Bacterial oxygen uptake kinetics as related to biological processes in oxygen deficient zones of the oceans. *Deep. Sea Res.* **25**, 137–146 (1978).

60. L. M. Zamora *et al.*, Nitrous oxide dynamics in low oxygen regions of the Pacific: Insights from the MEMENTO database. *Biogeosciences*. **9**, 5007–5022 (2012).

61. M. M. Jensen, M. M. M. Kuypers, G. Lavik, B. Thamdrup, Rates and regulation of anaerobic ammonium oxidation and denitrification in the Black Sea. *Limnol. Oceanogr.* **53**, 23–36 (2008).

62. T. Kalvelage *et al.*, Oxygen sensitivity of anammox and coupled N-cycle processes in oxygen minimum zones. *PLoS One*. **6** (2011), doi:10.1371/journal.pone.0029299.

63. B. Kartal, L. van Niftrik, J. T. Keltjens, H. J. M. Op den Camp, M. S. M. Jetten, Anammox-Growth Physiology, Cell Biology, and Metabolism. *Advances in Microbial Physiology.* **60** (2012).

64. T. Dalsgaard *et al.*, Oxygen at nanomolar levels reversibly suppresses process rates and gene expression in anammox and denitrification in the oxygen minimum zone off Northern Chile. *MBio*. **5**, 1–14 (2014).

65. T. Kalvelage *et al.*, Nitrogen cycling driven by organic matter export in the South

Pacific oxygen minimum zone. *Nat. Geosci.* **6**, 228–234 (2013).

66. L. Tiano *et al.*, Oxygen distribution and aerobic respiration in the north and south eastern tropical Pacific oxygen minimum zones. *Deep. Res. Part I Oceanogr. Res. Pap.* **94**, 173–183 (2014).
67. T. DeVries, F. Primeau, Dynamically and Observationally Constrained Estimates of Water-Mass Distributions and Ages in the Global Ocean. *J. Phys. Oceanogr.* **41**, 2381–2401 (2011).
68. T. Devries, C. Deutsch, F. Primeau, B. Chang, A. Devol, Global rates of water-column denitrification derived from nitrogen gas measurements. *Nat. Geosci.* **5**, 547–550 (2012).
69. Antonov, J. I., D. Seidov, T. P. Boyer, R. A. Locarnini, A. V. Mishonov, H. E. Garcia, O. K. Baranova, M. M. Zweng, and D. R. Johnson (2010), World ocean database 2009. In NOAA Atlas NESDIS 66 (US Govt Printing Office).
70. A. R. Babbin, R. G. Keil, A. H. Devol, B. B. Ward, Organic matter stoichiometry, flux, and oxygen control nitrogen loss in the ocean. *Science.* **344**, 406–408 (2014).
71. D. Tilman, *Resource Competition and Community Structure* (Princeton University Press, 1982).
72. N. P. Revsbech *et al.*, Determination of ultra-low oxygen concentrations in oxygen minimum zones by the STOX sensor. *Limnol. Oceanogr. Methods*. **7**, 371–381 (2009).
73. B. Thamdrup, T. Dalsgaard, N. P. Revsbech, Widespread functional anoxia in the oxygen minimum zone of the Eastern South Pacific. *Deep. Res. Part I Oceanogr. Res. Pap.* **65**, 36–45 (2012).
74. F. Lipschultz *et al.*, Bacterial transformations of inorganic nitrogen in the oxygen-deficient waters of the Eastern Tropical South Pacific Ocean. *Deep Sea Res. Part A, Oceanogr. Res. Pap.* **37**, 1513–1541 (1990).
75. J. Füssel *et al.*, Nitrite oxidation in the Namibian oxygen minimum zone. *ISME J.* **6**, 1200–1209 (2012).
76. K. L. Casciotti, M. R. McIlvin, Isotopic analyses of nitrate and nitrite from reference mixtures and application to Eastern Tropical North Pacific waters. *Mar. Chem.* **107**, 184–201 (2007).

77. C. Buchwald, A. E. Santoro, R. H. R. Stanley, K. L. Casciotti, Nitrogen cycling in the secondary nitrite maximum of the eastern tropical North Pacific off Costa Rica. *Global Biogeochem. Cycles*, **29**, 2061–2081 (2015).

78. B. X. Chang, A. H. Devo, S. R. Emerson, Fixed nitrogen loss from the eastern tropical North Pacific and Arabian Sea oxygen deficient zones determined from measurements of N_2:Ar. *Global Biogeochem. Cycles*. **26**, 1–8 (2012).

79. W. Koeve, P. Kähler, Heterotrophic denitrification vs. autotrophic anammox-quantifying collateral effects on the oceanic carbon cycle. *Biogeosciences*. **7**, 2327–2337 (2010).

80. P. Lam *et al.*, Revising the nitrogen cycle in the Peruvian oxygen minimum zone. *Proc. Natl. Acad. Sci.* **106**, 4752–4757 (2009).

81. D. Bianchi, A. R. Babbin, E. D. Galbraith, Enhancement of anammox by the excretion of diel vertical migrators. *Proc. Natl. Acad. Sci.* **111**, 15653–15658 (2014).

82. B. J. Ni, M. Ruscalleda, C. Pellicer-Nacher, and B. F Smets, Modeling Nitrous Oxide Production during Biological Nitrogen Removal via Nitrification and Denitrification: A Simple Extension to the General ASM Descriptive Models. *Environ. Sci. Tech.* **45**, 7768–7776 (2011).

83. B. A. S. Van Mooy, R. G. Keil, A. H. Devol, Impact of suboxia on sinking particulate organic carbon: Enhanced carbon flux and preferential degradation of amino acids via denitrification. *Geochim. Cosmochim. Acta*. **66**, 457–465 (2002).

84. B. E. Rittmann, P. L. McCarty, Stoichiometry and bacterial energetics. *Environ. Biotechnol. Princ. Appl.* (McGraw-Hill, 2001).

85. L. A. Anderson, On the hydrogen and oxygen content of marine phytoplankton. *Deep Sea Res. Part I Oceanogr. Res.* **42**, 1675–1680 (1995).

86. M. J. R. Fasham, H. W. Ducklow, S. M. McKelvie, A nitrogen-based model of plankton dynamics in the oceanic mixed layer. *J. Mar. Res.* **48**, 591–639 (1990).

87. R. Fukuda, H. Ogawa, T. Nagata, I. Koike, Direct Determination of Carbon and Nitrogen Contents of Natural Bacterial Assemblages in Marine Environments. *Appl. Environ. Microbio;*. **64**, 3352–3358 (1998).

88. M. Strous, J. J. Heijnen, J. G. Kuenen, M. S. M. Jetten, The sequencing batch

reactor as a powerful tool for the study of slowly growing anaerobic ammonium-oxidizing microorganisms. *Appl. Microbiol. Biotechnol.* **50**, 589–596 (1998).

89. T. Dalsgaard, B. Thamdrup, Factors Controlling Anaerobic Ammonium Oxidation with Nitrite in Marine Sediments Factors Controlling Anaerobic Ammonium Oxidation with Nitrite in Marine Sediments. *Appl. Environ. Microbiol.* **68**, 3802–3808 (2002).
90. W. Martens-Habbena, P. M. Berube, H. Urakawa, J. R. De La Torre, D. A. Stahl, Ammonia oxidation kinetics determine niche separation of nitrifying Archaea and Bacteria. *Nature*. **461**, 976–979 (2009).
91. G. Munz, C. Lubello, J. A. Oleszkiewicz, Factors affecting the growth rates of ammonium and nitrite oxidizing bacteria. *Chemosphere*. **83**, 720–725 (2011).
92. P. Servais, G. Billen, J. V. Rego, Rate of bacterial mortality in aquatic environments. *Appl. Environ. Microbiol.* **49**, 1448–1454 (1985).
93. G. Koch, K. Egli, J. R. Van Der Meer, H. Siegrist, Mathematical modeling of autotrophic denitrification in a nitrifying biofilm of a rotating biological contactor. *Water Sci. Technol.* **41**, 191–198 (2000).
94. M. R. Betlach, J. M. Tiedje, Kinetic Explanation for Accumulation of Nitrite, Nitric Oxide, and Nitrous Oxide during Bacterial Denitrification. *Appl. Environ. Microbiol.* **42**, 1074–1084 (1981).
95. D. Parsonage, A. J. Greenfield, S. J. Ferguson, The high affinity of Paracoccus denitrificans cells for nitrate as an electron acceptor. Analysis of possible mechanisms of nitrate and nitrite movement across the plasma membrane and the basis for inhibition by added nitrite of oxidase activity in permeabilised cells. *BBA - Bioenerg.* **807**, 81–95 (1985).
96. M. A. Altabet, R. Francois, D. W. Murray, W. L. Prell, Climate-related variations in denitrification in the Arabian Sea from sediment $^{15}N/^{14}N$ ratios. *Nature*. **373** (1995), pp. 506–509.
97. L. A. Bristow *et al.*, N_2 production rates limited by nitrite availability in the Bay of Bengal oxygen minimum zone. *Nat. Geosci.* **10**, 24–29 (2017).
98. T. Devries, The oceanic anthropogenic CO_2 sink: Storage, air-sea fluxes, and transports over the industrial era, *Global Biogeochemical Cycles*. **28**, 1–17 (2014).

99. A. R. Babbin, R. G. Keil, A. H. Devol, B. B. Ward, Organic matter stoichiometry, flux, and oxygen control nitrogen loss in the ocean. *Science (80-.).* **344**, 406–408 (2014).

100. T. DeVries, C. Deutsch, P. A. Rafter, F. Primeau, Marine denitrification rates determined from a global 3-D inverse model. *Biogeosciences*. **10**, 2481–2496 (2013).

101. D. Tsementzi *et al.*, SAR11 bacteria linked to ocean anoxia and nitrogen loss. *Nature*. **536**, 179–183 (2016).

102. B. Widner, C. W. Mordy, M. R. Mulholland, Cyanate distribution and uptake above and within the Eastern Tropical South Pacific oxygen deficient zone, *Limnol. Oceanogr.* **63**, 177–192 (2018).

103. L. Codispoti, Temperature, salinity, nutrients from Niskin bottles. *United States JGOFS Data Server*. Woods Hole Oceanographic Institution, USA: U.S. JGOFS Data Management Office (2000), (available at usjgofs.whoi.edu/jg/serv/jgofs/arabian/ttn-045/bottle.html0%7Bdir=usjgofs.whoi.edu/jg/dir/jgofs/arabian/ttn-045/,info=usjgofs.whoi.edu/jg/info/jgofs/arabian/ttn-045/ bottle%7D).

104. D. Bianchi, E. D. Galbraith, D. A. Carozza, K. A. S. Mislan, C. A. Stock, Intensification of open-ocean oxygen depletion by vertically migrating animals. *Nat. Geosci.* **6**, 545–548 (2013).

105. J. Huisman, F. J. Welssing, Biodiversity of plankton by species oscillations and chaos. *Nature*. **402**, 407–410 (1999).

106. J. Huisman, N. N. Pham Thi, D. M. Karl, B. Sommeijer, Reduced mixing generates oscillations and chaos in the oceanic deep chlorophyll maximum. *Nature*. **439**, 322–325 (2006).

107. A. Devol, "Physical, chemical, biological CTC and bottle data from R/V Thomas G. Thompson cruise TN278 in eastern tropical North Pacific Ocean from March 19 to April 20, 2012." DOC/NOAA/NESDIS/NCEI, National Oceanographic Data Center. (2013)

108. R. M. Holmes, et al, A simple and precise method for measuring ammonium in marine and freshwater ecosystems. *Can. J. Fish Aquat Scie*. **56**, 1801–1808

(1999).

109. P. B. Wignall, R. J. Twitchett, Oceanic anoxia and the end Permian mass extinction. *Science.* **272**, 1155–1158 (1996).

110. A. H. Knoll, R. K. Bambach, J. L. Payne, S. Pruss, W. W. Fischer, Paleophysiology and end-Permian mass extinction. *Earth Planet. Sci. Lett.* **256**, 295–313 (2007).

111. J. L. Payne, D. J. Lehrmann, D. Follett, M. Seibel, L. R. Kump, Erosional truncation of uppermost Permian shallow-marine carbonates and implications for Permian-Triassic boundary events, *GSA Bulletin*. **119**, 771–784 (2007).

112. J. L. Payne, A. V Turchyn, A. Paytan, D. J. Depaolo, D. J. Lehrmann, Calcium isotope constraints on the end-Permian mass extinction. *PNAS*. **107**, 8543–8548 (2010).

113. M. O. Clarkson *et al.*, Ocean acidification and the Permo-Triassic mass extinction. *Science.* **348**, 229–233 (2015).

114. M. R. Rampino, K. Caldeira, Major perturbation of ocean chemistry and a 'Strangelove Ocean' after the end-Permian mass extinction. *Terra Nova*. **17**, 554–559, (2005), doi:10.1111/j.1365-3121.2005.00648.x.

115. S. E. Grasby, B. Beauchamp, J. Knies, Early Triassic productivity crises delayed recovery from world's worst mass extinction, *Geology*. **44**, 779–782 (2016).

116. S. E. Grasby, H. Sanei, B. Beauchamp, Catastrophic dispersion of coal fly ash into oceans during the latest Permian extinction. *Nat. Geosci.* **4**, 104–107 (2011).

117. L. R. Kump, Massive release of hydrogen sulfide to the surface ocean and atmosphere during intervals of oceanic anoxia. *Geology.* **33**, 397–400 (2005), doi:10.1130/G21295.1.

118. K. Grice *et al.*, Photic Zone Euxinia During the Permian-Triassic Superanoxic Event. *Science*. **307**, 706–710 (2005).

119. C. Deutsch, A. Ferrel, B. Seibel, H. O. Pörtner, R. B. Huey, Climate change tightens a metabolic constraint on marine habitats. *Science.* **348**, 1132–1135 (2015).

120. J. T. Kiehl, C. A. Shields, Climate simulation of the latest Permian: Implications for mass extinction. *Geology*. **33**, 757–760 (2005).

121. C. Romano *et al.*, Climatic and biotic upheavals following the end-Permian mass extinction. *Nat. Geosci.* **6**, 57–60 (2012).

122. E. A. Sperling, J. C. Ingle Jr, A Permian-Triassic boundary section at Quinn River Crossing, northwestern Nevada, and implications for the cause of the Early Triassic chert gap on the western Pangean margin. *Geol. Soc. Am. Bull.*, **118** (2006).

123. J. L. Sarmiento, N. Gruber, M. A. Brzezinski, J. P. Dunne, High-latitude controls of thermocline nutrients and low latitude biological productivity. *Nature*. **427** (2004), doi:10.1038/nature02204.1.

124. H. O. Pörtner, Climate change affects marine fishes through the oxygen limitation of thermal tolerance. *Science.* **95** (2007), doi:10.1126/science.1135471.

125. C. C. Peterson, K. A. Nagy, J. Diamond, Sustained metabolic scope. *Proc. Natl. Acad. Sci.* **87**, 2324–2328 (1990).

126. S. M. Stanley, Estimates of the magnitudes of major marine mass extinctions in earth history. *PNAS E6325–E6334* (2016), doi:10.1073/pnas.1613094113.

127. H. Song *et al.*, Anoxia/high temperature double whammy during the Permian-Triassic marine crisis and its aftermath. *Sci. Rep.* **4**, 4132 (2014).

128. P. D. Roopnarine, K. D. Angielczyk, S. C. Wang, R. Hertog, Trophic network models explain instability of Early Triassic terrestrial communities, *Proc. R. Soc. B*. **274**, 2077–2086 (2007).

129. A. H. Knoll, R. K. Bambach, D. E. Canfield, J. P. Grotzinger, Comparative Earth History and Late Permian Mass Extinction. *Science.* **273**, 452-457 (1996).

130. R. J. Matear, A. C. Hirst, Long-term changes in dissolved oxygen concentrations in the ocean caused by protracted global warming. *Global Biogeochemical Cycles*. **17** (2003), doi:10.1029/2002GB001997.

131. N. G. Heavens, C. A. Shields, N. M. Mahowald, A paleogeographic approach to aerosol prescription in simulations of deep time climate. *Adv. Model. Earth Sys.* **4**, 1–13 (2012).

132. J. K. Moore, S. C. Doney, Upper ocean ecosystem dynamics and iron cycling in a global three-dimensional model. *Global Biogeochemical Cycles*. **18**, 1–21 (2004).

133. J. K. Moore, S. C. Doney, J. A. Kleypas, D. M. Glover, I. Y. Fung, An

intermediate complexity marine ecosystem model for the global domain. *Deep-Sea Research II.* **49**, 403–462 (2002).

134. K. Lindsay, The CESM Ocean Ecosystem Scientific Description. *Natl. Cent. Atmos. Res.* (2012), (available at https://www.cesm.ucar.edu/models/cesm1.0/pop2/doc/sci/ecosys_placeholder.html).

135. P. A. Sims, L. K. Medlin, D. G. Mann, Evolution of the diatoms : Insights from fossil , biological and molecular data. *Phycologia*. **45**, 361–402 (2006).

136. C. Winguth, A. M. E. Winguth, Simulating Permian-Triassic oceanic anoxia distribution: Implications for species extinction and recovery. *Geology*. **40**, 127–130 (2012).

137. T. Weber, C. Deutsch, Oceanic nitrogen reservoir regulated by plankton diversity and ocean circulation. *Nature*. **489**, 419–422 (2012).

138. N. M. Mahowald *et al.*, Atmospheric Iron Deposition: Global Distribution, Variability, and Human Perturbations. *Ann. Rev. Mar. Sci.* **1**, 245–278 (2009).

139. S. Severmann, J. Mcmanus, W. M. Berelson, D. E. Hammond, The continental shelf benthic iron flux and its isotope composition. *Geochim. Cosmochim. Acta*. **74**, 3984–4004 (2010).

140. R. Rosa *et al.*, Lower hypoxia thresholds of cuttlefish early life stages living in a warm acidified ocean. *Proc. R. Soc. B Biol. Sci.* **280**, 1–7 (2013).

141. T. J. Mickel, J. Childress, Effects of Temperature, Pressure, and Oxygen Concentration on the Oxygen Consumption Rate of the Hydrothermal Vent Crab Bythograea thermydron (Brachyura). *Physiol. Zool.* **55**, 199–207 (1982).

142. T. R . Fisher Oxygen uptake of the solitary tunicate *Styela plicata*. *Biological Bulletin*, **151**, 297-305 , (1976)

143. D. K. O. Chan, N. Y. S. Woo, The respiratory metabolism of the Japanese eel, Anguilla japonica: Effects of ambient oxygen, temperature, season, body weight, and hypophysectomy. *Gen. Comp. Endocrinol.* **35**, 160–168 (1978).

144. R. W. Brill, P. G. Bushnell, T. A. Elton, H. J. Small, The ability of blue crab (Callinectes sapidus, Rathbun 1886) to sustain aerobic metabolism during hypoxia. *J. Exp. Mar. Bio. Ecol.* **471**, 126–136 (2015).

145. R. Ern, J. L. Johansen, J. L. Rummer, A. J. Esbaugh, Effects of hypoxia and ocean acidification on the upper thermal niche boundaries of coral reef fishes. *Biol. Lett.* **13** (2017).
146. R. Ern, T. Norin, A. K. Gamperl, A. J. Esbaugh, Oxygen dependence of upper thermal limits in fishes. *Journal of Experimental Biology*. **219**, 3376–3383 (2016).
147. J. Childress, Effects of pressure, temperature, and oxygen on the oxygen consumption rate of the Midwater copepod Gaussia princeps. *Mar. Biol.* **39**, 19–24 (1976).
148. S. Artigaud, C. Lacroix, V. Pichereau, J. Flye-sainte-marie, Respiratory response to combined heat and hypoxia in the marine bivalves Pecten maximus and Mytilus spp . *Comp. Biochem. Physiol. Part A*. **175**, 135–140 (2014).
149. J. W. F. Chu, K. S. P. Gale, Ecophysiological limits to aerobic metabolism in hypoxia determine epibenthic distributions and energy sequestration in the northeast Pacific ocean. *Limnol. Oceanogr.* **62**, 59–74 (2017).
150. A. Dupont-prinet *et al.*, Northern shrimp (Pandalus borealis) oxygen consumption and metabolic enzyme activities are severely constrained by hypoxia in the Estuary and Gulf of St . Lawrence. *J. Exp. Mar. Bio. Ecol.* **448**, 298–307 (2013).
151. S. Lefevre, S. Watson, P. L. Munday, Will jumping snails prevail? Influence of near-future CO_2, temperature, and hypoxia on respiratory performance in the tropical conch Gibberulus gibberulus gibbosus. *Journal of Experimental Biology*. **218**, 2991–3001 (2015).
152. J. N. C. Whyte, B. L. Carswell, Determinants for Live Holding the Spot Prawn Pandalus Platyceros, Brandt. *Fisheries and Aquatic Sciences Canadian Technical Report No. 1129.* (1982).
153. B. J. Crear, G. N. R. Forteath, Flow-rate requirements for captive western rock lobsters (Panulirus cygnus): effects of boydy weight, temperature, activity, emersion, daily rhythm, feeding and oxygen tension on oxygen consumption. *Mar. Freshw. Res.* **52**, 763–771 (2001).
154. L. Ocampo, D. Patiño, C. Ramirez, Effect of temperature on hemolymph lactate and glucose concentrations in spiny lobster Panulirus interruptus during progressive hypoxia. *J. Exp. Mar. Bio. Ecol.* **296**, 71–77 (2003).

155. H. Zhou *et al.*, Sensitivity of Larvae and Adult and the Immunologic Characteristics of Litopenaeus vannamei under the Acute Hypoxia. *Journal of Chemistry.* (2014).

156. J. J. Torres, B. W. Belman, J. J. Childress, Oxygen consumption rates of midwater fishes as a function of depth of occureence. *Deep Sea Res. Part A, Oceanogr. Res. Pap.* **26**, 185–197 (1979).

157. L. A. Trueblood, B. A. Seibel, The jumbo squid, Dosidicus gigas (Ommastrephidae), living in oxygen minimum zones I : Oxygen consumption rates and critical oxygen partial pressures. *Deep. Res. Part II.* **95**, 218–224 (2013).

158. L. A. Dodds, J. M. Roberts, A. C. Taylor, F. Marubini, Metabolic tolerance of the cold-water coral Lophelia pertusa (Scleractinia) to temperature and dissolved oxygen change. *Journal of Experimental Marine Biology and Ecology*. **349**, 205–214 (2007).

159. J. F. Staples, J. J. Hershkowitz, Effects of ambient PO_2 and temperature on oxygen uptake in Nautilus pompilius, *J Comp Physiol B.* **170**, 231–236 (2000).

160. R. Mcallen, A. C. Taylor, J. Davenport, The effects of temperature and oxygen partial pressure on the rate of oxygen consumption of the high-shore rock pool copepod Tigriopus bre 6 icornis. *Comparative Biochemistry and Physiology Part A*. **123**, 195–202 (1999).

161. G. Le Moullac *et al.*, Metabolic adjustments in the oyster Crassostrea gigas according to oxygen level and temperature. *Mar. Biol. Res.* **3**, 357–366 (2007).

162. B. Y. P. J. Butler, E. W.- Taylor, The effect of progressive hypoxia on respiration in the dogfish (Scyliorhinus canicula) at different seasonal temperatures. *J. Exp. Biology*. **63**, 117–130 (1975).

163. R. F. Robertson, J. Meagor, E. W. Taylor, Specific Dynamic Action in the Shore Crab, Carcinus maenas (L.), in Relation to Acclimation Temperature and to the Onset of the Emersion Response. *Physiol. Biochem. Zool.* **75**, 350–359 (2002).

164. OBIS, Ocean Biogeographic Information System. *Intergov. Oceanogr. Comm. UNESCO* (2017), (available at www.iobis.org).

165. Paleobiology Database (2017). https://paleobiodb.org/#/

166. L. Quetin, J. CHildress, Respiratory Adaptations of Pleuroncodes planipes to its

environmnent off Baja California. *Mar. Biol.* **38** (1976), doi:doi:10.1007/BF00391372.

167. B. A. Seibel, B. E. Luu, S. N. Tessier, T. Towanda, K. B. Storey, Metabolic suppression in the pelagic crab, Pleuroncodes planipes, in oxygen minimum zones. *Comp. Biochem. Physiol. Part - B Biochem. Mol. Biol.* **224**, 88–97 (2018).
168. S. Díaz *et al.*, Pervasive human-driven decline of life on Earth points to the need for transformative change. *Science*. **1327** (2019), doi:10.1126/science.aaw3100.
169. S. Maxwell, R. A. Fuller, T. M. Brooks, J. E. M. Watson, The ravages of guns, nets and bulldozers. *Nature*. **536** (2016).
170. G. Ceballos *et al.*, Accelerated modern human – induced species losses: Entering the sixth mass extinction, *Science Adv.* 9–13 (2015).
171. D. J. McCauley *et al.*, Marine defaunation: Animal loss in the global ocean. *Science.* **347** (2015), doi:10.1126/science.1255641.
172. J. L. Payne, A. M. Bush, N. A. Heim, M. L. Knope, D. J. McCauley, Ecological selectivity of the emerrging mass extinction in the oceans. *Science.* **353**, 1284–1286 (2016).
173. B. C. O. Neill *et al.*, The Scenario Model Intercomparison Project (ScenarioMIP) for CMIP6, *Geosci. Model Dev.*, **9**, 3461–3482 (2018).
174. J. M. Sunday, A. E. Bates, N. K. Dulvy, Thermal tolerance and the global redistribution of animals. *Nat. Clim. Chang.* **2**, 686–690 (2012).
175. M. L. Pinsky, R. L. Selden, Z. J. Kitchel, Climate-Driven Shifts in Marine Species Ranges: Scaling from Organisms to Communities, *Ann. Rev. Mar. Sci.* **12**, 1–27 (2020).
176. J. J. Wiens, Climate-Related Local Extinctions Are Already Widespread among Plant and Animal Species, *PLoS Biol.* **14**, 1–18 (2016).
177. D. Tilman, R. M. Mayt, C. L. Lehman, M. A. Nowakt, Habitat destruction and the extinction debt. *Nature*. **371**, 65–66 (1994).
178. IUCN, The IUCN Red List of Threatened Species (2019). https://www.iucnredlist.org/
179. C. M. Duarte *et al.*, Will the Oceans Help Feed Humanity? *BioScience*, **59**, 967–976 (2009).

180. P. D, D. Zeller, Sea Around Us: Concepts, Design and Data (2015).

181. A. Dissanayake, A. Ishimatsu, Synergistic effects of elevated CO_2 and temperature on the metabolic scope and activity in a shallow-water coastal decapod (*Metapenaeus joyneri*; Crustacea: Penaeidae). *ICES J. Mar. Sci.* **68**, 1147–1154 (2011).

182. J. K. Moore *et al.*, Sustained climate warming drives declining marine biological productivity. *Science*. **1143**, 1139–1143 (2018).

183. A. P. D. Roopnarine, Extinction cascades and catastrophe in ancient food webs Extinction cascades and catastrophe in ancient food webs. *Paleobiology.* **32**, 1–19.

184. V. Eyring *et al.*, Overview of the Coupled Model Intercomparison Project Phase 6 (CMIP6) experimental design and organization, *Geosci. Model Dev.*, **9**, 1937–1958 (2016).

185. R. A. Locarnini, et al. World Ocean Atlas 2013, Volume 1: Temperature. S. Levitus, Ed., A. Mishonov Technical Ed.; NOAA Atlas NESDIS 73, 40 pp. (2013).

186. OBIS, "Ocean Biodiversity Information System" (2019). http://www.iobis.org/

187. Behrenfeld MJ, Falkowski PG. Photosynthetic rates derived from satellite based chlorophyll concentration. *Limnol Oceanogr* **42**, 1–20 (1997).

188. G. R. Mcghee Jr *et al.*, A new ecological-severity ranking of major Phanerozoic biodiversity crises. *Palaeogeogr. Palaeoclimatol. Palaeoecol.* **370**, 260–270 (2013).